TU Delft

Delft University of Technology

Kinematic Methods for the Rational Design of Mechanical Metamaterials

Broeren, F.G.J.

DOI
10.4233/uuid:5b00119f-793c-4a5c-8528-bace6934ad2e

Publication date
2022

Document Version
Final published version

Citation (APA)
Broeren, F. G. J. (2022). *Kinematic Methods for the Rational Design of Mechanical Metamaterials*. [Dissertation (TU Delft), Delft University of Technology]. https://doi.org/10.4233/uuid:5b00119f-793c-4a5c-8528-bace6934ad2e

Important note
To cite this publication, please use the final published version (if applicable).
Please check the document version above.

Copyright
Other than for strictly personal use, it is not permitted to download, forward or distribute the text or part of it, without the consent of the author(s) and/or copyright holder(s), unless the work is under an open content license such as Creative Commons.

Takedown policy
Please contact us and provide details if you believe this document breaches copyrights.
We will remove access to the work immediately and investigate your claim.

This work is downloaded from Delft University of Technology.
For technical reasons the number of authors shown on this cover page is limited to a maximum of 10.

Kinematic Methods for the Rational Design of Mechanical Metamaterials

Kinematic Methods for the Rational Design of Mechanical Metamaterials

Proefschrift

ter verkrijging van de graad van doctor
aan de Technische Universiteit Delft,
op gezag van de Rector Magnificus Prof. dr. ir. T.H.J.J. van der Hagen,
voorzitter van het College voor Promoties,
in het openbaar te verdedigen op
donderdag 8 december 2022 om 15:00 uur

door

Freek Gerardus Johannes BROEREN

Master of Science in Physics,
Leiden University, Leiden, Nederland
geboren te 's-Hertogenbosch, Nederland.

Dit proefschrift is goedgekeurd door de promotoren

Samenstelling promotiecommissie:

Rector Magnificus,	voorzitter
Prof. dr. ir. J.L. Herder,	Technische Universiteit Delft, promotor
Dr. ir. V. van der Wijk,	Technische Universiteit Delft, copromotor
Onafhankelijke leden:	
Prof. dr. A. Zadpoor,	Technische Universiteit Delft
Prof. dr. ir. K.M.B. Jansen,	Technische Universiteit Delft
Prof. dr. C. Borcea,	Rider University, USA
Prof. dr. ir. D.M. Brouwer	Universiteit Twente
Dr. ir. J.T.B. Overvelde	AMOLF / Technical Universiteit Eindhoven

This work was part of the Nanoscience Engineering Research Initiative (NERI) of TU Delft



Printed by: Gildeprint

Front & Back: Drawings and pictures created during the research on "Mechanical Metamaterials with $\nu = 1$ Based on the Inversor" (Chapter 5) are combined to illustrate the process of developing a monolythic mechanical metamaterial from linkages.

Copyright © 2022 by F.G.J. Broeren

ISBN 978-94-6384-398-0

An electronic version of this dissertation is available at http://repository.tudelft.nl/.

Wat is de werld toch groet, als ik mien oege sloet

Jack Poels

It is quite conceivable that the whole universe may constitute one great linkage, ... If the Cosmic linkage is of the kind I have called complete, then determinism is the law of Nature; but, if there be more than one of liberty in the system, there will be room for the play of free-will.

J.J. Sylvester

Contents

Summary 1

Samenvatting 3

1 Introduction 5
- 1.1 Objectives and Contributions of this Thesis. . . . 7
- 1.2 Structure of this Thesis 7
- Bibliografie 8

2 Definitions 11
- 2.1 Mechanical Metamaterial 11
- 2.2 Auxetic 12
- 2.3 Pseudo-Rigid Body Models 14
- 2.4 Periodicity 15
- Bibliografie 16

3 Spatial PRBM for a Tubular Mechanical Metamaterial 17
- 3.1 Introduction. . . . 18
- 3.2 The Elastomeric Tubular Strucutre 19
- 3.3 Two Pseudo-Rigid Body Models for the Post-Buckling Behavior. . . . 21
- 3.4 Pre-buckling estimation 24
- 3.5 Experimental Validaton 24
- 3.6 Discussion 26
- 3.7 Conclusion 27
- Bibliografie 28

4 Synthesis of Periodic Linkages with Constant ν 35
- 4.1 Introduction. . . . 36
- 4.2 Planar Periodic Linkages 36
- 4.3 Poisson's Ratio in Periodic Linkages 37
- 4.4 Discussion 42
- 4.5 Conclusion 43
- Bibliografie 43

5 Mechanical Metamaterials with ν=1 Based on the Inversor 45
- 5.1 Introduction. . . . 46
- 5.2 The inversor linkage 47
- 5.3 Periodic linkage design 48
- 5.4 Compliant Designs 51
- 5.5 Experimental Verification 52
- 5.6 Discussion 55

5.7 Conclusion . . . 57
Bibliografie . . . 58

6 Auxetic interval determination and experimental validation 61
6.1 Introduction . . . 62
6.2 The Periodic Framework . . . 63
6.3 Experimental Methods . . . 67
6.4 Results . . . 70
6.5 Discussion . . . 71
6.6 Conclusion . . . 73
Bibliografie . . . 73

7 Spherical Metamaterial Based on Symmetry Groups 77
7.1 Introduction . . . 78
7.2 Spherical Symmetry Groups . . . 79
7.3 Unit Cell Design . . . 80
7.4 Fabrication Methods . . . 81
7.5 Results . . . 81
7.6 Discussion . . . 83
7.7 Conclusions . . . 84
Bibliografie . . . 85

8 A General Method for the Creation of Dilational Surfaces 87
8.1 Introduction . . . 88
8.2 Results . . . 89
8.3 Discussion . . . 97
Bibliografie . . . 99

9 Discussion 103
Bibliografie . . . 106

10 Conclusion 109

Curriculum Vitæ 111

List of Publications 113

Acknowledgements 115

Summary

Most materials around us have properties that are determined at extremely small scales. Often the atoms and molecules that make up these materials determine how they behave under load. While this already leads to a great variety of material properties, a lot more is possible.

Mechanical metamaterials use structure to extend the available range of material properties. In this way, we can design material properties that are not found in nature. An example of this is materials with a negative Poisson's ratio. When these materials are compressed, they will not expand in the direction perpendicular to the applied deformation, as we would expect from natural materials. Rather, they will contract.

In general, mechanical metamaterials allow us to design materials with properties that are tailored to their intended solution. This provides more design freedom; instead of choosing from a list of available materials, the material properties themselves now become variables that can be designed. Additionally, this makes it possible to integrate multiple functions within a material. In this way, the material is no longer passive but can react based on applied forces, deformations, or changes in the environment.

In practice, designing mechanical metamaterials has turned out to be difficult. While there are many examples of mechanical metamaterials with exceptional properties, their discovery has rarely been based on a rational and structured design process. The lack of such a design strategy makes the design of metamaterials with exactly the desired properties, at least for now, difficult and unreliable.

This dissertation explores this design problem and presents a method to aid in the structured and rational design of mechanical metamaterials. This method is based on a pseudo-rigid body approach, borrowed from the field of compliant mechanisms. Following this approach, the metamaterial is modeled as a collection of rigid parts, which are connected by joints to which we assign a stiffness. This allows us to model both the deformation and the stiffness of the material while keeping the complexity of the models as low as possible.

Because of the limited complexity of the models, this approach allows the designer to understand the effects of design decisions and adaptations. This enables directed and conscious changes to the design, of which the consequences are known beforehand. This is different from alternative methods where highly complex and time-consuming computer models are used to calculate the effects of changes. By using less complex models and making directed choices, new design iterations can be generated more quickly. Especially at the start of a design process, this is expected to quickly lead to new insights. These can then at a later stadium be refined using more detailed methods.

Outline of this Dissertation

After the introduction in Chapter 1, Chapter 2 presents the most important definitions for this dissertation. In Chapter 3, a cylindrical mechanical metamaterial is analyzed using a pseudo-rigid body model. We see that a relatively simple model with only one degree of freedom is sufficient for describing the force-deflection behavior, but that more degrees of freedom are necessary in order to include the experimental boundary conditions.

Chapters 4 and 5 investigate the synthesis problem in the plane: how can a periodic structure be designed to have exactly the desired constant Poisson's ratio? As a basis for this design, we use well-known linkages. In this way, we use the vast field of research into curve-generating mechanisms. By choosing the right mechanism and adapting it to a periodic lattice, the desired constant Poisson's ratio can be achieved.

Chapter 6 Further investigates the relation between linkages and Poisson's ratio, this time in three dimensions. Using microscale experiments, it is shown that models that only regard rigid links connected by ball joints give a good indication of the range of motion for which auxetic behavior can be observed.

Chapters 7 and 8 finally investigate the synthesis of mechanical metamaterials on curved surfaces. In chapter 3, we have seen that mechanisms on such surfaces often behave differently than we are used to in the plane. That poses extra challenges to the design of metamaterials that follow these curved surfaces. Here, we approach this problem by subdividing the surfaces into multiple flat facets. By doing this, planar mechanisms can be used as the basis of the curved structures. These two chapters show two distinct methods in which curved surfaces are enabled to dilate; they can change their size without changing their shape.

Samenvatting

De meeste materialen om ons heen hebben eigenschappen die bepaald worden op een heel klein niveau. Vaak zijn het de atomen en moleculen waarvan ze gemaakt zijn die bepalen hoe ze zich gedragen wanneer ze aan krachten blootgesteld worden. Dit zorgt al voor een enorme verscheidenheid aan materiaaleigenschappen, maar er is nog veel meer mogelijk.

Mechanische metamaterialen gebruiken structuur om het beschikbare palet aan materiaaleigenschappen uit te breiden. Zo kunnen we materiaaleigenschappen ontwerpen die niet in de natuur te vinden zijn. Een voorbeeld hiervan zijn materialen met een negative dwarscontractiecoefficient. Wanneer deze materialen ingedrukt worden zullen ze in de richting loodrecht op de toegepaste indrukking niet uitzetten, zoals we van natuurlijke materialen verwachten, maar juist samentrekken.

Meer algemeen geven mechanische metamaterialen ons de mogelijkheid om materialen te ontwerpen met eigenschappen die aansluiten op de beoogde toepassing. Zo ontstaat er meer ontwerpvrijheid; in plaats van het kiezen uit een lijst met materialen kan je nu het materiaal met precies de juiste eigenschappen ontwerpen. Daarnaast geeft het ook mogelijkheden voor het integreren van verschillende functies in een materiaal. Het materiaal is niet langer een passief onderdeel, maar kan zelf ook functies uitvoeren in reactie op opgelegde krachten, vervormingen of omgevingsveranderingen.

In de praktijk blijkt het ontwerpen van deze materialen ingewikkeld te zijn. Er zijn al verschillende voorbeelden van metamaterialen met bijzondere eigenschappen, maar vaak zijn deze ontdekt zonder dat daar een bewust en gestructureerd ontwerpproces aan ten grondslag lag. Het ontbreken van een dergelijke ontwerpstrategie maakt het ontwerpen van materialen met precies de gewenste eigenschappen op dit moment nog lastig en onbetrouwbaar.

Deze dissertatie bekijkt dit ontwerpvraagstuk en biedt een methode aan om het gestructureerd en bewust ontwerp van mechanische metamaterialen te vergemakkelijken. Deze is gebaseerd op een pseudo-starre lichamen aanpak, geleend uit het veld van de buigende mechanismen. Volgens deze aanpak kunnen wij het metamateriaal modelleren als een verzameling starre onderdelen, verbonden met scharnieren die een stijfheid meekrijgen. Hierdoor kan zowel de beweging als de effectieve stijfheid van het materiaal gemodeleerd worden terwijl de modellen zo eenvoudig mogelijk blijven.

Doordat de modellen relatief eenvoudig blijven geeft deze aanpak de ontwerper de mogelijkheid om het effect van aanpassingen te overzien. Dit maakt het mogelijk om gericht aanpassingen aan het ontwerp te doen waarvan je van tevoren al een goede inschatting kan maken wat daar het effect van gaat zijn.

Dit in tegenstelling tot andere methoden waarbij vaak ingewikkelde computermodellen nodig zijn om te berekenen wat het effect van een verandering is. Hierdoor kunnen nieuwe ontwerpiteraties sneller gegenereerd worden. De verwachting is dat dit zeker in het begin van het ontwerpproces snel tot nieuwe inzichten kan leiden. Deze kunnen dan in een later stadium met langzamere en meer gedetailleerde methoden verfijnd worden.

Opzet van dit Proefschrift

Na de introductie in Hoofdstuk 1 worden in Hoofdstuk 2 de belangrijkste definities voor dit proefschrift gegeven. In hoofdstuk 3 wordt een cylindrisch mechanisch metamateriaal geanalyseerd aan de hand van een pseudo-starre lichamen model. Hierin zien we dat een eenvoudig model met één graad van vrijheid al voldoende is voor het beschrijven van het kracht-weg gedrag, maar dat meerdere graden van vrijheid nodig zijn om de experimentele randvoorwaarden mee te nemen.

Hoofdstukken 4 en 5 bekijken het synthese probleem in het platte vlak: hoe kan je een periodieke structuur maken met precies de gewenste, constante, dwarscontractiecoefficient? Als basis hiervoor worden bekende stangenmechanismen gebruikt. Zo maken we gebruik van de het enorme onderzoeksveld naar mechanismen die gebruikt worden om krommen te tekenen. Door het juiste mechanisme te kiezen en dit aan te passen naar een herhalend rooster kan de gewenste, constante, dwarscontractiecoefficient bereikt worden.

Hoofdstuk 6 gaat verder in op de relatie tussen stangenmechanismen en dwarscontractiecoefficient, dit keer in drie dimensies. Door middel van experimenten op microschaal wordt aangetoond dat modellen die uitgaan van oneindig stijve stangen die roteren in perfecte bolscharnieren een goede voorspelling geven van het vervormingsbereik waarvoor auxetisch gedrag optreedt.

Hoofdstukken 7 en 8 bekijken tenslotte de synthese van metamaterialen in gekromde vlakken. In het hoofdstuk 3 zagen we ook al dat mechanismen op deze oppervlakken vaak niet werken zoals we gewend zijn. Dat kan het ontwerpen van metamaterialen die deze vlakken volgen lastig maken. Dit probleem wordt hier aangepakt door het beoogde oppervlak op te delen in verschillende, vlakke, facetten. Hierdoor kunnen vlakke mechanismen gebruikt worden als de basis voor gekromde structuren. De twee hoofdstukken laten twee manieren zien waarop we gekromde oppervlakken de mogelijkheid geven om van groottte te veranderen zonder dat hun vorm verandert.

1

Introduction

Why is it that we can compress a block of rubber by hand, but have a substantially harder time compressing a block of steel? How come a piece of glass shatters when impacted, but a rubber ball deforms and returns to its original state? When we consider these material properties, we naturally assume that they originate in the chemical properties of the materials. For most materials we find in nature, their chemical composition is indeed the most prominent factor determining their material properties. Rubber is relatively soft and can regain its shape from large deformations because it consists of long polymers that can slide past each other, while the bonds between the atoms in steel are stronger, which causes objects made from steel to have a higher stiffness.

However, these atomic and molecular bonds can not explain the complete variety of properties we see in natural materials. The bones of birds, for example, are substantially lighter by volume than those of an elephant [1], even though they are made of the same material. The difference here is structure, by changing the structure of a material at length scales substantially longer than those of atoms and molecules, the properties of bulk materials can be significantly altered. This concept, of structure altering the properties of materials, is what lies at the basis of metamaterials.

Metamaterials have first been introduced with respect to optical properties, but quickly spread to other fields, such as acoustics and mechanics [2]. This dissertation deals with the latter type of metamaterials. In mechanical metamaterials, the mechanical properties, such as stiffness or deformations resulting from an external force are significantly altered by structure. This has resulted in metamaterials with a density so low that a centimeter-sized block can be supported by the seedhead of a dandelion [3], but also metamaterials that shrink in all directions when compressed [4] or multistable structures that can be stable in a large number of states [5].

Among the most illustrative examples are those metamaterials that have been designed to have a negative Poisson's ratio [4]. When we stretch a rub-

ber band, it will become thinner in the lateral direction. This is what we see in almost all natural materials and therefore also what we intuitively feel should happen. When structure is added to such materials, however, this behavior can be changed. A natural example of this is cork, which does not change its width at all when stretched along certain directions [6]. In artificial metamaterials, this behavior can be taken even further to materials that expand in the directions perpendicular to an applied stretch. These metamaterials are characterized by a negative Poisson's ratio and are often called auxetics, after the Greek "αύξησις": that which may be increased [7].

The material properties that can be designed in mechanical metamaterials are not limited to Poisson's ratio. Mechanical metamaterials possess the promise of being able to tailor mechanical properties to the requirements of any given application. Already in 1995, Milton and Cherkaev proved that any elasticity tensor can be synthesized in a structured composite of two materials [8], or as they put it:

> "Thus, if in the beginning, God gave man just two materials, one sufficiently soft and the other sufficiently rigid (plus some glue and some cutting tools) then man could make everything!"

However, while many examples of structures with exotic properties have been presented since their paper appeared, the design methods for these structures remain elusive, as was pointed out by Bertoldi et al. in 2017:

> "...the rational design of metamaterials with a target property or functionality remains fiendishly difficult, and many designs so far have relied on luck and intuition." [9]

The work in this dissertation is aimed towards making this promise reality: the design of mechanical metamaterials to have exactly the properties that we desire. For this, a kinematic approach to the problem has been chosen.

Many mechanical metamaterials rely on the bending of internal slender parts for their function [10, 11]. By modeling the slender elements as revolute joints with a representative stiffness and the rest of the structure as rigid bodies, accurate descriptions of the metamaterial behavior can be obtained [12]. This approach is commonly used in the analysis of compliant mechanisms, where it is known as *Pseudo-Rigid Body modeling* [13].

To design new mechanical metamaterials, we reverse this process. Instead of analyzing the metamaterial using a rigid body analog, we design a mechanism with the desired properties and later convert it into a monolithic mechanical metamaterial. The advantage of this approach is that we are able to use our pre-existing knowledge of kinematics to design new materials. Furthermore, the kinematic theories behind the designs are inherently non-linear and are therefore suitable for large deformations. Finally, because the kinematic formulations used in this design process are analytic, faster design iterations are possible than with computational methods such as the commonly used Finite Element Method.

1.1. Objectives and Contributions of this Thesis

This thesis aims to further the understanding of mechanical metamaterial design by developing rational synthesis methods based on Pseudo-Rigid Body Models (PRBMs). These models are well-known as design and modeling methods for compliant mechanisms [13]. Since these mechanisms rely on the bending of slender parts of their structure for their function, just as bending-dominated mechanical metamaterials do, it is assumed that these models will be useful.

Compared to compliant mechanisms, Pseudo-Rigid Body Models for mechanical metamaterials do come with additional challenges. In general, metamaterial designs will be periodic. That means that they consist of identical unit cells which fill the space. In designing the kinematics of these structures, one has to take the connections between the individual unit cells into account to ensure that the neighboring unit cells fit together. Additionally, analyzing just the single unit cell can prove insufficient because the coupling between unit cells can increase or decrease the total number of degrees of freedom of the material as a whole.

Using PRBMs for the design of mechanical metamaterials allows us to design periodic structures using the available toolboxes for mechanism design. In this way, the mechanical properties of a metamaterial are designed as a kinematic transmission with appropriate joint stiffness.

Additionally, this kinematic design method is used to add functionality to curved surfaces. For this, the regular method of creating periodic structures is no longer applicable since the Bravais lattices that underlie this periodicity can not generally be transmitted to curved surfaces. For this, alternative methods are developed and applied.

1.2. Structure of this Thesis

This thesis demonstrates how pseudo-rigid body models can be used for the modeling and design of mechanical metamaterials.

In Chapter 3, a cylindrical mechanical metamaterial is modeled as a mechanism consisting of rigid plates connected by hinges with stiffness. This way, the behavior of the metamaterial is closely approximated, with only a fraction of the computational expense associated with conventional finite element methods.

In Chapter 4, we investigate how to design a given value of Poisson's ratio in periodic linkages. For this, we define Poisson's ratio as a geometrical transmission between two orthogonal directions and find linkages that match the prescribed transmission ratio. For this, we take inspiration from the large body of mechanism and linkage research that exists.

In Chapter 5, one of these linkages is further developed into a compliant mechanical metamaterial. We explore different ways to create a compliant unit cell out of an inversor linkage and compare three possible designs using experimental tests.

Chapter 6 investigates the concept of the auxetic interval. Not every auxe-

tic structure remains auxetic for large deformations. Most will have regions in their deformation path where they exhibit auxetic behavior, but outside of which they demonstrate a positive Poisson's ratio for certain directions. Here, we take an existing design of an auxetic framework, manufacture it on the microscale, and compare their theoretical and experimentally determined auxetic intervals

Chapters 7 and 8 investigate mechanical metamaterials on curved surfaces. On curved surfaces, periodicity as we know it no longer applies since it becomes impossible to copy and translate a unit cell over them without deforming it. In Chapter 7, we investigate the case of a spherical surface and create an origami-inspired structure based on the symmetries of the sphere. In Chapter 8, we expand this even further and investigate arbitrarily curved surfaces. We propose a design based on the pantograph that allows for dilation of the surface and proves that this design method can be applied to surfaces with any curvature.

Finally, Chapter 9 discusses the overall design methodology presented in this thesis. We assess the usefulness of PRB modeling for mechanical metamaterials as well as its limitations and look forward to future challenges and possible applications.

Bibliografie

[1] T. N. Sullivan, B. Wang, H. D. Espinosa, and M. A. Meyers, *Extreme lightweight structures: avian feathers and bones,* Materials Today **20**, 377 (2017).

[2] M. Kadic, T. Bückmann, R. Schittny, and M. Wegener, *Metamaterials beyond electromagnetism,* Reports on Progress in Physics **76**, 126501 (2013).

[3] T. A. Schaedler, A. J. Jacobsen, A. Torrents, A. E. Sorensen, J. Lian, J. R. Greer, L. Valdevit, W. B. Carter, Q. Ge, J. A. Jackson, S. O. Kucheyev, N. X. Fang, and C. M. Spadaccini, *Ultralight metallic microlattices.* Science **334**, 962 (2011).

[4] H. A. Kolken and A. A. Zadpoor, *Auxetic mechanical metamaterials,* RSC Adv. **7**, 5111 (2017).

[5] B. Haghpanah, L. Salari-Sharif, P. Pourrajab, J. Hopkins, and L. Valdevit, *Architected Materials: Multistable Shape-Reconfigurable Architected Materials (Adv. Mater. 36/2016),* Advanced Materials **28**, 8065 (2016).

[6] L. J. Gibson and M. F. Ashby, *Cellular Solids: Structure and Properties*, 2nd ed., Cambridge Solid State Science Series (Cambridge University Press, 1997).

[7] K. E. Evans, *Auxetic polymers: a new range of materials,* Endeavour **15**, 170 (1991).

[8] G. W. Milton and A. V. Cherkaev, *Which Elasticity Tensors are Realizable?* J. Eng. Mater. Technol. **117**, 483 (1995).

[9] K. Bertoldi, V. Vitelli, J. Christensen, and M. Van Hecke, *Flexible mechanical metamaterials,* Nat. Rev. Mater. **2** (2017), 10.1038/natrevmats.2017.66.

[10] V. Deshpande, M. Ashby, and N. Fleck, *Foam topology: bending versus stretching dominated architectures,* Acta Mater. **49**, 1035 (2001).

[11] H. Mitschke, F. Schury, K. Mecke, F. Wein, M. Stingl, and G. E. Schröder-Turk, *Geometry: The leading parameter for the Poisson's ratio of bending-dominated cellular solids,* Int. J. Solids Struct. **100**, 1 (2016).

[12] J. N. Grima, P. S. Farrugia, C. Caruana, R. Gatt, and D. Attard, *Auxetic behaviour from stretching connected squares,* J. Mater. Sci. **43**, 5962 (2008).

[13] L. L. Howell, S. P. Magleby, and B. M. B. M. Olsen, *Handbook of compliant mechanisms* (John Wiley & Sons Ltd, 2013).

2

Definitions

Mechanical Metamaterials is a relatively young and very active field of research. In the past years, many terms have been used to describe these structures, among which *Mechanical Metamaterials* and *Architected Materials* are the most prominent. Similarly, the terms to describe the behavior of these structures also differ between works and terms used in literature can have different meanings depending on the author or context.

In order to explain the concepts of metamaterial research accurately, a common set of definitions needs to be established. Therefore, we will use this section to give explanations and definitions for the most important terms and concepts in this thesis. These definitions have come both from literature and my own experiences and should in no way be assumed to be valid for all literature on this topic. They do, however, apply to the entirety of this thesis.

2.1. Mechanical Metamaterial

The term *metamaterial* was originally used to refer to periodic structures with unusual bulk optical properties [1]. In optics, and similarly in acoustics, there seems to be a general consensus that a metamaterial should have the following properties:

- Structure-dominated optical or acoustical properties, different from the properties of the constituent materials
- Periodic structure with a period shorter than the wavelength of the light or sound for which it was designed

For mechanical metamaterials, however, the relevant material properties are usually bulk properties and therefore have an infinite wavelength. Therefore, there is no inherent length scale to these structures and the second property described above becomes irrelevant. There are also many examples of

mechanical metamaterials with an aperiodic structure that still have properties different from their constituent materials. The foams with a negative Poisson's ratio created by Roderic Lakes in 1987 [2] are a good example of this. Therefore, since there is no defined length scale and periodicity is not required, one might wonder whether even a chair could be classified as a mechanical metamaterial since its mechanical properties are different from the wood from which it was made.

In order to get to a more useful definition, let us focus on the material part of the metamaterial. Merriam-Webster dictionary defines a material as:

> "The elements, constituents, or substances of which something is composed or can be made". [3]

Based on this definition of a material, we can define mechanical metamaterials similarly:

> A structure with mechanical properties that are different from those of its constituent materials due to an internal structure, from which something is composed or can be made.

From this definition, we can see that a mechanical metamaterial should be divisible; if we have a block of it, we should be able to split it without changing its bulk properties. This rules out the example of the chair discussed above, since a chair split in half will have different properties and functionality from the complete chair.

With this definition comes a new length scale. Since mechanical metamaterials are often periodic or are foams with an average cell size as a characteristic length scale, it becomes evident that one can not create arbitrarily thin slices of these materials without changing their bulk properties. When the slices become thinner than the characteristic length of the material, the structure will no longer behave as the designed collective structure. This new length scale is therefore application driven; it is determined by the smallest feature size that one would want to make out of the metamaterial. As long as this smallest feature size is sufficiently larger than the characteristic length scale of the metamaterial structure, the designed bulk properties should hold and we can speak of a mechanical metamaterial.

2.2. Auxetic

One of the most studied properties in mechanical metamaterials research is *Poisson's ratio*. This quantity describes the ratio between a resulting transverse strain induced by an applied longitudinal strain. For almost all natural materials, this ratio is positive; this means that when we stretch these materials along one direction, they contract in perpendicular directions. This is the behavior we expect from material and can be observed when we, for example, stretch a rubber band.

By creating clever internal structures, it is possible to create mechanical metamaterials with negative Poisson's ratios. These structures will expand in perpendicular directions when stretched. One of the first examples of this behavior is pre-compressed foams [2], but later many more examples have been created [4–6].

To give a complete characterization of the strains in a material resulting from a uniaxial compression, at least two Poisson's ratios need to be defined. Typically, these are ν_{xy} and ν_{xz}, where the x, y and z directions are perpendicular. These two Poisson's ratios can (and often will be) different.

Materials with negative Poisson's ratios are rarely found in nature, which is why this property is perceived as counterintuitive. The Holey Sheet, a prototypical mechanical metamaterial consisting of a rubber sheet perforated with a square array of round holes [4], possesses this property. When this structure is compressed uniaxially in the plane, it will also contract in the perpendicular in-plane direction. In the direction out of plane, however, the strains are small but positive, since they are dominated by the material from which the metamaterial is constructed. Therefore, when we would calculate Poisson's ratio for this structure using an in-plane axis and the out of plane axis, we will find a small but positive Poisson's ratio.

To give a complete characterization of the strains in a material resulting from a uniaxial compression, at least two Poisson's ratios need to be defined: ν_{xy} and ν_{xz}, where the x, y and z directions are perpendicular. These two Poisson's ratios can (and often will be) different, as we have seen in the example of the Holey Sheet.

In his paper from 1991 [7], Ken E. Evans introduced the term *Auxetic* for material with a negative Poisson's ratio. This term comes from the Greek word *auxetos*, which means "that may be increased". With this term, he refers to the fact that materials with a negative Poisson's ratio increase their size in all directions, and therefore increase their volume, when stretched.

Following the paper by Evans, many mechanical metamaterials with negative Poisson's ratios have been grouped under the term auxetic. However, when we consider three-dimensional structures, multiple Poisson's ratios need to be taken into account, and it can be possible for a structure to have a negative Poisson's ratio for one set of axes, but a positive one for another. Therefore, when stretched only two dimensions of the structure would increase, when one decreases. This behavior is not consistent with auxeticity as described above.

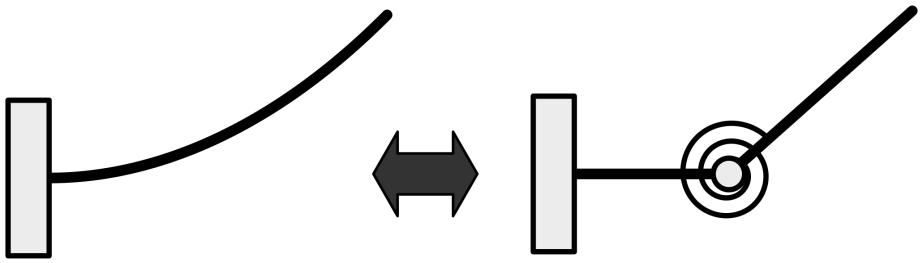
A more exact definition for periodic frameworks is given by Ciprian S. Borcea and Ileana Streinu [5]. For their definition, they use the generators of the periodic lattice. These generators are the vectors along which we translate the unit cell to build up the periodic structure. According to their definition, auxetic motion for a periodic framework is a kinematically allowed periodic motion for which these generators either all simultaneously increase in length or stay the same, or they all simultaneously decrease in length or stay the same. Therefore, if we have a general periodic framework with a parallelepiped unit cell, and this framework has an allowable periodic motion for which none of its bars

changes in length, it is only auxetic when all sides of the parallelepiped (these constitute the generators) increase in length or stay the same, or when they all decrease in length or stay the same.

Following this definition of auxeticity, we see that the direction of the deformations of the metamaterial should be equal or zero for all global dimensions of the structure. None of its global dimensions can decrease when another increases or vice-versa. Therefore, the Holey Sheet we discussed before, when considered in three dimensions, is only auxetic when there is no global change in the thickness of the sheet when it is deformed in-plane.

2.3. Pseudo-Rigid Body Models

The basis for much of the work in this thesis is Pseudo-Rigid Body Modeling (PRBM). This technique originates in compliant mechanism design and is described in detail in the books by Larry L. Howell [8, 9].



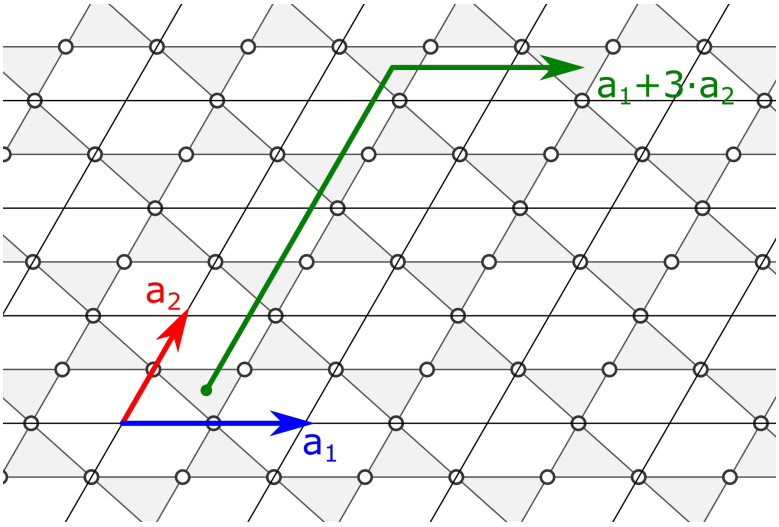
Figuur 2.1: Pseudo-Rigid Body Models approximate the behavior of a bending beam by modeling it as rigid bars connected by revolute joints with a corresponding torsional stiffness.

At the basis of this modeling technique lies the idea that, up to remarkably large deformations, the movement of a bending beam can be approximated by a system of rigid bars and joints, and that the corresponding stiffness can be modeled as a linear torsional stiffness in these joints. By investigating the bar-and-joint system, instead of the continuous beam, a good approximation of the behavior can be obtained with a significantly simpler model. For more complex compliant structures, such as the metamaterials in this thesis, it allows us to study their kinematics without having to consider the compliance of the structure at every point. In this way, it becomes easier and more intuitive to visualize the allowed motions and yet obtain an accurate description.

Similarly, this PRBM can also be used as a design methodology by reversing the above process. It can be used to convert a linkage into a compliant mechanism by designing slender parts into a continuous structure that corresponds to the joints in the linkage. The stiffness of the resulting compliant mechanisms can then be designed by choosing the dimensions, and therefore stiffness, of these slender elements.

2.4. Periodicity

In order for linkages or compliant mechanisms to be applied as mechanical metamaterials, their properties need to be distributed over large areas. A common method to achieve this is through periodicity. Periodic structures consist of many identical basic elements, called unit cells. A unit cell typically has a parallelogram or parallelepiped shape, for the 2D and 3D cases respectively, such that the complete space can be filled by stacking these unit cells, see Fig. 2.2. The resulting periodic lattice is also called a Bravais lattice, after Auguste Bravais, and is often used in crystallography to describe the arrangements of atoms and molecules in a crystalline material.



Figuur 2.2: A periodic lattice consists of unit cells that are copied and translated along the lattice generators to fill space. Here, the unit cells are indicated by a black grid. The generators of the lattice are labeled a_1 and a_2. In green, it is illustrated that any integer sum of generators will bring you to a similar point of the lattice.

In order to fill space, the unit cells are translated along a set of two or three independent vectors for the planar and spatial case, respectively. These vectors are called the generators of the periodicity lattice. Starting from a point on the periodic structure, a translation by any integer sum of generators will always result in an equivalent point on the lattice.

When designing a unit cell, care must be taken to ensure that the mechanism in the unit cell correctly matches with the neighboring unit cells. For this, periodic boundary conditions are often used. These boundary conditions simulate the existence of all neighboring unit cells. For the planar case, this effectively transforms the unit cell into the surface of the torus. This connects each set of opposite edges of the unit cell. When using these boundary conditions only a single unit cell needs to be analyzed. If motion can exist within this unit cell, it is ensured that a periodic degree of freedom exists in the complete infinitely

large periodic lattice.

A unit cell with one degree of freedom does not, however, ensure that only one degree of freedom exists in the lattice. The Kagome lattice, for example, can be constructed out of rhombic unit cells, each containing two triangular bodies, as has been done in Fig. 2.2. These two bodies are coupled by a single revolute joint and the unit cell will therefore have one degree of freedom. However, when a larger patch of the periodic lattice is investigated, we see that it has more degrees of freedom. These other degrees of freedom could not be observed from the single unit cell since they break the symmetry of the original lattice. Only when we expand the unit cell beyond the original rhombus (this is also known as relaxing the periodicity), do we find these degrees of freedom [10].

Bibliografie

[1] N. Engheta and R. W. Ziolkowski, *Metamaterials. Physics and Engineering Explorations* (Wiley-IEEE Press, 2006).

[2] R. Lakes, *Foam Structures with a Negative Poisson's Ratio,* Science (80-.). **235**, 1038 (1987).

[3] *Material,* (2020).

[4] K. Bertoldi, P. M. Reis, S. Willshaw, and T. Mullin, *Negative Poisson's Ratio Behavior Induced by an Elastic Instability,* Adv. Mater. **22**, 361 (2010).

[5] C. Borcea and I. Streinu, *Geometric auxetics,* Proc. R. Soc. A Math. Phys. Eng. Sci. **471**, 20150033 (2015).

[6] A. Rafsanjani and D. Pasini, *Bistable auxetic mechanical metamaterials inspired by ancient geometric motifs,* Extrem. Mech. Lett. (2016), 10.1016/j.eml.2016.09.001.

[7] K. E. Evans, *Auxetic polymers: a new range of materials,* Endeavour **15**, 170 (1991).

[8] L. L. Howell, *Compliant mechanisms* (Wiley, 2001) p. 459.

[9] L. L. Howell, S. P. Magleby, and B. M. B. M. Olsen, *Handbook of compliant mechanisms* (John Wiley & Sons Ltd, 2013).

[10] R. Hutchinson and N. Fleck, *The structural performance of the periodic truss,* J. Mech. Phys. Solids **54**, 756 (2006).

3

Spatial Pseudo-Rigid Body Model for the Analysis of a Tubular Mechanical Metamaterial

Freek G.J. Broeren, Volkert van der Wijk, Just L. Herder

This paper proposes a Pseudo-Rigid Body Model for the analysis of a spatial mechanical metamaterial and demonstrates its application. Using this model, the post-buckling behavior of the mechanical metamaterial can be determined without the need to consider the whole elastic structure, e.g. using finite element procedures. We do this by analyzing a porous cylindrical mechanical metamaterial using a rigid body mechanism, consisting of rigid squares that are connected at their corners. Stiffness in this model comes from torsion springs placed at the connections between the rigid parts. The theory of the model is presented and we compare the results of two versions of this model with experiments. One version describes the metamaterial in the free state, while the other, more extended, version includes clamped boundaries, matching the conditions of the experimental set-up. We show that the mechanical behavior of the spatial metamaterial is captured by the models and that the shape of the metamaterial in the deformed state can be obtained from the more extended model.

The contents of this chapter have been published in Mathematics and Mechanics of Solids (2019) [1].

3.1. Introduction

Mechanical metamaterials are artificially designed materials of which the mechanical properties are dominated by their structure, rather than by the chemical composition of the constituent materials. In this way, materials can be designed with novel properties, such as a negative Poisson's ratio, vanishing elastic moduli and extreme stiffness to weight ratios [2, 3].

These material structures have potential applications in a variety of fields. Mechanical metamaterials with negative Poisson's ratios are applied in a diverse range of industries [4]. In medicine, such structures have been proposed as stents [5, 6] and in sporting equipment, structures with negative Poisson's ratios have been used in the soles of running shoes for their shock absorbing properties [7] or in textiles for better shape-fitting to the wearer [8].

Material structures with vanishing elastic moduli could find applications in impact protection and seismic isolation [9]. Materials with extreme stiffness to weight ratios could be used in automotive or aerospace applications to reduce weight without reducing the strength of the parts fabricated from these structured materials [10, 11].

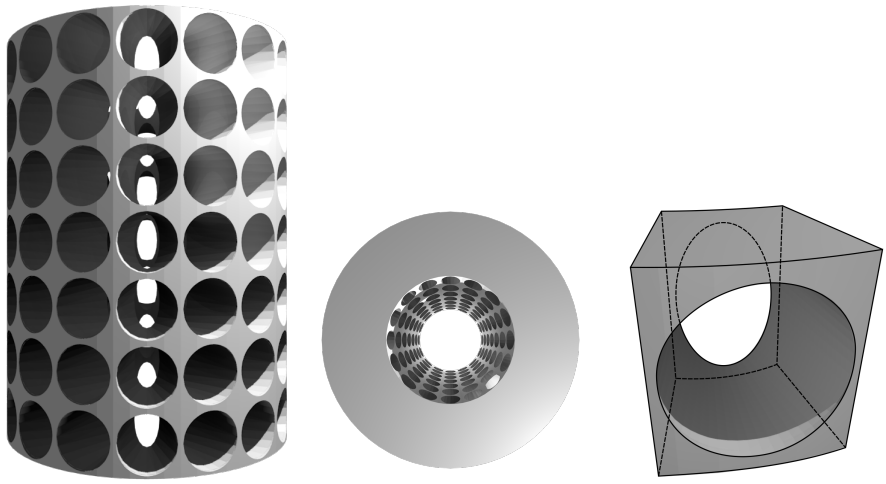
Mechanical metamaterials can be split up in two classes: bending-, and stretching dominated structures [12, 13], named after the most dominant deformation of the slender parts of their structures. Stretching dominated structures are generally designed to be stiff and light [14]. Bending dominated structures on the other hand have been designed to have a broader range of properties like a negative Poisson's ratio [15–17] and multiple stable states [18–21]. This paper is focused on the modeling of bending dominated structures.

Because of the elastic deformations of the structure, bending dominated mechanical metamaterials require extensive computational effort for analysis, since the complete elastomeric structure needs to be considered at once. Generally, this is done by finite element methods [21–23].

As an alternative to the computationally intensive finite element methods, pseudo-rigid body models (PRBM) [24] can be used for the analysis of these structures. With this method, the elastomeric structure is approximated by a rigid body mechanism with torsion springs at the hinges to model the elastic forces. Using this method, the calculations for analysis become significantly simpler and analytical solutions of the material properties can be obtained. Similar methods have been used by Florijn et al. [18] to model a planar bistable mechanical metamaterial and by Turco et al. [25] to model planar pantographic lattices.

Current examples of rigid body mechanisms used to model mechanical metamaterials are either solely kinematic [26–28] or only consider planar structures [18, 29–31]. However, for spatial mechanical metamaterials pseudo-rigid body models have not been applied yet, while for these more complicated structures the resulting computational efficiency will be of significant benefit.

In this paper, we present a pseudo-rigid body model for the analysis of the kinematics as well as the force-displacement characteristic of a spatial mechanical metamaterial. We investigate a known spatial tubular mechanical meta-



(a) (b) (c)

Figuur 3.1: The tubular mechanical metamaterial under study in this paper. Shown are a front-view (a), top-view (b) and a section containing a single hole (c). This structure has 7 holes along the height and 16 holes around the circumference. The holes are tapered such that they are round at the outer perimeter and elliptical at the inner perimeter with a constant thickness of the most slender parts between the holes.

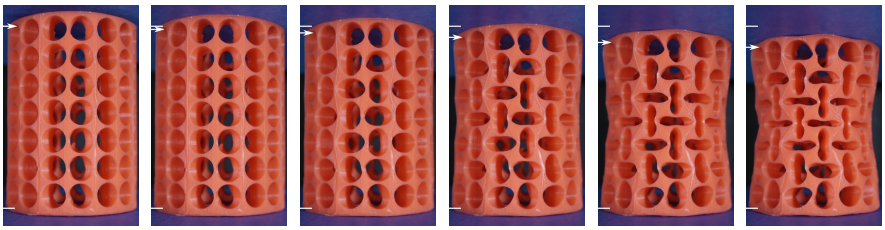
material [32–34]. This tubular structure has a negative Poisson's ratio due to a square array of round holes which is patterned around the circumference of the cylinder. The PRBM we present in this paper is able to replicate this property, as well as capturing the force-displacement behavior of the structure.

By including fixed boundary conditions, matching the clamping in the experimental setup in one of the models, we are able to model the inhomogeneously deformed shape of the elastomeric structure. This is an advantage over common unit-cell based models, where the deformations of the structure are assumed to be periodic and therefore only homogeneous deformations of the metamaterial are considered [35].

We will first describe how the tubular mechanical metamaterial deforms under uniaxial compression and indicate the geometrical features that give rise to the negative Poisson's ratio. Secondly, we present and discuss two representative spatial PRBMs for the analysis of the metamaterial, both of which share the same geometrical structure. One model describes the metamaterial under idealized conditions, while the other also considers boundary effects due to clamping. Finally, we will validate the two implemented models with experimental data.

3.2. The Elastomeric Tubular Strucutre

The tubular mechanical metamaterial under study in this paper consists of a hollow cylinder with a square array of pores around the circumference, as is



(a) dy =0mm (b) dy =1mm (c) dy =2mm (d) dy =4mm (e) dy =6mm (f) dy =8mm

Figuur 3.2: The elastomeric, porous cylinder at various stages of vertical compression dy. The height of the undeformed cylinder in these pictures is 70 mm, indicated by two white lines on the left in each picture. The arrow indicates the compressed height of the cylinder. (a) shows the undeformed structure. At low compressions (b), the whole structure undergoes a vertical strain. At higher compressions, however (c,d,e,f), a buckling transition has occurred and the holes have deformed into alternatingly oriented ellipses.

shown in Fig.3.1. Fig. 3.1a shows a front-view of the structure and Fig. 3.1b shows a top-view. Fig.3.1c shows a section of a single pore of the structure, which is circular at the outer perimeter of the cylinder and elliptical at the inner perimeter. It was made such that the holes follow the curvature of the cylinder with the wall thickness between the holes remaining constant throughout the radius of the cylinder.

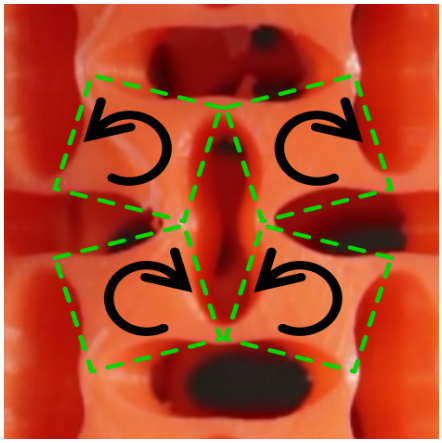
Figure 3.2 shows snapshots taken during compression of the tubular mechanical metamaterial along the cylinder's central axis. Two distinct stages can be identified in the compression characteristics:

- *Pre-buckling:* the whole structure undergoes a uniform vertical strain, the holes deform into ellipses with their largest principal axis oriented horizontally, as shown in fig. 3.2b.

- *Post-buckling:* the slender parts between the holes buckle and the pattern of holes deforms into alternatingly oriented ellipses, as shown in fig. 3.2c, d, e.

During the first stage of the compression, the slender parts between the holes undergo uniform vertical compression. The Poisson's ratio of the structure is therefore determined by the Poisson's ratio of the material. However, because the deformation is mostly localized in the slender parts, the overall structure has a Poisson's ratio close to zero.

In the second stage of the deformation, the slender parts between the holes have buckled and the holes form a checkerboard pattern of horizontally and vertically elongated ellipses. This pattern transformation causes a new deformation mode, in which the structure has a negative Poisson's ratio; the radius of the structure decreases with increasing compression along the cylinder axis. It is in this stage that the deformation of the metamaterial becomes bending-dominated.



Figuur 3.3: In the post-buckling stage of the deformation, the solid parts between the holes behave approximately as rigid square plates, and rotate in an alternating pattern. These squares are indicated with dashed lines and the direction of rotation for each of the plates is indicated by arrows.

In the post-buckling stage of the deformation, the majority of the deformation of the structure is localized in the slender parts between the holes. Therefore, the solid square parts between the holes behave approximately as rigid parts. These square parts rotate alternatingly clockwise and counter-clockwise, deforming the holes into the alternatingly oriented ellipses. This is illustrated in Fig. 3.3.

In both stages of the deformation, the overall structure of the tube remains approximately cylindrical. In previous studies of this structure, it was shown that this is the case whenever the beams between the holes are sufficiently slender with respect to the size of the holes [34].

3.3. Two Pseudo-Rigid Body Models for the Post-Buckling Behavior

In this section we introduce the spatial pseudo-rigid body models used to analyze the elastomeric tubular structure, one including the clamping of the ends, and one without clamping. Both models are based on the same mechanical structure, illustrated in Fig. 3.4a, where the clamping has been included. The structure consists of N_h layers of rigid squares. In each layer, there are N_c squares, where N_c is an even number. Within a layer, the squares are joined at their corners by spherical joints, shown in green. The centers of all squares in a layer are at a distance r_i from the central axis of the modeled cylinder and each square occupies a constant sector angle $\alpha = \frac{2\pi}{N_c}$. These values are indicated in Fig. 3.4b.

Each square in a layer can rotate about an axis normal to its surface and crossing its center. We call this rotation angle θ_i. All squares in a layer rotate

simultaneously about their respective normals by an angle $\pm\theta_i$, alternating in sign around the circumference of the cylinder. When they rotate, they move radially with respect to the cylinder axis in order to maintain the constant sector angle α. Additionally, the squares are allowed to rotate about a horizontal axis tangent to the cylinder surface and crossing the midpoint of the square by an angle ψ_i. This angle is the same for all squares in a layer. These rotation angles are illustrated in Fig. 3.4c, 3.4d. Rotations about the $\hat{z}$-axis and translations within the $\hat{x}\hat{y}$-plane tangent to the cylinder are fixed.

The radius r_i of a layer is

$$r_i = \frac{l\cos(\theta_i)}{2\sin\left(\frac{\pi}{N_c}\right)}, \tag{3.1}$$

where l is the length of the diagonal of the squares. The height of a layer, measured along the $\hat{z}$-axis is

$$h_i = l\cos(\theta_i)\cos(\psi_i). \tag{3.2}$$

The squares in consecutive layers are coupled at their corners such that these corners share their radial and $\hat{z}$ coordinates. These connections are indicated in red in Fig. 3.4. At these connections, relative displacements of the two connected corners in the $\hat{x}\hat{y}$-plane, tangent to the cylindrical surface are allowed, just as relative rotations of the squares. These connections place constraints on the angles ψ_i:

$$r_i - r_{i+1} = \frac{l}{2}\left(\cos(\theta_i)\sin(\psi_i) - \cos(\theta_{i+1})\sin(\psi_{i+1})\right), \quad \forall i \in [1, N_h - 1]. \tag{3.3}$$

The total height of the modeled structure is

$$H = \frac{h_0 + h_{N_h}}{2} + \sum_{i=2}^{N_h-1} h_i, \tag{3.4}$$

where the height of the top- and bottom layers have been halved to reflect the flat top and bottom surfaces of the elastomeric structure.

We add stiffness to the model by adding torsion springs to the connections between the squares, as illustrated in Fig. 3.5. Within a layer, we place torsion springs at each connection, oriented radially (Fig. 3.5a). For this, we define the rotation angle ϕ_i of a square, as projected along the radial line through the connection:

$$\phi_i = \arctan\left(\frac{\tan(\theta_i)}{\cos\left(\frac{\pi}{N_c}\right)}\right). \tag{3.5}$$

The energy in these torsion springs is then

$$E_h = \frac{1}{2} N_c k_R \sum_{i=1}^{N_h} (2\phi_i)^2, \tag{3.6}$$

where k_R is the stiffness of the radially oriented torsion springs.

Between the layers, we place two springs at each connection, one oriented radially and one tangent to the cylindrical surface. The stiffness of the radially oriented springs is equal to that of the previously described radial springs within a layer. The radial springs are illustrated in Fig. 3.5b. The energy in these springs is

$$E_v = \frac{1}{2} N_c k_R \sum_{i=1}^{N_h - 1} (\theta_i + \theta_{i+1})^2. \tag{3.7}$$

The energy in the torsion springs placed tangent to the cylinder is

$$E_s = \frac{1}{2} N_c k_S \sum_{i=1}^{N_h - 1} (\psi_i - \psi_{i+1})^2, \tag{3.8}$$

where k_S is the stiffness of the tangent springs. These springs are illustrated in 3.5c.

We implement the above described model in two distinct ways: a simplified 1-DOF model with free boundaries, and one with $N_h - 2$ degrees of freedom, where the boundaries are fixed. The 1-DOF model can be solved analytically and can therefore be used to obtain a quick estimate of the properties of the spatial metamaterial under idealized conditions. The second model allows us to match the boundary conditions observed in experiments and therefore represents the measurements better, at the expense of requiring numerical methods for its evaluation.

3.3.1. 1-DOF Model

In the simplified model, we take all θ_i to be equal. Therefore, the radius will be constant along the height of the modeled structure and the Poisson's ratio can then be calculated analytically:

$$\nu = -\frac{H}{r}\frac{\partial r}{\partial H} = -1. \tag{3.9}$$

Because the radius is constant along the height of the cylinder, we have $\psi_i = 0$ for all layers and the torsion springs tangent to the cylinder do not contribute to the total energy; $E_s = 0$. The energy for a state of the structure can be expressed as a function of the single variable θ:

$$E = E_h + E_v + E_s = \frac{1}{2} N_c k_R \left(N_h \left(2\phi(\theta)\right)^2 + (N_h - 1)(2\theta)^2 \right), \tag{3.10}$$

where the sums over the layers have been evaluated.

3.3.2. N_h-DOF Model

In the second model, we constrain the top and bottom boundary of the structure in the radial direction by setting $\theta_0 = \theta_{N_h} = 0$. This matches the boundary conditions observed in compression experiments of the elastomeric structure.

This model is evaluated numerically for a range of vertical strains ϵ_y. This is done by minimizing the total energy $E = E_h + E_v + E_s$ under the constraint $H = H_0(1 + \epsilon_y)$, where H_0 is the maximum height of the structure, obtained when $\theta_i = 0$ for all layers.

3.4. Pre-buckling estimation

To estimate the stiffness of the structure in the pre-buckling regime, as well as the buckling threshold, we model the structure as N_c parallel columns with each N_h serial linear springs. Therefore, if one such spring has a stiffness k_L, the total pre-buckling stiffness of the structure will be estimated as

$$k_{PB} = N_c \frac{k_L}{N_h}. \tag{3.11}$$

The reaction force of the structure in the pre-buckling stage is then

$$F_{PB} = k_{PB}(H - H_0), \tag{3.12}$$

where H is the current height of the structure and H_0 the original height.

The buckling transition is then assumed to occur at the point where the force-displacement graphs of the pre-buckling and the post-buckling model intersect.

3.5. Experimental Validaton

3.5.1. Methods

For the experimental validation of the Pseudo-Rigid Body Model, we constructed a porous cylinder with $N_h = 8, N_c = 16$, an outer radius of $25mm$, an inner radius of $16.7mm$ and a total height of $70mm$. The elastomeric structure is flat on the top and bottom. A mold was 3D printed on a Prusa i3 MK2 3D printer in PLA. The structure was then molded in a single piece using a two-part silicone rubber with a Shore-Hardness of A10 (Poly-Sil PS8510 by Poly-service BV). During the curing of the silicone rubber, it was placed under vacuum to reduce the occurence of air bubbles in the structure.

Tabel 3.1: Parameters of the PRBM for validation

Symbol	Description	Value	Unit
l	Diagonal length of the squares	9.8	mm
k_R	Stiffness of the radially oriented torsion springs	0.24e-3	$\frac{Nm}{rad}$
k_S	Stiffness of the tangentially oriented torsion springs	5.7e-3	$\frac{Nm}{rad}$
k_L	Linear stiffness of the pre-buckling springs	9.6e2	$\frac{N}{m}$
N_h	Number of squares along the height	8	
N_c	Number of squares along the circumference	16	

The structure was compressed by a universal testing machine (Zwick/Roell AG, Ulm, Germany). The cylinder was placed between two acrylic plates, which were covered in masking tape to reduce reflections. The cylinder was compressed by $8mm$, at a rate of $5mm/min$, during which a digital camera (Canon EOS 70D) was used to acquire image data. Using the image data and image recognition software (Python3 with the OpenCV2 module), the width of the central 10% of the cylinder was determined during compression.

The experimental data was compared to both models. The stiffness of the torsion springs and the pre-buckling linear springs were calculated for notch hinges with radii of 9mm, a minimum thickness of 1.13mm and a height of 8.45mm [36]. The Young's modulus of the material was taken to be $0.67MPa$. These, and other parameters for the model were measured on the silicone structure. The used values are presented in table 3.1.

3.5.2. Poisson's ratio

Figure 3.6 shows the observed radial strain ϵ_r (a) and the Poisson's ratio ν (b) plotted against the applied vertical strain ϵ_y for the experiment and the two PRBMs. In 3.6a, we see that there is an offset between the modeled and experimental strain curves. This is caused by the pre-buckling stage of the elastomeric structure, which was not taken into account in the PRBMs. Therefore, we compare the slope of the experimental curve after buckling to the modeled curves. This is best reflected by the Poisson's ratio, shown in Fig. 3.6b. To obtain the Poisson's ratio of the elastomeric structure, we fitted the radial strain with the following function:

$$f(\epsilon_y) = \begin{cases} a + b\epsilon_y + c\epsilon_y^2, & \epsilon_y < \epsilon_0 \\ a + b\epsilon_0 + c\epsilon_0^2 + d(\epsilon_y - \epsilon_0), & \epsilon_y \geq \epsilon_0 \end{cases} . \tag{3.13}$$

We fit a linear function to deformation in the pre-buckling behavior and a quadratic function to the post-buckling behavior. The Poisson's ratio is then determined as the negative derivative of this function with respect to the applied strain ϵ_y. By applying this fit, we remove the noise from the determined Poisson's ratio. The chosen function fits the experimental data with a RMS error of $6 \cdot 10^{-14}$.

In Fig. 3.6b, we see that the 1-DOF model predicts a Poisson's ratio of -1,

higher than the experimentally observed value. The N_h-DOF model matches the observed Poisson's ratio more closely, also showing an increase in its value for larger applied strains.

Figure 3.7 shows the shapes predicted by the N_h-DOF model drawn over pictures of the elastomeric structure at matching vertical strains. The model captures the hourglass-like shape observed in the deformed elastomeric structure.

3.5.3. Force-Displacement

Figure 3.8 shows the force-displacement behavior measured on the elastomeric structure and predicted by the two PRBMs. In the experiment, we observe a steep increase of the reaction force up to the buckling point, after which the force is close to constant around $3N$. Both models predict close to constant force-displacement behavior, but overestimate the total force by approximately $0.43N$ and $0.14N$, respectively. The N-DOF model predicts a lower total force because the square plates in the top and bottom layer do not rotate and therefore the torsion springs in these layers are not loaded, which is closer to reality.

In the experimental results, we observe a buckling transition at a strain of -0.03. Using the pre-buckling estimation based on linear springs, the pre-buckling stiffness of the structure is higher, leading to an estimated buckling strain of -0.01.

3.6. Discussion

The experimentally determined Poisson's ratio is lower than the value of -1 predicted in the 1-DOF model, while the N_h-DOF model matches it substantially better. Since the only difference between the two models is the inclusion of fixed boundaries in the N_h-DOF model, this suggests that the experimental boundary conditions, where the top and bottom surface of the cylinder are fixed radially due to friction, affect the Poisson's ratio significantly, decreasing its value below -1. This is confirmed by Fig. 3.7, where we see the elastomeric cylinder deform into an hourglass-like shape when compressed. In the 1-DOF model, the structure remains cylindrical, while the N_h-DOF model matches the experimental shape.

The force-displacement data of Fig. 3.8 also shows a better match between the experimental post-buckling behavior and the N_h-DOF model than it does for the 1-DOF model. Both models predict a low stiffness of the structure in the post-buckling regime, which is also observed in the elastomeric structure. The difference between the two models lies mainly in the magnitude of the force, where the N_h-DOF model predicts a lower force, which is closer to the experimentally observed values.

The observed difference between the reaction force of the elastomeric structure and that predicted by the PRBMs could also be attributable to imperfections in the elastomeric structure. The Young's modulus used to calculate the

stiffness of the joints was converted from the Shore hardness provided by the supplier of the silicone rubber and was not tested experimentally. Therefore, the elastomeric structure could have a Young's modulus different from the $0.667MPa$ used in the models. Furthermore, left-over air bubbles or an imperfect mixing of the two silicone components would also have an effect on the stiffness. A higher Young's modulus would increase the reaction forces of the elastomeric structure, while air bubbles would decrease the stiffness of the material and therefore result in lower forces.

The buckling strain is substantially overestimated by the intersection of the force-strain curves from the pre-buckling analysis and the post-buckling models. This is due to a calculated pre-buckling stiffness that is higher than the experimental values. In the calculations, it is assumed that all deformation is localized in the notch joints, just as was done for the post-buckling analysis. From the experiments, we observe that this assumption might not be valid. If there is also deformation in the square parts of the structure, the total stiffness of the structure will be lower since the deformation is more evenly spread throughout the structure. This would result in a buckling transition at lower values of the strain.

The 1-DOF PRBM presented in this paper can be solved analytically and is therefore useful to calculate a quick estimate of the properties of the metamaterial under ideal compression conditions. However, as we see in the experimental validation, it is unable to replicate the significant effects of the boundary conditions. The N_h-DOF PRBM is able to predict the post-buckling behavior of these porous elastomeric metamaterials more accurately, taking into account the fixed boundaries in our experiments. However, because of the greater complexity of this model, numerical methods were needed to obtain the shown results.

3.7. Conclusion

In this paper, we have demonstrated the application of two Pseudo-Rigid Body Models to a spatial mechanical metamaterial structure. This was done by analyzing a cylindrical mechanical metamaterial with a negative Poisson's ratio. The PRBMs used for this analysis consist of rigid squares that rotate about their normals as well as around a horizontal axis tangent to the cylindrical surface. Two PRBMs were presented, one simplified version with a single variable and one with one variable per layer of rigid squares along the height of the cylinder.

We have validated PRBMs by measuring the Poisson's ratio and force-displacement characteristic of the tubular mechanical metamaterial, molded from silicone rubber. The 1-DOF model captured the main features of the metamaterial in the post-buckling regime, predicting a negative Poisson's ratio and giving a reasonable estimate for the reaction force. However, this model was unable to include the boundary conditions introduced by clamping of the specimen in the experimental setup, causing it to underestimate the Poisson's ratio.

The second model, with N_h degrees of freedom, proved to be able to capture the experimental boundary conditions and therefore matches the observed

Poisson's ratio and force-displacement behavior of the elastomeric structure more accurately. This model was also able to match the hourglass-like shape of the deformed cylinder.

To obtain an estimation for the buckling strain of the structure, a simple model based on linear springs was used. This model overestimates the pre-buckling stiffness of the structure and therefore predicted a lower buckling strain than was observed in the experiment.

By analyzing spatial mechanical metamaterials using PRBMs, analytical equations for the effective material properties of these structures can be obtained. This greatly reduces the computational effort necessary to analyze these structures and can lead to a more intuitive evaluation of the complex deformation patterns that occur in these novel materials.

As the field of mechanical metamaterials grows towards the design of materials with tailored mechanical properties, fast evaluation of design iterations will become crucial. PRBMs, such as those shown in this paper, can greatly reduce the computational effort involved in these iterations, allowing for a more efficient design process.

Bibliografie

[1] F. G. Broeren, V. van der Wijk, and J. L. Herder, *Spatial pseudo-rigid body model for the analysis of a tubular mechanical metamaterial,* Math. Mech. Solids , 108128651987550 (2019).

[2] A. A. Zadpoor, *Mechanical meta-materials,* Mater. Horizons **3**, 371 (2016).

[3] K. Bertoldi, V. Vitelli, J. Christensen, and M. Van Hecke, *Flexible mechanical metamaterials,* Nat. Rev. Mater. **2** (2017), 10.1038/natrevmats.2017.66.

[4] X. Ren, R. Das, P. Tran, T. D. Ngo, and Y. M. Xie, *Auxetic metamaterials and structures: a review,* Smart Mater. Struct. **27**, 023001 (2018).

[5] M. N. Ali and I. U. Rehman, *An Auxetic structure configured as oesophageal stent with potential to be used for palliative treatment of oesophageal cancer; development and in vitro mechanical analysis,* J. Mater. Sci. Mater. Med. **22**, 2573 (2011).

[6] M. N. Ali, J. J. C. Busfield, and I. U. Rehman, *Auxetic oesophageal stents: structure and mechanical properties,* J. Mater. Sci. Mater. Med. **25**, 527 (2014).

[7] T. M. Cross, K. W. Hoffer, D. P. Jones, P. B. Kirschner, E. Langvin, and J. C. Meschter, *Auxetic Structures and Footwear with Soles Having Auxetic Structures,* (2016).

[8] A. Toronjo, *Articles of Apparel Including Auxetic Materials,* (2017).

[9] F. Fraternali and A. Amendola, *Mechanical modeling of innovative metamaterials alternating pentamode lattices and confinement plates,* J. Mech. Phys. Solids **99**, 259 (2017).

[10] T. A. Schaedler, A. J. Jacobsen, A. Torrents, A. E. Sorensen, J. Lian, J. R. Greer, L. Valdevit, W. B. Carter, Q. Ge, J. A. Jackson, S. O. Kucheyev, N. X. Fang, and C. M. Spadaccini, *Ultralight metallic microlattices.* Science **334**, 962 (2011).

[11] M. Rashed, M. Ashraf, R. Mines, and P. J. Hazell, *Metallic microlattice materials: A current state of the art on manufacturing, mechanical properties and applications,* Mater. Des. **95**, 518 (2016).

[12] N. Fleck, M. Ashby, and V. Deshpande, *The Topology of Cellular Structures,* in *New Approaches to Struct. Mech. Shells Biol. Struct.*, edited by H. Drew and S. Pellegrino (Kluwer Academic Publishers, 2002) pp. 81–89.

[13] V. Deshpande, M. Ashby, and N. Fleck, *Foam topology: bending versus stretching dominated architectures,* Acta Mater. **49**, 1035 (2001).

[14] L. R. Meza, A. J. Zelhofer, N. Clarke, A. J. Mateos, D. M. Kochmann, and J. R. Greer, *Resilient 3D hierarchical architected metamaterials,* Proc. Natl. Acad. Sci. U. S. A. **112**, 11502 (2015).

[15] K. Bertoldi, P. M. Reis, S. Willshaw, and T. Mullin, *Negative Poisson's Ratio Behavior Induced by an Elastic Instability,* Adv. Mater. **22**, 361 (2010).

[16] G. W. Milton, *New examples of three-dimensional dilational materials,* Phys. status solidi **252**, 1426 (2015).

[17] H. Mitschke, F. Schury, K. Mecke, F. Wein, M. Stingl, and G. E. Schröder-Turk, *Geometry: The leading parameter for the Poisson's ratio of bending-dominated cellular solids,* Int. J. Solids Struct. **100**, 1 (2016).

[18] B. Florijn, C. Coulais, and M. van Hecke, *Programmable Mechanical Metamaterials,* Phys. Rev. Lett. **113**, 175503 (2014).

[19] S. Shan, S. H. Kang, J. R. Raney, P. Wang, L. Fang, F. Candido, J. A. Lewis, and K. Bertoldi, *Multistable Architected Materials for Trapping Elastic Strain Energy,* Adv. Mater. **27**, 4296 (2015), arXiv:1207.1956 .

[20] K. Che, C. Yuan, J. Wu, H. Jerry Qi, and J. Meaud, *Three-Dimensional-Printed Multistable Mechanical Metamaterials With a Deterministic Deformation Sequence,* J. Appl. Mech. **84**, 11004 (2016).

[21] A. Rafsanjani and D. Pasini, *Bistable auxetic mechanical metamaterials inspired by ancient geometric motifs,* Extrem. Mech. Lett. (2016), 10.1016/j.eml.2016.09.001.

[22] G. F. Méjica and A. D. Lantada, *Comparative study of potential pentamodal metamaterials inspired by Bravais lattices,* Smart Mater. Struct. **22**, 115013 (2013).

[23] T. Frenzel, M. Kadic, and M. Wegener, *Three-dimensional mechanical metamaterials with a twist.* Science **358**, 1072 (2017).

[24] L. L. Howell, *Compliant mechanisms* (Wiley, 2001) p. 459.

[25] E. Turco, F. Dell'Isola, A. Cazzani, and N. L. Rizzi, *Hencky-type discrete model for pantographic structures: numerical comparison with second gradient continuum models,* Zeitschrift fur Angew. Math. und Phys. **67**, 1 (2016).

[26] J. N. Grima and K. E. Evans, *Auxetic behavior from rotating squares,* J. Mater. Sci. Lett. **19**, 1563 (2000).

[27] J. N. Grima, A. Alderson, and K. E. Evans, *Auxetic behaviour from rotating rigid units,* Phys. status solidi **242**, 561 (2005).

[28] D. Attard and J. N. Grima, *A three-dimensional rotating rigid units network exhibiting negative Poisson's ratios,* Phys. status solidi **249**, 1330 (2012).

[29] B. Deng, J. R. Raney, V. Tournat, and K. Bertoldi, *Elastic Vector Solitons in Soft Architected Materials,* Phys. Rev. Lett. **118** (2017), 10.1103/PhysRevLett.118.204102.

[30] C. G. Johnson, U. Jain, A. L. Hazel, D. Pihler-Puzović, and T. Mullin, *On the buckling of an elastic holey column,* Proc. R. Soc. A Math. Phys. Eng. Sci. **473**, 20170477 (2017).

[31] H. Tanaka, K. Hamada, and Y. Shibutani, *Transition mechanism for a periodic bar-and-joint framework with limited degrees of freedom controlled by uniaxial load and internal stiffness,* R. Soc. Open Sci. **5** (2018), 10.1098/rsos.180139.

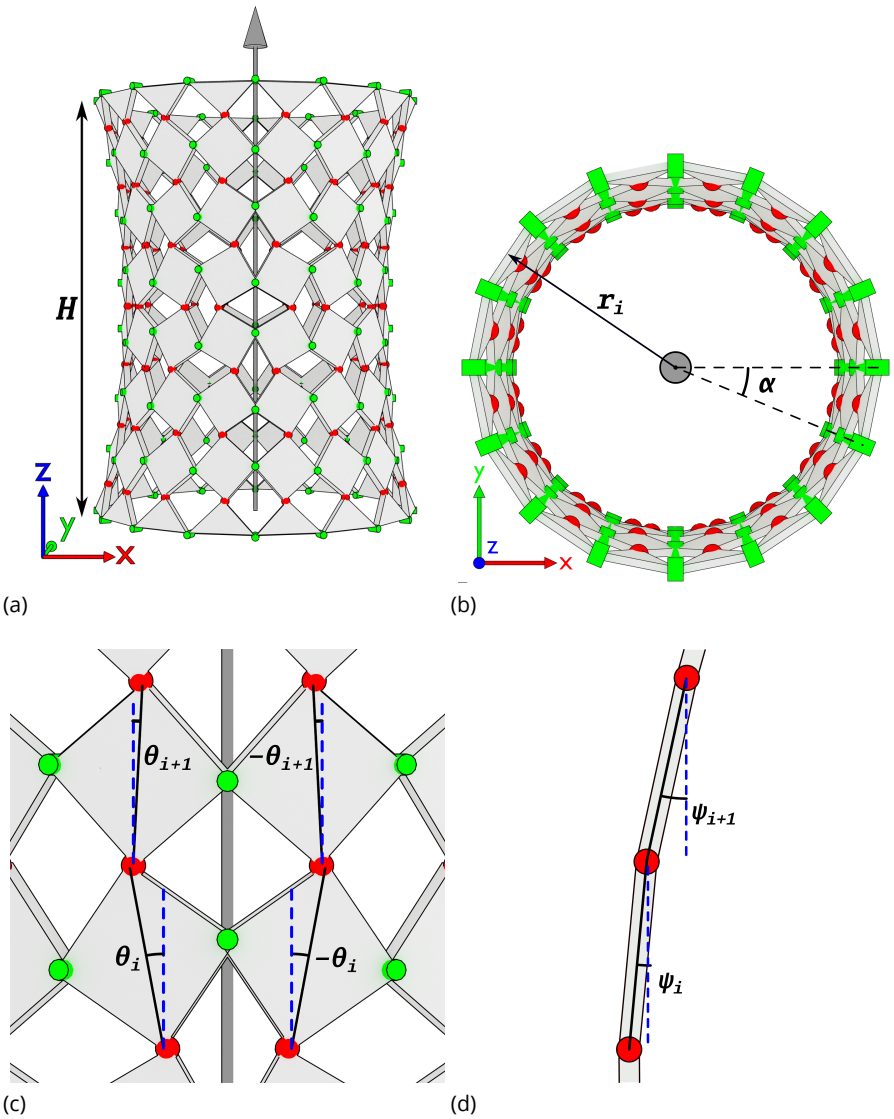
[32] A. Lazarus and P. M. Reis, *Soft Actuation of Structured Cylinders through Auxetic Behavior,* Adv. Eng. Mater. **17**, 815 (2015).

[33] X. Ren, J. Shen, A. Ghaedizadeh, H. Tian, and Y. M. Xie, *A simple auxetic tubular structure with tuneable mechanical properties,* Smart Mater. Struct. **25**, 065012 (2016).

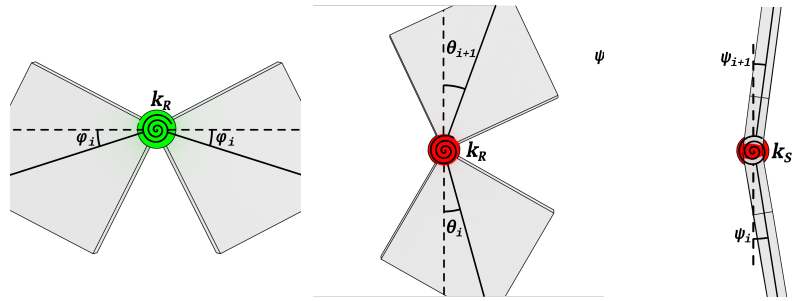
[34] F. Javid, J. Liu, J. Shim, J. C. Weaver, A. Shanian, and K. Bertoldi, *Mechanics of instability-induced pattern transformations in elastomeric porous cylinders,* J. Mech. Phys. Solids **96**, 1 (2016).

[35] R. Hutchinson and N. Fleck, *The structural performance of the periodic truss,* J. Mech. Phys. Solids **54**, 756 (2006).

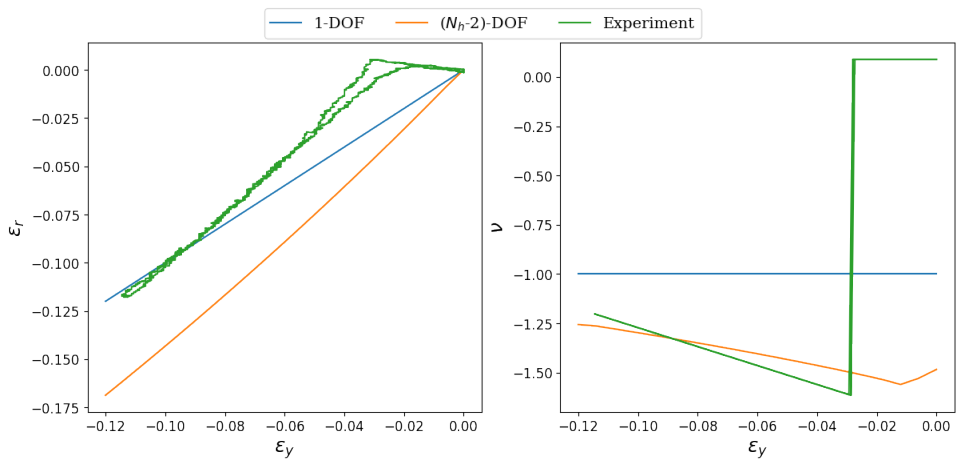
[36] H. Soemers, *Design Principles for Precision Mechanisms* (T-Point print, Enschede, 2011).



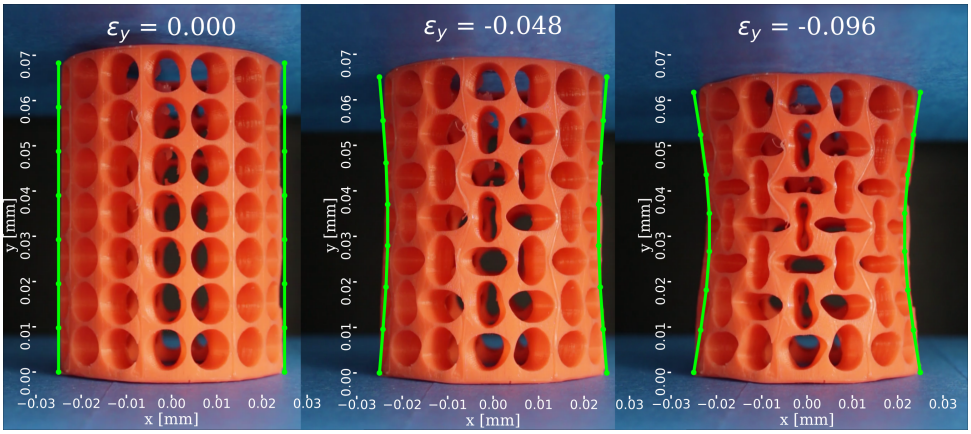
Figuur 3.4: The PRBM of the elastomeric cylindrical metamaterial structure consists of rigid squares, coupled at their corners (a). Each square occupies a fixed sector angle α around the circumference of the cylinder and is placed at a radius r_i from the cylinders central axis (b). The squares rotate by an angle θ_i around their respective normals (c). (d) shows a single column of squares from the side, indicating that the squares also rotate around a tangential axis by an angle ψ_i.



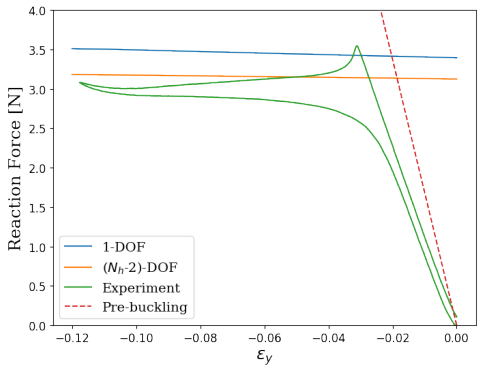
Figuur 3.5: Three types of torsion springs are used to model the stiffness of the elastomeric structure in the PRBM. In the horizontal connections (green), there are radially oriented torsion springs (a). In the vertical connections (red), there are both radially oriented (b) and tangentially oriented (c) torsion springs.



Figuur 3.6: Plots of the radial strain (left) and Poisson's ratio (right) versus the applied vertical strain on the structures. Shown are the data from the experiment (green), and the calculated values for the 1-DOF PRBM (blue) and N_h-DOF PRBM (orange).



Figuur 3.7: Three snapshots of the elastomeric structure during the compression test, with the shape calculated by the N_h-DOF model overlaid in green. The values of the applied vertical strain for each snapshot are indicated at the top of each frame.



Figuur 3.8: Plots of the force-displacement behavior of the cylindrical structure. The green line shows the experimental data. The blue and orange lines show the calculated post-buckling behavior of the structure as calculated using the 1-DOF and N_h-DOF PRBMs respectively. The red dashed line shows an approximation of the pre-buckling behavior.

4

On the Synthesis of Periodic Linkages with a Specific Constant Poisson's Ratio

Freek G.J. Broeren, Just L. Herder, Volkert van der Wijk

Poisson's ratio is one of the most studied material properties that can be designed in mechanical metamaterials. However, in most studies so far, Poisson's ratio is not constant for larger compressions. Only for structures in which ν = -1, structures with a constant Poisson's ratio have been demonstrated. This paper studies the design of planar mechanical metamaterials with a constant Poisson's ratio based on the pantograph, inversor, straight-line and parabolograph mechanisms. Using these classical mechanisms as building blocks, periodic mechanisms with ν =-1, -½, 0 and 1 are proposed.

The contents of this chapter have been published in Advances in Mechanisms and Machine Science, vol 73. (2019)[1]

4.1. Introduction

Poisson's ratio describes the deformation of a material in the directions perpendicular to a uniaxially applied load. This ratio is the subject of a large body of research into artificially designed material structures called mechanical metamaterials [2, 3]. Especially, material structures with a negative Poisson's ratio, also named auxetics [4–6], are of interest lately, because of the counter-intuitive property that they contract in the direction perpendicular to an applied uniaxial compression. This property leads to an increased shear modulus and impact resistance of these material structures [5].

One category of auxetic structures consists of periodic linkages. These built up from unit cells consisting of rigid bars or bodies, connected by hinges [7–9]. In these structures, the periodic degrees of freedom have been designed such that when one of the dimensions of the unit cell decreases, the others also decrease and vice-versa. This effect has been demonstrated for planar periodic linkages [10–12] as well as for spatial structures [13].

Poisson's ratio is an infinitesimal property; its value is defined at a state of the structure based on small deformations around that state. In most mechanical meta-materials found in literature this value is not constant for larger deformations. A noteable exception to this are structures with a constant Poisson's ratio of -1 based on rotating squares [10] or triangles [14].

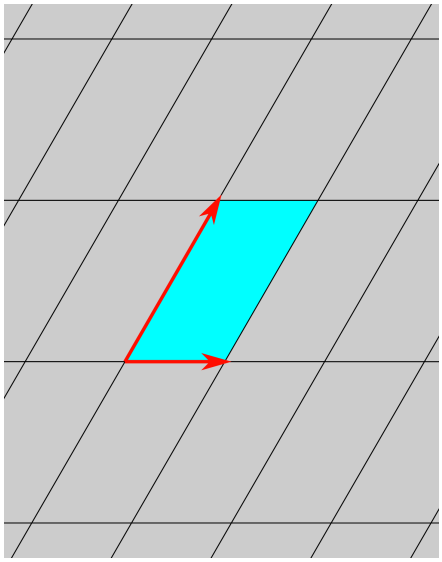
Periodic linkages could be used as a starting point for the design of elastic mechanical metamaterials. When a linkage has been designed with the desired kinematic properties, i.e. desired Poisson's ratio, then, as a next step, an elastic structure could be derived from it, obtaining a metamaterial with similar kinematic properties.

In this paper, we will show that planar periodic linkages with various constant Poisson's ratios can be created based on classical linkages, specifically, the pantograph, the inversor, the straight-line mechanism, and the parabolograph. We first determine the necessary transmission function between a vertical input and a horizontal output of a unit cell. Then, we present four periodic new linkages with constant Poisson's ratios of $-1, -\frac{1}{2}, 0$ and 1 and illustrate the connection of these periodic linkages to their classical counterparts.

4.2. Planar Periodic Linkages

Periodic linkages consist of a basic mechanism, the unit cell, which is copied along two non-parallel vectors to fill the whole plane [15, 16]. This is illustrated in figure 4.1. The unit cell of such a linkage is always a parallelogram, such that the tiling corresponds to a Bravais lattice [17].

We study a single unit cell of this structure and impose periodic boundary conditions to it to maintain connectivity between neighboring unit cells. In this paper, we only study mechanisms with a single degree of freedom, and therefore all unit cells deform in the same way. An other study [8] has investigated structures with more than one degree of freedom using Bloch-wave analysis, where the deformation patterns are still periodic, but possibly with a larger pe-



Figuur 4.1: A periodic linkage consists of a unit cell (highlighted in cyan) which is copied along two non-parallel vectors (red arrows) to fill the plane. Within this unit cell, a linkage is constructed with periodic boundary conditions, maintaining connectivity between neighboring unit cells.

riod than the constructed lattice.

4.3. Poisson's Ratio in Periodic Linkages

For materials, Poisson's ratio is defined by:

$$\nu_{ij} = -\frac{d\epsilon_j}{d\epsilon_i}, \tag{4.1}$$

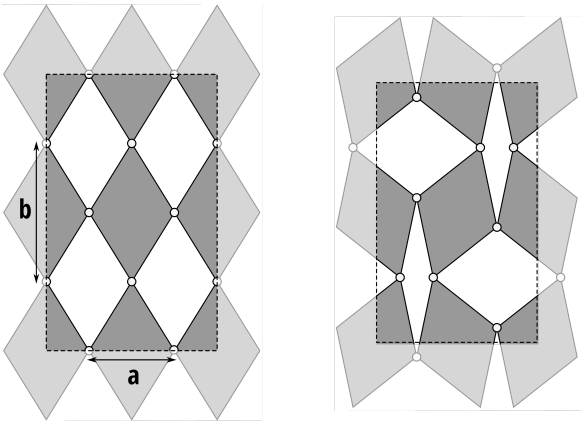
where the labels i, j denote perpendicular directions and $d\epsilon_i$ is an infinitesimal strain in the ith direction [10]. For planar periodic mechanisms, we can use the width and height of the unit cell to express a similar ratio. We follow Grima and Evans (2000) [10], and express the effective Poisson's ratio in terms of these dimensions:

$$\nu_{HW} = -\frac{H}{W}\frac{\partial W}{\partial H}, \tag{4.2}$$

where W and H are respectively the width and height of a unit cell. Using this equation, we can express the width of a unit cell as a function of its height:

$$W(H) = CH^{-\nu_{HW}}, \tag{4.3}$$

where C is an arbitrary constant. When designing a periodic linkage with a certain Poisson's ratio, we look for a linkage with this transmission between the two perpendicular directions. A useful observation here is that $\nu_{WH} = (\nu_{HW})^{-1}$,



Figuur 4.2: Four pantographs can be combined to form a unit cell with $\nu = -1$. The grey plates are rigid and allowed to hinge at their corners. The unit cell is indicated by a dashed line. This structure is adapted from [12].

so that when a periodic linkage is obtained for a specific Poisson's ratio, we automatically also obtain a linkage for the inverse Poisson's ratio by rotating the linkage by 90 degrees.

In the following, we will show how periodic linkages with a constant Poisson's ratio can be obtained from well-known planar linkages for the cases of $\nu = -1, -\frac{1}{2}, 0$ and 1.

4.3.1. ν = -1: Pantograph linkages

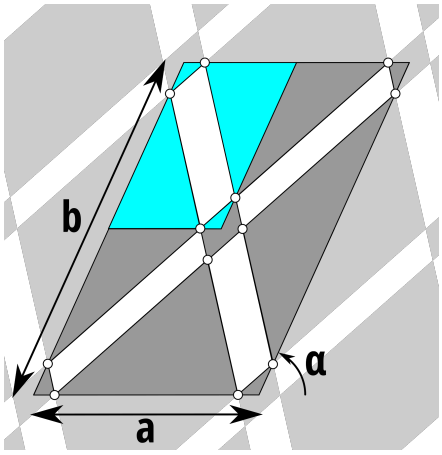
In the field of auxetics, the case of $\nu = -1$ has been widely studied because this is the limiting case for isotropic materials due to thermodynamic considerations. For these structures, the change in the width of the structure is directly proportional to the change in the height of the structure:

$$W(H) = CH, \tag{4.4}$$

where C depends on the geometry of the structure.

The shape of the unit cell does not change, but it does change in size. Therefore, the degree of freedom of such a linkage corresponds to dilation. One of the best known linkages that has this property is the pantograph [18]. Four pantograph linkages can be coupled together to form a unit cell of the structure, as is shown in figure 4.2. This structure has been described previously by Attard et al. [12]. For the drawn structure, $C = \frac{a}{b}$.

The structure in Fig. 4.2 can be generalized further to the pantographs presented in Fig. 4.3. Here, we take a parallelogram and construct a pantograph from it by following the construction described in [18]. This pantograph is then mirrored along both edges of the parallelogram to obtain a unit cell consisting of four copies of the pantograph. The rigid triangles of these pantographs are



Figuur 4.3: Proposed design of a planar parallelogram-shaped unit cell, we can construct a set of four pantograph linkages, merged together such that there is one degree of freedom for the mechanism which corresponds to $\nu = -1$. The gray faces in this drawing are rigid elements and connected by revolute joints at their corners. The pantograph in the upper left corner is highlighted.

coupled to their neighbours such that they form rigid quadrilaterals, each of them shared between four separate pantograph mechanisms. For this structure, $C = \frac{b}{a} \sin \alpha$.

4.3.2. ν = 1: Inversor linkages

For Poisson's ratio 1, the unit cell must have a constant area for the full range of motion. Then, the width of the structure can be written as:

$$W(H) = \frac{C}{H}. \tag{4.5}$$

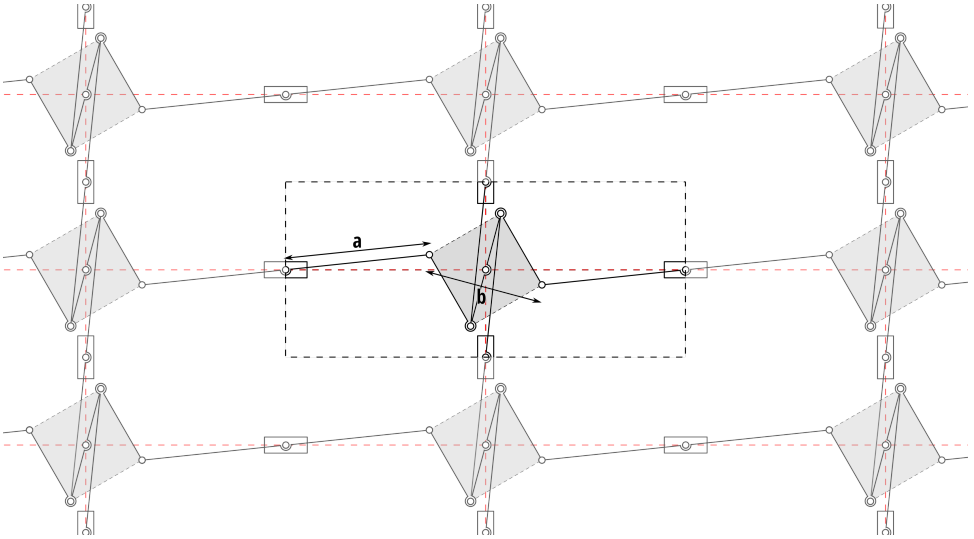
This means that the width of the structure is inversely proportional to its height,. This behavior can be achieved by using an inversor linkage [19]. Figure 4.4 presents a design of such a periodic linkage that was derived from Fig. 49 of Artobolevskii's book [19]. For this structure, $C = 4a^2 - b^2$. When the rigid squares rotate, the sliders on the edges of the indicated unit cell move such that the area of the unit cell remains constant. Therefore, the Poisson's ratio of this linkage is 1.

4.3.3. ν = 0: Straight-line mechanisms

For a Poisson's ratio of zero, there should be no dependence between the width and height of the unit cell. This can be formulated as:

$$W(H) = C. \tag{4.6}$$

For 1-DoF linkages this property is found in straight-line mechanisms. In principle, any straight line mechanisms could be used to achieve a periodic $\nu =$



Figuur 4.4: Proposed design of a periodic linkage with a Poisson's ratio of 1 based on inversor linkages. Red dashed lines indicate the slider paths. The central unit cell of the linkage is indicated with a dashed black line. The gray squares indicate rigid bodies which have a pivot at the intersection of the horizontal and vertical slider paths. The diagonals of the grey squares have length b and the four bars have length a.

0 linkage. In Fig. 4.5, we present a periodic linkage that is based on Hart's A frame. Hart's A-frame has two stationary points at the base of the A, and draws a straight line, perpendicular to the base, with its top point. We couple two of these linkages together, one rotated by 180 degrees, to form a parallelogram-shaped unit cell. When it is actuated, the corners of the unit cell will move along straight, parallel lines, thus changing the height of the unit cell while preserving its width. For the drawn structure, $C = a$.

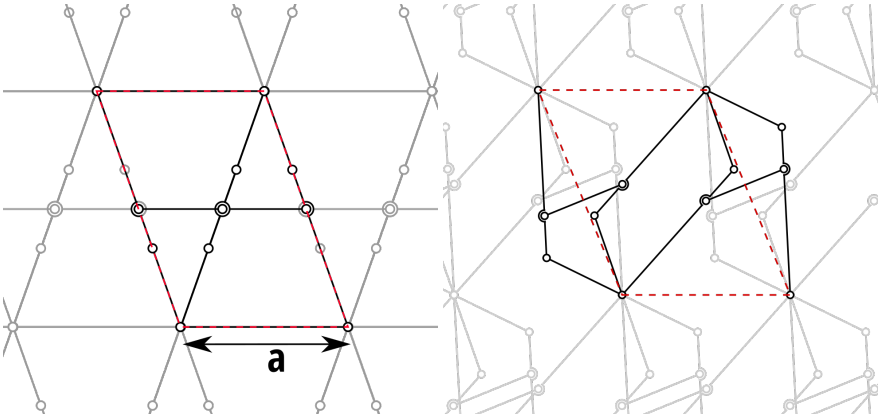
4.3.4. $\nu = -\frac{1}{2}$: Parabolograph linkages

For a Poisson's ratio of $-\frac{1}{2}$ the width of the unit cell should be given by

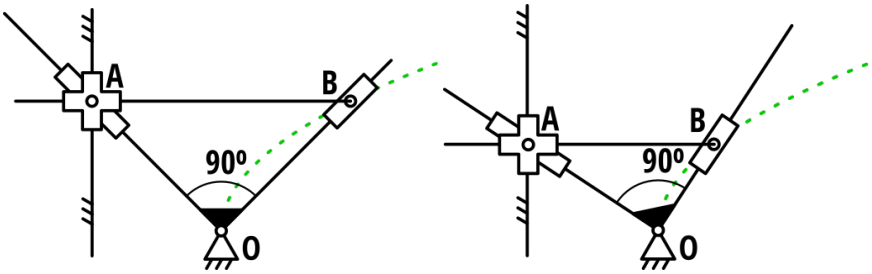
$$W(H) = C\sqrt{H}. \tag{4.7}$$

To achieve such behavior, we can use linkages from the class of Parabolographs. These are planar linkages designed to draw parabolas in the plane. Here, we will use Antonov's parabolograph (see p. 132 of Artobolevskii's book [19] for more information on this mechanism).

Antonov's parabolograph consists of three moving links, connected by revolute and prismatic joints to form a one-degree of freedom mechanism. This mechanism is shown in Fig. 4.6. When the angular link in this mechanism rotates around point O, point A moves along the vertical guide and point B follows the parabolic curve indicated by the green dotted line.



Figuur 4.5: Proposed design of a periodic linkage with $\nu = 0$, based on Hart's A-frame. Shown are two configurations within its range of motion. The unit cell is indicated by the red dotted line and drawn with black lines, The rest of the lattice is drawn in gray. When this linkage moves, the height of the unit cell decreases, but its width remains the constant distance a.

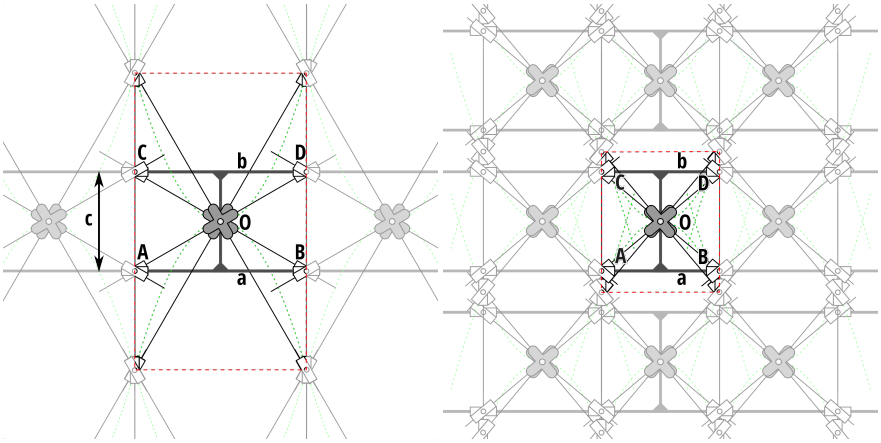


Figuur 4.6: Antonov's Parabolograph in two different configurations. Point O is fixed to the ground, point A is fixed to a vertical line. When actuated, Point B moves along a parabolic path, indicated by the green dotted line. Figure adapted from Fig. 215 in Artobolevskii's book [19]

If we take the distance AB of this mechanism to be proportional the width of the unit cell and vertical distance between points O and A to be proportional to the height of the unit cell, we obtain a unit cell with a Poisson's ratio equal to $-\frac{1}{2}$. In this case, $C = \sqrt{\frac{c}{2}}$, where c is the distance between lines a and b.

We can mirror this linkage along both the vertical and horizontal axes to obtain the tileable version presented in Fig. 4.7. Here, the horizontal lines labeled a and b indicate guides for the sliding connections and the central unit cell is indicated by a dashed red line. This linkage has been rotated by 90 degrees with respect to Fig. 4.6 to achieve $\nu_{HW} = -\frac{1}{2}$.

When actuated, the four corners of the unit cell follow parabolic curves, such that $H \propto W^2$.



Figuur 4.7: Proposed design of a periodic linkage based on Antonov's Parabolograph with a constant Poisson's ratio of $-\frac{1}{2}$. Two different configurations are shown. The unit cell is indicated by a dashed red line, the corners of this unit cell follow the green dashed parabolic paths. The points A, B, C and D slide over lines a and b. Point O is situated at the center of the unit cell. The two crossed bars pivot around this point.

4.4. Discussion

In this paper, we have shown how classical linkages, specifically the pantograph, inversor, straight-line mechanisms and the parabolograph, can be used to create periodic linkages with various constant effective Poisson's ratios. We have presented designs for a constant Poisson's ratio of $-1, -\frac{1}{2}, 0$ and 1. We are, however not limited to these examples. The curves required to obtain these values of ν can be generated by a number of different linkages, which then can be converted into a variety of periodic counterparts.

It is interesting to note from equation 4.3 that all negative integer Poisson's ratios can be achieved by linkages drawing mononomial curves, the existence of which have been proven generally by Kempe in 1875[20]. Consequently, linkages with $\nu = -\frac{1}{n}$ also exist for every positive integer n and can be obtained by rotating the linkage with $\nu = -n$ by 90 degrees. Versions of these periodic linkages with positive Poisson's ratio could be obtained by integrating an inversor within the design.

For pantograph-based linkages with $\nu = -1$, it has been shown that the kinematics can be matched by an elastic structure with a square array of round holes[21, 22]. This could significantly simplify the manufacturing for these metamaterials. Similarly, elastic structures could be designed to match the kinematics of the linkages shown in this paper. If the designs in this paper are best suitable for this and how sliders could be desgigned elastically was not yet investigated.

4.5. Conclusion

In this paper, we have presented 4 designs of periodic mechanisms with a constant effective Poisson's ratio of $-1, -\frac{1}{2}, 0$ and 1. These mechanisms were constructed based on the pantograph, inversor, straight-line and parabolograph linkage, respectively, which were adapted and tiled in a periodic grid. In this way, infinitely large linkages are constructed with a specified expansion or contraction in the horizontal direction as a response to a vertical actuation.

We have shown that it is possible to create periodic mechanisms for a variety of constant Poisson's ratios, where, in current literature, this has only been demonstrated for $\nu = -1$. In the discussion, we have indicated how linkages with other constant Poisson's ratios can be constructed using a similar approach to the one presented in this paper.

These mechanisms could, in future work, be implemented in monolytic, elastic structures with the specified Poisson's ratio that remains constant for large deformations. In this way, artificial materials can be constructed with predictable and tailored material properties that stay constant for large deformations.

Bibliografie

[1] F. G. J. Broeren, J. L. Herder, and V. van der Wijk, *On the Synthesis of Periodic Linkages with a Specific Constant Poisson's Ratio,* (Springer, Cham, 2019) pp. 249–257.

[2] A. A. Zadpoor, *Mechanical meta-materials,* Mater. Horizons **3**, 371 (2016).

[3] K. Bertoldi, V. Vitelli, J. Christensen, and M. Van Hecke, *Flexible mechanical metamaterials,* Nat. Rev. Mater. **2** (2017), 10.1038/natrevmats.2017.66.

[4] K. E. Evans, *Auxetic polymers: a new range of materials,* Endeavour **15**, 170 (1991).

[5] H. A. Kolken and A. A. Zadpoor, *Auxetic mechanical metamaterials,* RSC Adv. **7**, 5111 (2017).

[6] X. Ren, R. Das, P. Tran, T. D. Ngo, and Y. M. Xie, *Auxetic metamaterials and structures: a review,* Smart Mater. Struct. **27**, 023001 (2018).

[7] J. N. Grima, A. Alderson, and K. E. Evans, *Auxetic behaviour from rotating rigid units,* Phys. status solidi **242**, 561 (2005).

[8] R. Hutchinson and N. Fleck, *The structural performance of the periodic truss,* J. Mech. Phys. Solids **54**, 756 (2006).

[9] C. S. Borcea and I. Streinu, *Auxetics Abounding,* in *Proc. 4th IEEE/IFToMM Int. Conf. Reconfigurable Mech. Robot.*, June (Delft, the Netherlands, 2018) pp. 20–22.

[10] J. N. Grima and K. E. Evans, *Auxetic behavior from rotating squares,* J. Mater. Sci. Lett. **19**, 1563 (2000).

[11] J. . N. Grima, R. Gatt, A. Alderson, and K. E. Evans, *On the potential of connected stars as auxetic systems,* Mol. Simul. **31**, 925 (2005).

[12] D. Attard and J. N. Grima, *Auxetic behaviour from rotating rhombi,* Phys. status solidi **245**, 2395 (2008).

[13] D. Attard and J. N. Grima, *A three-dimensional rotating rigid units network exhibiting negative Poisson's ratios,* Phys. status solidi **249**, 1330 (2012).

[14] J. N. Grima and K. E. Evans, *Auxetic behavior from rotating triangles,* J. Mater. Sci. **41**, 3193 (2006).

[15] C. S. Borcea and I. Streinu, *Periodic frameworks and flexibility,* Proc. R. Soc. a-Mathematical Phys. Eng. Sci. **466**, 2633 (2010).

[16] E. Ross, B. Schulze, and W. Whiteley, *Finite motions from periodic frameworks with added symmetry,* Int. J. Solids Struct. **48**, 1711 (2011).

[17] C. Kittel, *Crystal Structure,* in *Introd. to solid state Phys.* (Wiley, Hoboken, NJ :, 2005) Chap. 1. Crystal, p. 680.

[18] E. Dijksman, *Motion geometry of mechanisms.* (Cambridge University Press, Cambridge, UK, 1976).

[19] I. I. Artobolevskii, *Mechanisms for the generation of plane curves*, edited by W. M. C. o. S. Johnson and Technology) (Pergamon Press, 1964) p. 278.

[20] A. B. Kempe, *On a General Method of describing Plane Curves of the n^{th} degree by Linkwork,* Proc. London Math. Soc. **s1-7**, 213 (1875).

[21] T. Mullin, S. Deschanel, K. Bertoldi, and M. C. Boyce, *Pattern Transformation Triggered by Deformation,* Phys. Rev. Lett. **99** (2007), 10.1103/PhysRevLett.99.084301.

[22] K. Bertoldi, M. Boyce, S. Deschanel, S. Prange, and T. Mullin, *Mechanics of deformation-triggered pattern transformations and superelastic behavior in periodic elastomeric structures,* J. Mech. Phys. Solids **56**, 2642 (2008).

5

Mechanical Metamaterial With Poisson's Ratio Close to 1 Based on the Inversor Linkage

Freek G.J. Broeren, Just L. Herder, Volkert van der Wijk

Numerous mechanical metamaterials are designed to have a specific Poisson's ratio. Only a few of them, however, can maintain a constant Poisson's ratio for a large range of motion. In this paper, we present 3 designs of a mechanical metamaterial based on the inversor linkage. These have a near-constant Poisson's ratio of 1 for a large range of motion. This is mainly attributed to the constant transmission between the perpendicularly oriented input and output points of the inversor linkage.

Of the 3 designs, there is one with a single layer, one with two layers and one with four layers. With an increase in layers, the complexity of the design increases. The three designs were 3D printed and experimentally verified. This shows that, for this design, with increasing complexity the range in which its Poisson's ratio remains constant also increases.

The contents of this chapter have been submitted to Mechanism and Machine Theory

5.1. Introduction

Mechanical metamaterials are mechanical structures with have effective bulk material properties that are different from their constituent materials due to their geometry. By using structural design, the effective Young's modulus and Poisson's ratio of these metamaterials can be designed to be significantly different from the materials they are made of, even extending beyond the values found in nature [1–3].

How mechanical metamaterials obtain their distinctive properties often blurs the lines between mechanisms and materials. A large class of metamaterials are the bending-dominated mechanical metamaterials[4, 5], which rely on the bending of internal slender elements for their function. By designing the internal structure of the material carefully and changing the thickness of the internal elements, bending can be localized. These metamaterials are very similar to compliant mechanisms [6]. Design methods from this field, like pseudo-rigid body modeling [7] and rigid-body replacement [8] can therefore be used in the design of bending-dominated metamaterials.

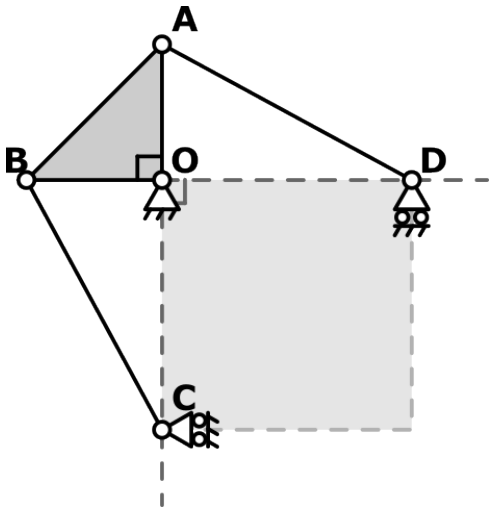
In order to be used as a material, it is necessary that a mechanical metamaterial can be shaped and divided without losing its bulk mechanical properties. To achieve this, their structure is often periodic. They consist of multiple identical elements, called unit cells, which are copied and translated to fill space. This method has the advantage that only the single unit cell, with periodic boundary conditions to account for interactions, is of concern. Because of the periodicity of the lattice, the bulk properties are ensured to be equal to those of the single unit cell[9].

Within mechanical metamaterial research, especially Poisson's ratio has received considerable interest [10–13]. This ratio determines the strain of the material in the direction perpendicular to an applied uniaxial strain. Almost all natural materials have a positive Poisson's ratio, meaning that they contract in the direction perpendicular to an applied strain. Steel and rubber, for example, have Poisson's ratios around 0.3 and 0.5, respectively.

In a previous paper[14], we have shown that the effective Poisson's ratio of a periodic linkage can be designed based on classical linkages. The kinematics of these linkages directly dictate the effective Poisson's ratio. By choosing a linkage that describes a mononomial curve of the form $y = x^{-\nu}$, and using that linkage as the unit cell of a periodic mechanism, space-filling structures can be created that have a constant Poisson's ratio ν for their complete range of motion.

In this paper, we will look at the case where $\nu = 1$. The corresponding curve $y = \frac{1}{x}$ is described by an inversor linkage. We will show how this linkage can be converted into a periodic mechanism and how this periodic mechanism can in turn be used to create a monolithic compliant metamaterial.

We present three iterations of monolithic designs based on the inversor linkage. Each of these designs relies on the bending of internal elements to produce a designed Poisson's ratio. The first design is fully planar, but only approximates the kinematics of the inversor linkage. Therefore, Poisson's ratio



Figuur 5.1: The inversor linkage consists of a single triangular body and two moving links. When actuated, the area of the rectangle spanned by points O, C and D remains constant. This rectangle is indicated in light grey.

for this structure deviates from the desired value of 1 for larger deformations. The other designs consist of multiple layers, which opens up space for designs that maintain their Poisson's ratio for a larger range of motion.

The designs have been 3D printed and tested under compression to verify the resulting effective Poisson's ratio. We show that, while all three have a Poisson's ratio equal to the designed value of 1 at the construction position, only one design maintains this ratio for larger deformations. This design has the highest degree of symmetry of the three presented designs and maintains its Poisson's ratio up to applied compressive strains of 8%.

5.2. The inversor linkage

The metamaterial lattices developed in this paper are based on the inversor linkage shown in Figure 5.1. This linkage has been adapted from the inversor presented in Artobolevskii (1964 p.24, Fig.49)[15]. It consists of one right-triangular rigid body OAB and two moving links AD and BC. Point O is connected to the ground by a revolute joint and points C and D are attached to the ground by perpendicularly oriented sliders with a revolute joint. Links AD and BC are connected to the triangular body with revolute joints in A and B. We will call the distance OD the width W of this linkage and the distance OC the height H of the linkage.

Characteristic for this inversor is that for the complete range of motion of this linkage, the product $\mathcal{P}$ of the height (OC) and width (OD) remains constant. Therefore, the width of the linkage can be written as:

$$W = \frac{\mathcal{P}}{H}, \tag{5.1}$$

Hence, if we consider W and H as the respective width and height of a unit cell of a periodic linkage, we can calculate the effective Poisson's ratio as follows[14]:

$$\nu = -\frac{H}{W}\frac{\partial W}{\partial H} \tag{5.2}$$

$$= 1. \tag{5.3}$$

5.3. Periodic linkage design

In order to transfer the behavior of the previously described linkage to a mechanical metamaterial, additional changes to the linkage are needed. These additional changes serve two purposes:

1. They allow the linkage to be tiled in the plane such that the resulting periodic linkage has a single degree of freedom
2. They remove the sliders from the linkage, as these are more difficult to replicate in a compliant structure.

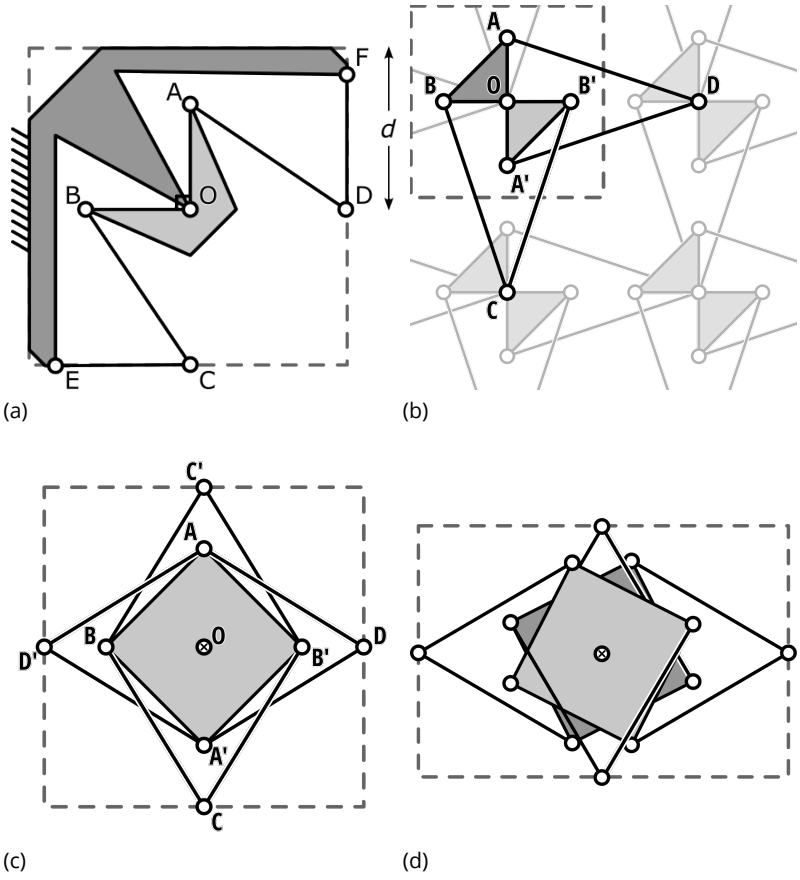
There is no unique approach to satisfy these two requirements. Therefore, we present three distinct adaptations of the linkage presented in Section 5.2. These adaptations are shown in Figure 5.2 and will be discussed in the following subsections. Each of these adaptations satisfies both requirements.

5.3.1. Design 1: Single layer

In the first design, we have prioritized a planar resulting linkage. This design is shown in Figure 5.2a.

In this design, a large body OEF has been added which acts as the ground of the linkage. This body has been designed to provide support for the hinges at O, E and F, while providing as much open space as possible for the rest of the moving links. The right triangular body OAB has been adapted to completely lie within the open space left by the ground body. The moving links AD and BC have not been changed and fit within the open space. The two sliders connecting points C and D to the ground have been replaced by the links CE and DF, respectively. These links approximate the straight-line motion of the points C and D for small displacements around the position shown in Figure 5.2a.

The resulting linkage forms a square unit cell which can be tiled in space by connecting the joint C to the top edge of the neighbouring ground body and the joint D to the left edge of its neighbouring ground body. A vertical translation of the point C with respect to the origin O will therefore be transferred to the unit cell below it and a horizontal translation of the point D with respect to O will be transferred to the unit cell to its right.



Figuur 5.2: Three adaptations of the original linkage design in Figure 5.1 from Section 5.2. Each adaptation can be tiled in the plane and has a single degree of freedom when tiled. Panels (a) and (b) show a single-layer and double-layer design, respectively. Panels (c) and (d) show a four-layer design in two states within its range of motion. Grey dashed lines have been used to indicate the unit cell for each linkage.

With this design, an offset has been introduced between the central rotation point O and the left and top sides of the unit cell. This will affect the effective Poisson's ratio of the periodic lattice. In Figure 5.2a, the offset has been indicated in the vertical direction and labelled as d. When we assume that this offset is equal for both the vertical and horizontal directions, the Poisson's ratio of this design becomes:

$$H' = H + d \tag{5.4}$$
$$W' = W + d \tag{5.5}$$
$$= \frac{\mathcal{P}}{H} + d \tag{5.6}$$
$$\nu = -\frac{H'}{W'}\frac{\partial W'}{\partial H'} \tag{5.7}$$
$$= \frac{H + d}{H + \frac{d}{\mathcal{P}}H^2} \tag{5.8}$$

Therefore, Poisson's ratio for this periodic linkage will no longer be constant and will only be equal to 1 for small displacements around the construction position.

5.3.2. Design 2: Two layers

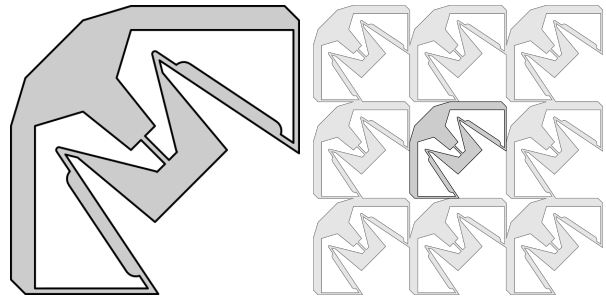
A second design, which can be constructed in two layers, is shown in Figure 5.2b. In this design, the original inversor has been modified by mirroring the links OA and AD along the vertical axis and the links OB and BD along the horizontal axis. This creates the new points A' and B'. By connecting these points, a new right-triangular rigid body $OA'B'$ is formed. This coupling ensures that the resulting linkage again has a single degree of freedom.

The resulting linkage consists of two coupled four-bar linkages. The symmetry in the linkage ensures that the lines OC and OD remain perpendicular throughout its range of motion. A periodic linkage can be obtained by coupling the point D to the origin of the unit cell to the right and coupling point C to the origin of the unit cell below it. This has been indicated in Figure 5.2b, where the neighbouring unit cells have been greyed-out. This coupling does not introduce an offset between the unit cells, so this design is expected to perform as in Equation (5.2).

5.3.3. Design 3: Four layers

In the final design, we aimed to simplify the coupling between the unit cells. This was done in a design that can be constructed in four layers, as is shown in Figures 5.2c and 5.2d.

In this design, additional symmetry with respect to the second design is introduced by mirroring the design along the horizontal and vertical axes. The resulting consists of two square plates which are connected by a hinge at their



Figuur 5.3: A compliant mechanical metamaterial based on the inversor linkage. (a) shows a single unit cell. (b) shows this unit cell tiled in a 3 × 3 grid.

centres (indicated by a circle with a cross in Figure 5.2c) and eight moving links. The components form four coupled four-bar linkages with a single degree of freedom. Throughout its motion, the linkage maintains a left-right and an up-down symmetry.

The unit cell of this design is described by the rectangle passing through points C, D, C' and D'. The tiling of these unit cells can be performed by coupling point D of the unit cell to point D' of its neighbour to the right and by coupling point C of the unit cell to point C' of its bottom neighbour.

Comparing this design to the original inversor from Figure 5.1, we see that both the width and the height of the unit cell have doubled. This does not affect Poisson's ratio so this design is expected to behave as in Equation (5.2).

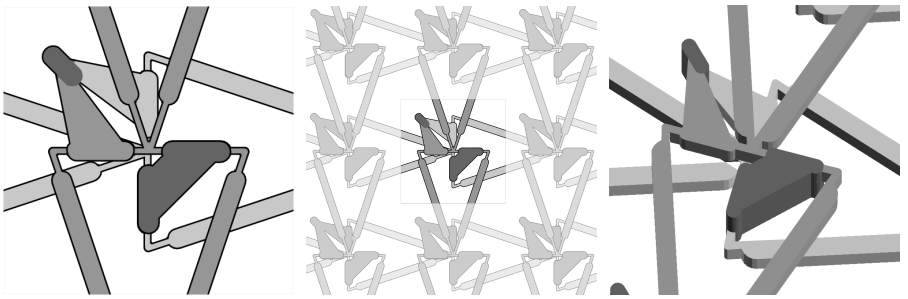
5.4. Compliant Designs

In each case, the monolithic compliant designs are created using a Rigid Body Replacement method[8]. Using this method, the joints are replaced by slender beams while the rigid links become thicker elements.

5.4.1. Compliant Design 1: Single Layer

For the single-layer design, the compliant embodiment is shown in Figure 5.3a. In this embodiment, the hinges at the points O, A, B have been replaced with relatively short thin beams. Because of their short length, the possible deformations in these beams will closely resemble the hinge rotations of the original linkage. The links CE and DF have been completely replaced by long slender beams.

Figure 5.3b shows a tiling of 9 compliant unit cells. The rigid ground body at the left and upper boundary of each unit cell has been shaped to give the long slender beams sufficient space to bend.



(a) (b) (c)

Figuur 5.4: A compliant mechanical metamaterial based on the inversor linkage built up in two layers. (a) shows a single unit cell. (b) shows this unit cell tiled in a 3 × 3 grid. (c) shows a 3D view of the structure, further highlighting the layers. The two layers are colored different light- and medium-grey. The parts in a dark-grey cross between the two layers.

5.4.2. Compliant Design 2: Two Layers

The design with two layers is shown in Figure 5.4. The hinges at A, B, A' and B' have been replaced by short slender beams, similar to the single-layer design. At point O, however, a total of six beams come together in two separate layers. To accommodate this within the available space, the top-left triangular body has been reshaped. It now consists of one part in the top layer and a second part in the bottom layer. These parts are connected by a body in the top-left of the unit cell which spans both layers.

The tiling of this unit cell into a grid of 9 unit cells is shown in Figure 5.4b.

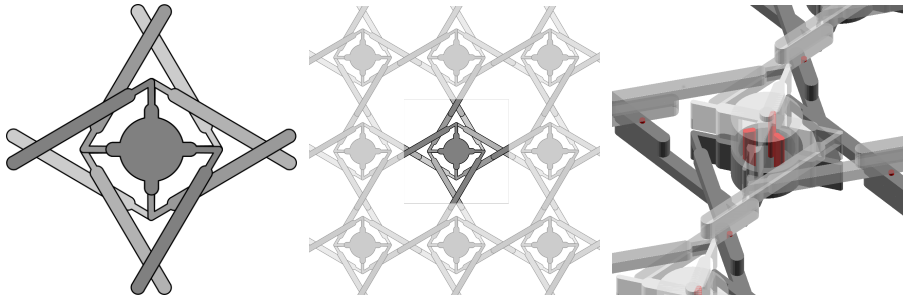
5.4.3. Compliant Design 3: Four Layers

The compliant embodiment of the four-layer design is shown in Figure 5.5. At the points A, B, A' and B', the hinges have been replaced by short slender beams as before. At the four sides of the unit cell, points C, D, C' and D' the hinge is replaced by a thin cylinder between the layers for torsional deflection. At the centre of the unit cell, point O of the linkage, the two square rotating bodies have been replaced by cylinders. These cylinders are connected at their centres by a set of three leaf flexures, which replace the revolute joint connecting the square bodies and allow rotational motion. These connections are shown in Figure 5.5c.

The unit cells of this design combine into a periodic metamaterial as shown in Figure 5.5b. At the sides of the connecting unit cells, the rigid bars of the neighbouring unit cells are joined rigidly and form a kind of scissor mechanism. This enhances the coupling of the motion of one unit cell to the next.

5.5. Experimental Verification

In order to test the performance of the metamaterial designs, they have been manufactured and their Poisson's ratio has been measured experimentally. In



(a) (b) (c)

Figuur 5.5: A compliant mechanical metamaterial based on the inversor linkage built up in four layers. (a) shows a single unit cell. (b) shows this unit cell tiled in a 3×3 grid. (c) shows a 3D view of the structure, where the connections between the layers have been highlighted in red. The four layers have been drawn in different shades of grey.

this section, we detail the experimental methods used and share the results.

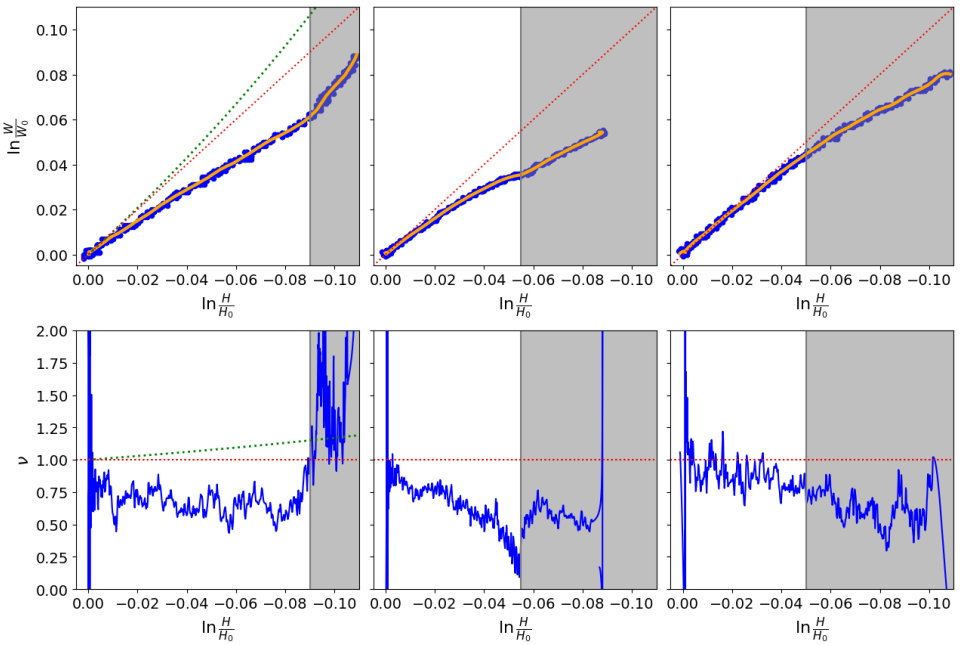
5.5.1. Methods

The three mechanical metamaterials described in the previous sections were 3D printed in *Ultrasinth TPU-90A* using *Multi-jet fusion* by Materialise[16]. For each of the three designs, a 5×5 grid of unit cells was printed, with a unit cell size of 35 mm square. The thickness of each printed sheet was 10 mm. Protruding cylinders were added to the top surfaces of the metamaterials. These were colored yellow using acrylic paint in order to be used as markers for the image processing of the measurements.

The structures were compressed in a Zwick-Roell universal test bench up to a strain of 10%. During compression, the structures were filmed using a digital camera (Canon EOS 70D). The recorded movies were processed using Python and OpenCV[17]. In order to prevent out-of-plane buckling of the structures and to study their planar behavior, they were placed between two sheets of transparent acrylic during the experiments.

The colored markers were used to track the unit cell deformations of the structure throughout the experiments. By calculating the distance between the markers, the height and width of the unit cells was determined. To minimize the effect of the boundaries, only the positions of the central markers were used to determine the deformations of the metamaterials. Deformations are presented as logarithmic (Hencky) strains, as the natural extension to large deformations of the infinitesimal strains used in Section 5.2.

The Poisson's ratio was determined from the measured data by first applying a Savistky-Golay filter to the raw data. The Poisson's ratio was then calculated as minus the derivative of this smoothed curve.



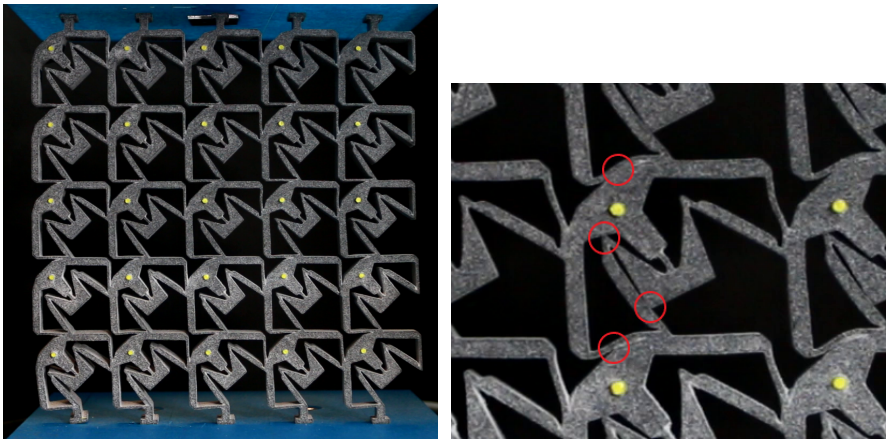
Figuur 5.6: Logarithmic strains (top) and effective Poisson's ratio (bottom) for each of the three compliant metamaterial designs. The data is plotted with the applied logarithmic strain $\ln \lambda_H$ on the horizontal axis. The orange line in the strain plots has been obtained by applying a Savitsky-Golay filter on the raw data. This filtered data has been used to obtain the effective Poisson's ratio in the bottom panes. Red dotted lines indicate the desired $\nu = 1$ behavior, the green dotted lines indicate the expected behavior from the design with an offset. Parts of the graphs where undesired behavior is caused by self-collision or shearing are indicated by grey shading.

5.5.2. Results

Figure 5.6 shows the resulting strains and effective Poisson's ratios from the measurements on the three different designs. In these figures, the red dashed lines correspond to a Poisson's ratio of 1, the blue dots are the measured values, and the orange line indicates the smoothed data that was used to determine Poisson's ratio.

The results from the single-layer design quickly deviate from the $\nu = 1$ line. We see a significant deviation in the measured strain for most of the measured range. The effective Poisson's ratio lies around 0.75 for most of the measured range and shows only slight fluctuations around this value. This deviation can not be explained by the offset d of 15 mm, as we observe by comparing the experimental results with the green dotted line in Figure 5.6. We also see a steep increase in Poisson's ratio around 9% compressive strain. This is likely caused by internal collisions within the structure, as can be seen in Figure 5.7.

For the two-layer structure, the initial Poisson's ratio is close to 1, but it quickly deviates from this value. Additionally, around an applied strain of 5.5%, a discontinuity is observed in the effective Poisson's ratio. The observed devia-



(a) (b)

Figuur 5.7: The measured sample of the single layer design. (a) shows the structure before compression. (b) shows a state where the applied strain is around 9% and internal collisions occur. Four points of internal collision have been indicated with red circles.

tions are likely caused by shearing of the sample for larger deformations. This effect can be observed in the photo's from the experiments shown in Figure 5.8. In the ideal lattice, all yellow dots would form vertical lines. In the compressed state of Figure 5.8, the top and bottom layers have visibly shifted.

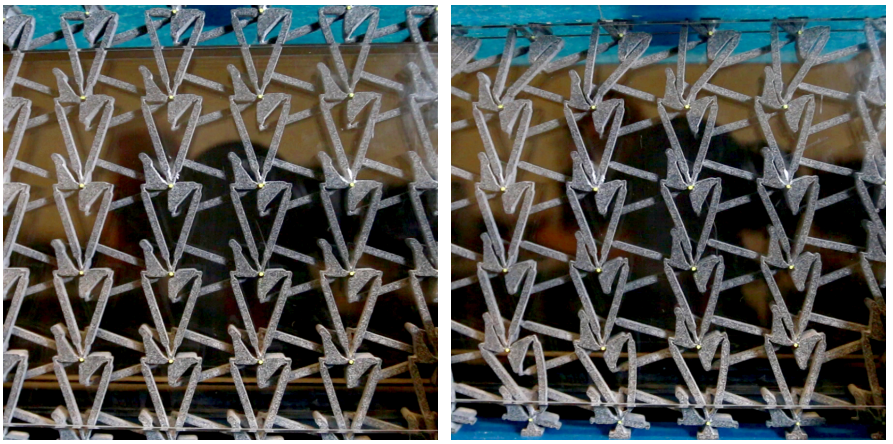
The third structure has an effective Poisson's ratio close to 1 up to an applied strain of 5%, at which point internal collisions occur and the measured strains start to deviate from the expected line. These internal collisions can be observed in the photo's from the experiments shown in Figure 5.9

5.6. Discussion

When designing a mechanical metamaterial to have a specific Poisson's ratio, linkages can be used as a starting point. In these linkages, Poisson's ratio can be designed as a geometric transmission ratio between two perpendicular motions [14].

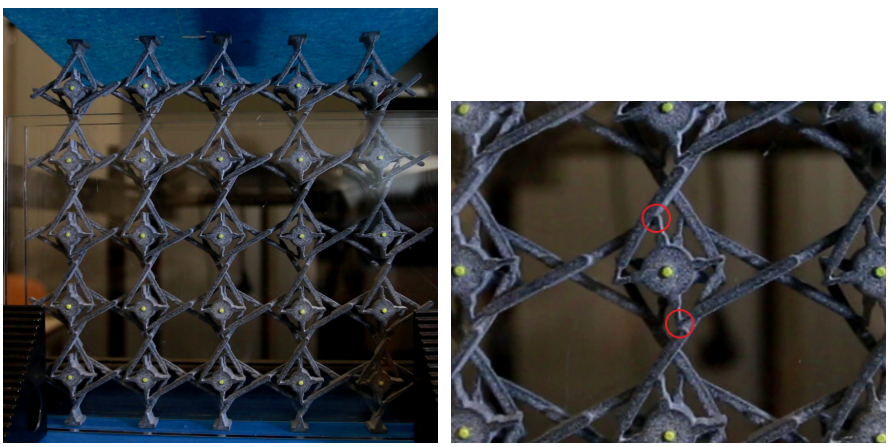
Starting from a single linkage design, we have demonstrated three possible monolithic designs. All three designs were based on the inversor linkage and were thereby designed to have a Poisson's ratio of 1 up to large deformations.

The first design was completely planar and thereby the easiest to manufacture. For consistency with the other samples, additive manufacturing was used, but more conventional 2D manufacturing techniques like laser cutting or CNC would also have been suitable. However, this design introduced an offset d between the unit cells that led to a deviation from the designed Poisson's ratio for finite deformations. At the construction position, the metamaterial had a Poisson's ratio close to 1, but it quickly deviates from the designed value for larger deformations. However, we do see a near-constant Poisson's ratio of 0.75



(a) (b)

Figuur 5.8: The two-layer design in the initial (a) and compressed (b) state. Shearing can be observed in the top and bottom layers of the deformed state, causing the columns of yellow dots to no longer form vertical lines.



(a) (b)

Figuur 5.9: The four-layer second design in the initial (a) and compressed (b) state. In the compressed state, internal collisions can be observed. Two points of internal collision have been indicated with red circles.

for this design up to a strain of 9%, where self-collision occurs. The observed deviation between the designed Poisson's ratio of 1 and the actual ratio of 0.75 can not be explained by the offset d, as we see in Figure 5.6. This suggests that this planar design introduces additional deviations from the kinematic model which have not been taken into account.

The second design consists of two moving layers and thereby eliminated the offset between the unit cells. However, during the compression, the structure deformed by shearing rather than uniform compression, leading to a lower-than-designed Poisson's ratio.

The last design consists of four moving layers, allowing for a four-fold symmetry of the unit cell. Due to this symmetry, the metamaterial deformed more uniformly during compression and the effective Poisson's ratio was close to 1 up to 5% compressive strains, after which internal collisions caused deviations from the predicted behavior.

The differences between the second and third compliant designs show the importance of symmetry when designing periodic mechanical materials. Both kinematic structures have a single degree of freedom and are expected to perform equally well. However, the experiments show that in the second design a shearing deformation occurred, making the measured properties of the metamaterial deviate from the designed values. In the third design, this behavior was not observed, likely due to the four-fold symmetry in the unit cells of the structure distributing the actuation forces equally in all directions.

Additionally, we have seen that, while the inversor linkage can achieve the desired Poisson's ratio of 1 up to 100% compression, the physical embodiments can not due to intersections between their components. With the structures demonstrated in this paper, Poisson's ratio was shown to be constant up to 5% for the four-layer sample. Further optimization is likely to further increase this allowable compression range.

5.7. Conclusion

In this paper, we have developed three monolithic and compliant realizations of a periodic mechanical metamaterial with a Poisson's ratio of 1, based on the inversor linkage. While all three realizations originated from the same linkage, both their shapes and their performance has been shown to differ significantly. We have shown how the linkage can be converted to form the unit cell of a periodic linkage and have demonstrated different approaches to converting the linkage into a monolithic compliant mechanism. This has resulted in three designs. The first consists of a single layer, but includes an offset that changes the effective Poisson's ratio. The second consist of two layers of overlapping parts and the third design consists of four layers of overlapping parts.

The three distinct realizations differed in complexity and performance. For small deformations, all three mechanical metamaterials demonstrated a Poisson's ratio close to 1. However, large differences were observed for increasing deformations. Of the three tested designs, only the design with a four-fold symmetric unit cell demonstrated the desired Poisson's ratio over large defor-

mations up to 5% compressive strain.

With this paper, we have demonstrated how classical linkages and transmissions can be used to create monolithic metamaterials with a specifically designed Poisson's ratio. While this paper has focused on the inversor linkage and, therefore, a Poisson's ratio of 1, a similar approach could be used to create metamaterials with different Poisson's ratios. The unique aspect of metamaterials designed in this way is that they can have a constant value of Poisson's ratio for large deformations, something that is not often seen in the existing literature.

Bibliografie

[1] A. A. Zadpoor, *Mechanical meta-materials,* Mater. Horizons **3**, 371 (2016).

[2] K. Bertoldi, *Harnessing Instabilities to Design Tunable Architected Cellular Materials,* Annu. Rev. Mater. Res. **47**, 51 (2017).

[3] M. Kadic, G. W. Milton, M. van Hecke, and M. Wegener, *3D metamaterials,* Nat. Rev. Phys. **1**, 198 (2019).

[4] N. Fleck, M. Ashby, and V. Deshpande, *The Topology of Cellular Structures,* in *New Approaches to Struct. Mech. Shells Biol. Struct.*, edited by H. Drew and S. Pellegrino (Kluwer Academic Publishers, 2002) pp. 81–89.

[5] V. Deshpande, M. Ashby, and N. Fleck, *Foam topology: bending versus stretching dominated architectures,* Acta Mater. **49**, 1035 (2001).

[6] L. L. Howell, *Introduction to compliant mechanisms,* in *Handbook of Compliant Mechanisms* (John Wiley & Sons, Ltd, 2013) Chap. 1, pp. 1–13, https://onlinelibrary.wiley.com/doi/pdf/10.1002/9781118516485.ch1 .

[7] F. G. Broeren, V. van der Wijk, and J. L. Herder, *Spatial pseudo-rigid body model for the analysis of a tubular mechanical metamaterial,* Math. Mech. Solids , 108128651987550 (2019).

[8] C. A. Mattson, *Synthesis through rigid-body replacement,* in *Handbook of Compliant Mechanisms* (John Wiley & Sons, Ltd, 2013) Chap. 8, pp. 109–121.

[9] R. Hutchinson and N. Fleck, *The structural performance of the periodic truss,* J. Mech. Phys. Solids **54**, 756 (2006).

[10] K. E. Evans, *Auxetic polymers: a new range of materials,* Endeavour **15**, 170 (1991).

[11] K. Bertoldi, P. M. Reis, S. Willshaw, and T. Mullin, *Negative Poisson's Ratio Behavior Induced by an Elastic Instability,* Adv. Mater. **22**, 361 (2010).

[12] H. Mitschke, F. Schury, K. Mecke, F. Wein, M. Stingl, and G. E. Schröder-Turk, *Geometry: The leading parameter for the Poisson's ratio of bending-dominated cellular solids,* Int. J. Solids Struct. **100**, 1 (2016).

[13] H. A. Kolken and A. A. Zadpoor, *Auxetic mechanical metamaterials,* RSC Adv. **7**, 5111 (2017).

[14] F. G. J. Broeren, J. L. Herder, and V. van der Wijk, *On the Synthesis of Periodic Linkages with a Specific Constant Poisson's Ratio,* (Springer, Cham, 2019) pp. 249–257.

[15] I. I. Artobolevskii, *Mechanisms for the generation of plane curves*, edited by W. M. C. o. S. Johnson and Technology) (Pergamon Press, 1964) p. 278.

[16] Materialise, NV, *Online 3D Printing | 3D Prototypes | Materialise OnSite,* (2015).

[17] G. Bradski, *The OpenCV Library,* Dr. Dobb's Journal of Software Tools (2000).

6

Auxetic interval determination and experimental validation for a three-dimensional periodic framework

Ciprian S. Borcea, Freek G.J. Broeren, Just L. Herder, Ileana Streinu, Volkert van der Wijk

Auxetic behavior refers to lateral widening upon stretching or, in reverse, lateral shrinking upon compression. When an initially auxetic structure is actuated by compression or extension, it will not necessarily remain auxetic for larger deformations. In this paper, we investigate the auxetic range in the deformation of a periodic framework with one degree of freedom. We use geometric criteria to identify the interval where the deformation is auxetic and validate these theoretical findings with compression experiments on sample structures with $10 \times 10 \times 10$ *unit cells.*

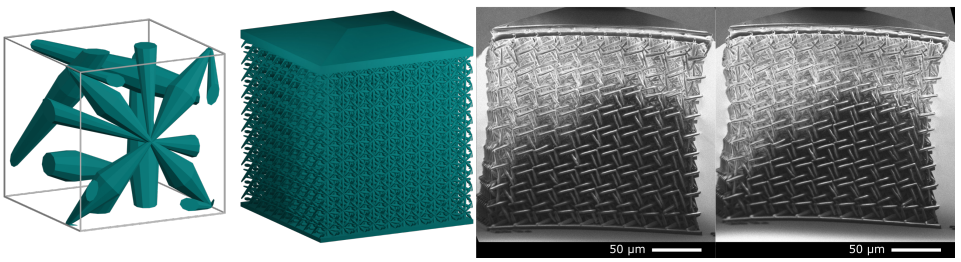
The contents of this chapter have been published in Mathematics and Mechanics of Solids (2022) [1]

6.1. Introduction

Auxetic structures have the curious property that they shrink in all directions under uniaxial compression and widen in all directions under stretching. Early considerations on this type of behavior appeared in [2–5]. Foam structures reported by Lakes [6] kindled wider interests in cellular and periodic designs which exhibit *auxetic deformations* [7, 8]. The scope of investigations and proposed applications can be gleaned from a string of reviews [9–16]. Advances in additive manufacturing have permitted the fabrication of increasingly complex and intricate structures [17–21], leading to a renewed emphasis on rational design. As observed in [22], "the rational design of metamaterials with a target property or functionality remains fiendishly difficult, and many designs so far have relied on luck and intuition".

In this paper, we focus on periodic bar-and-joint frameworks with auxetic behavior. Structures of this type, also referred to as a "rods and hinges lattices", "metamaterials of rigid bars and pivots", or simply "trusses", have been frequently used in investigations concerned with the geometric underpinnings of auxetic deformations [23–27]. We note, in this context, that crystalline materials provide a vast array of periodic bar-and-joint frameworks, also called "crystal structures" or "crystal nets" [28–31]. Displacive phase transitions, occurring under variations of temperature or pressure, can oftentimes be modeled as periodic framework deformations [32–34] and inquiries about auxetic behavior have been conducted for various structures [35–38].

Materials which can be modeled as periodic bar-and-joint frameworks allow a direct comparison of theoretical predictions with experimental results, thereby offering a more precise understanding of the fundamental role of geometry in functional responses. For auxetic behavior, there is a strictly mathematical theory, developed in [39–41], which gives necessary and sufficient conditions for the existence of auxetic infinitesimal deformations and leads to a comprehensive design methodology. Since auxetic behavior is necessarily confined to a limited range, these results bring to the fore the problem of identifying, in the global deformation space of a periodic framework, all regions where auxetic deformations are possible [42].



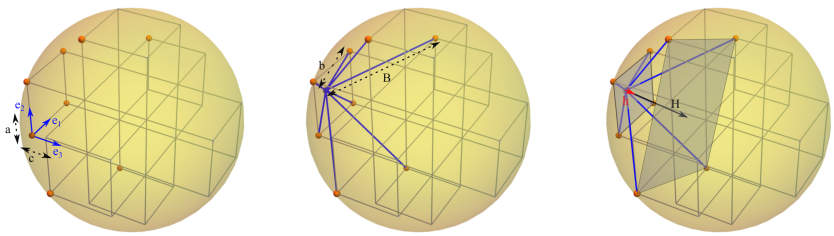
Figuur 6.1: The framework used in compression experiments. Description and dimensions are given in the text. See also Fig. 6.6

In the present study, we explore the long-range behavior of a three-dimensional periodic framework with one degree of freedom, introduced in [43]. Figure 6.1 illustrates the sample structure produced for experiments and an actual response recorded for compression. We determine the entire deformation path of the framework and recognize auxeticity along a limited arc of this trajectory. The auxetic interval of the framework is obtained through rigorous geometric calculations. The existence of this interval is then validated through experiments on 3D printed structures with $10 \times 10 \times 10$ unit cells measuring $200\mu m$ in total side length. These structures are compressed and the lateral deformation is measured through computer vision.

In our concluding section, we elaborate on the significance of one degree of freedom framework designs and the importance of the notion of auxetic interval, which allows a numerical comparison of auxetic performance for different frameworks in this class via the *volume increase factor* for the unit cells at the endpoints of the interval.

6.2. The Periodic Framework

The specific periodic framework considered here belongs to a family of designs presented in [43]. It is obtained from the diagram shown in Fig. 6.2. On the left, we see a fragment of a cubic lattice consisting of seven cubes inside a sphere passing through the twenty-four outlying corners. In the middle, the image shows an octet of lattice points chosen from these corners and connected by edges to an additional vertex placed on the sphere. This common vertex of the eight edges is chosen along the axis running through the center of the sphere and the centers of the two squares determined by the octet of lattice points. This gives a rotational symmetry of order four to the generating configuration and we use the expression 'four-fold symmetry' to refer to the resulting crystallographic symmetry of the periodic framework.



Figuur 6.2: Design diagram of the periodic framework. The unit vectors e_1, e_2 and e_3, forming an orthonormal basis, as well as the distances a, b, B, c, h and H are indicated.

The periodicity lattice is $2\mathbb{Z}^3$, consisting of all vectors in Euclidean three-dimensional space with even integers as coordinates. Thus, the side length of the cubes depicted in the sphere is 2 and the radius of the sphere is $\sqrt{11}$. The

four short edges have squared length $b^2 = 22 - 6\sqrt{11}$ and the four long edges have squared length $B^2 = 22 - 2\sqrt{11}$.

6.2.1. The global deformation space

The geometric model assumes all edges of the framework to be rigid bars and all joints to allow free relative rotation of the incident bars. The initial configuration of this periodic framework then has one degree of freedom and the deformation mechanism can be visualized and described by taking into account the preservation of the four-fold rotational symmetry. The vectors e_1, e_2, e_3 denote the standard orthonormal basis of our Euclidean three-dimensional space. The symmetry axis remains fixed along the e_3 direction and the one-parameter deformation is obtained by the variation of the periodicity lattice which keeps the direction of the initial periodicity generators $2e_1, 2e_2, 2e_3$ and keeps the first two generators of equal length. In other words, the initial cubic cell determined by the generators evolves into an orthogonal box which maintains square faces normal to the symmetry axis direction (e_3). We let a denote half the edge length of the square face and let c denote half the edge length of the third periodicity generator (with direction e_3). Thus, the initial configuration has $a = c = 1$.

When the framework moves along its deformation path, it suffices to describe what happens to the eight-bar configuration depicted in Fig. 6.2. We observe that the common vertex remains along the fixed axis and the four ends of the short bars form a square of edge length $2a$ with center on the axis and normal to the axis. The four ends of the long bars are the vertices of a square with center on the axis, normal to the axis and the distance between the planes of these two squares is $2c$.

If we denote by h the distance of the common vertex to the center of the first square and by H the distance to the center of the second square, we have:

$$h^2 = b^2 - 2a^2 \tag{6.1}$$

$$H^2 = B^2 - 10a^2 \tag{6.2}$$

We note that a is constrained to remain in the interval $(0, b/\sqrt{2}]$, since $0 \leq h^2 < b^2$. The relation between a and c depends on whether the common vertex is between the two squares or not (as in the initial configuration). Thus

$$c = \frac{1}{2}(H \pm h) = \frac{1}{2}[\sqrt{B^2 - 10a^2} \pm \sqrt{b^2 - 2a^2}] \tag{6.3}$$

which implies the algebraic relation:

$$(4c^2 - 8a^2 + B^2 - b^2)^2 - 16c^2(B^2 - 10a^2) = 0 \tag{6.4}$$

Considering that the Gram matrix ω for the periodicity generators is diagonal, with entries $\omega_{11} = \omega_{22} = 4a^2$ and $\omega_{33} = 4c^2$, we see via (6.4) that the Gram matrix trajectory is the arc of the conic

$$Q(\omega_{22}, \omega_{33}) = (\omega_{33} - 2\omega_{22} + B^2 - b^2)^2 - 2\omega_{33}(2B^2 - 5\omega_{22}) = 0 \tag{6.5}$$

where $\omega_{22},\ \omega_{33} > 0$. This arc of a hyperbola is shown in Fig. 6.4(a).

6.2.2. Geometrical determination of the auxetic interval

The detection of the precise interval where the deformation is auxetic will illustrate the geometric criteria established in [39, 40]. In particular, auxetic behavior requires, for all pairs of orthogonal directions, simultaneous elongation, or, under compression, simultaneous shrinking. Computationally, we have to see where a and c increase or decrease at the same time. Since the derivative of $c(a)$ is negative when the common vertex is between the two squares, we are left with the alternative

$$c(a) = \frac{1}{2}(H - h) = \frac{1}{2}[\sqrt{B^2 - 10a^2} - \sqrt{b^2 - 2a^2}] \tag{6.6}$$

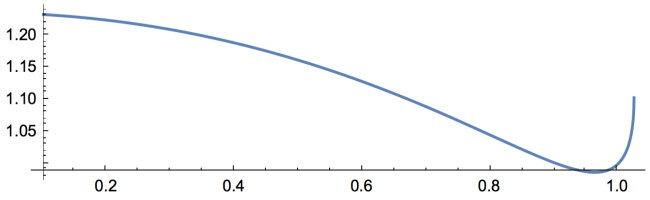
Figure 6.3 shows the graph of this function. We have

$$c'(a) = -5a(B^2 - 10a^2)^{-1/2} + a(b^2 - 2a^2)^{-1/2} = -\frac{5a}{H(a)} + \frac{a}{h(a)} \tag{6.7}$$

There is one critical point in $(0, b/\sqrt{2})$, namely

$$a_0 = \sqrt{\frac{1}{10}(132 - 37\sqrt{11})} \approx 0.963581 \tag{6.8}$$

and (6.7) is negative to the left and positive to the right of a_0.



Figuur 6.3: The graph of $c(a)$ in (6.6), for $a \in (0, 1.02476)$.

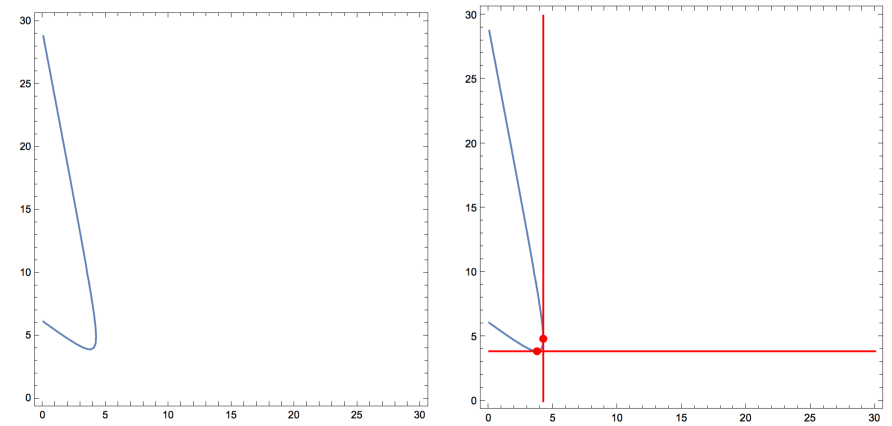
The *auxetic interval* is where $a \in [a_0, b/\sqrt{2}] \approx [0.963581, 1.02476]$ and c is given by (6.6). The (a, c) pairs at the endpoints are:

$$(\sqrt{\frac{1}{10}(132 - 37\sqrt{11})}, 2\sqrt{\frac{1}{5}(7\sqrt{11} - 22)}) \approx (0.963581,\ 0.986458) \tag{6.9}$$

$$(\sqrt{11 - 3\sqrt{11}}, \sqrt{7\sqrt{11} - 22}) \approx (1.02476,\ 1.10289) \tag{6.10}$$

The auxetic interval can be retrieved based on the *directions of the tangents to the Gram matrix trajectory* given above in (6.5) and shown in Figure 6.4. By [39], the auxetic locus is where the tangents have directions belonging to the *positive*

semidefinite cone of 3×3 symmetric matrices. Our trajectory lies in the plane $\omega_{11} = \omega_{22}$, $\omega_{ij} = 0$, for $i \neq j$, whose intersection with the positive semidefinite cone corresponds with $\omega_{22},\ \omega_{33} \geq 0$.



(a) (b)

Figuur 6.4: Gram matrix trajectory in $(\omega_{22}, \omega_{33})$ coordinates, with auxetic interval between points with horizontal and vertical tangent.

Thus, in Fig. 6.4, the auxetic interval can be visualized as the *arc between the points of the trajectory where the tangent is horizontal and then vertical*. These points correspond to

$$\frac{\partial Q}{\partial \omega_{22}} = 0, \quad \text{respectively} \quad \frac{\partial Q}{\partial \omega_{33}} = 0 \tag{6.11}$$

We find

$$3\omega_{33} = 2(B^2 - b^2) - 4\omega_{22}, \quad \text{respectively} \quad \omega_{33} = B^2 + b^2 - 3\omega_{22} \tag{6.12}$$

and this determines the endpoints of the *auxetic interval* on the Gram matrix trajectory as

$$(\omega_{22}, \omega_{33}) = (\frac{2}{5}(132 - 37\sqrt{11}), \frac{16}{5}(7\sqrt{11} - 22)) \approx (3.71395, 3.8924) \tag{6.13}$$

$$(\omega_{22}, \omega_{33}) = (44 - 12\sqrt{11}, 28\sqrt{11} - 88) \approx (4.2005, 4.86549) \tag{6.14}$$

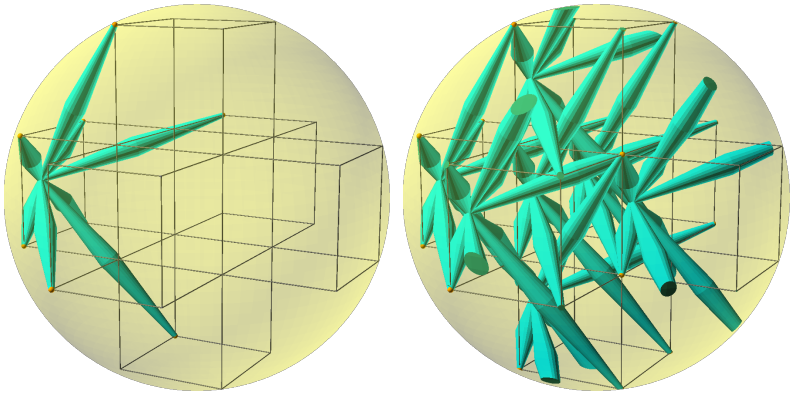
Fig. 6.4 shows the auxetic arc of the trajectory between these two endpoints. The relation $(\omega_{22}, \omega_{33}) = (4a^2, 4c^2)$ allows an easy comparison with the (a, c) points in (6.9) and (6.10) and we conclude that our two descriptions of the auxetic window agree.

6.3. Experimental Methods

6.3.1. Structure Design

From the framework blueprint described above, a monolithic design was created. The design process is illustrated in Fig. 6.5.

To create a monolithic sample of the framework, each of the edges in the blueprint shown in Fig. 6.2 is replaced by a bicone, as shown in Fig. 6.5a. By doing this, we obtain a fundamental unit consisting of eight bicones connected in a single point. We can then replicate this fundamental unit and translate it along the vectors of the periodicity lattice, as illustrated in Fig. 6.5b, to obtain the complete monolithic structure.



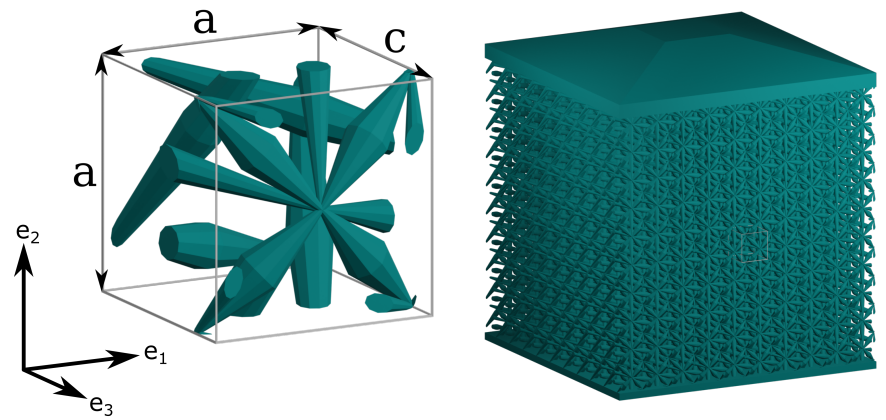
(a) (b)

Figuur 6.5: The monolithic implementation of the periodic framework is developed in two steps. First, the edges in the blueprint of Fig. 6.2 are replaced by bicones (a). Secondly, the eight bicones that make up a fundamental unit are copied and translated along the vectors of the periodicity lattice to generate the periodic structure (b).

The monolithic structure was realized with edge lengths of $b = 14.5\mu m$ for the short edges and $B = 39.2\mu m$ for the long edges, resulting in $a = c = 20\mu m$ in the initial configuration. The bicones that replace each of the edges have a small diameter of $0.5\mu m$ at their ends and a large diameter in the middle of $4\mu m$. The unit cell of the periodic framework was repeated 10 times along each of the periodicity generators to create a structure with 1000 unit cells in total, arranged into a cube. On the bottom of this cube, a plate with a thickness of $5\mu m$ was placed to ensure a level surface, and on the top a flattened pyramid was placed. The resulting unit cell and the complete sample structure are shown in Fig. 6.6.

6.3.2. Sample Creation

All sample structures were manufactured using 2-photon lithography on a Nanoscribe Photonic Professional GT (Nanoscribe GmbH, Eggenstein-Leopoldshafen, Germany), using IP-Dip photoresin on a silicon substrate. This machine



Figuur 6.6: The designed periodic framework. (a) shows a single unit cell, with the unit cell volume outlined by grey lines. The dimensions a and c are indicated along the corresponding sides of the cubic unit cell and the corresponding unit vectors e_i are indicated separately. (b) shows the complete 1000-unit cell structure, with a plate on the bottom for adhesion and a shallow pyramid on the top for probe alignment.

is capable of a lateral resolution of $200nm$ and can create structures up to $400\mu m$ high. The printed structures were sputter-coated with approximately $4nm$ of gold-palladium in order to image them in a Scanning Electron Microscope (SEM).

After creating and testing the structures, it was observed that the plates on the top and botom of the structures appear slightly curved and the central part of the structure is already slightly less wide than the top and bottom parts. This is likely an effect of the shrinkage of the used resin, which is reported to be up to 10% [44]. As we describe in subsection 6.3.4, a central region of the structure is measured to decrease the effect of these boundaries.

6.3.3. Sample Testing

Two uniaxial load cases are considered. One where a uniaxial deformation is applied along the four-fold symmetry axis i.e. along direction e_3. In this case, c is the driving parameter. For this load case, the four viewing directions normal to the faces are equivalent and the lateral deformation of a can be measured as a response to a deformation in c.

In the other load case, the structure is uniaxially deformed along direction e_2, perpendicular to the symmetry axis and a is the driving parameter. There are two distinct side-views for this case, one along e_3, where we view the deformation of the second side marked a under compression and one along e_1, where the deformation in c is visible.

Three structures were constructed, one for each testing orientation. The

two structures to be compressed along e_2 were constructed identically, with the only difference being a 90 degree rotation of the complete structure (including plates) along the axis normal to the substrate.

The structures were compressed using a Femtotools FT-NMT03 nanomechanical testing system inside of a Jeol JSM-6010LA Scanning Electron Microscope. For the compression tests, a silicon microforce sensing probe with a tip width of $50\mu m$ was used. The probe was centered on the structures by aligning it with the flattened pyramid. The structures were compressed at a rate of $0.1\mu ms^{-1}$. Every $0.2\mu m$ of travel, the probe was stopped and the SEM was used to record a high-resolution (5120x3840px) image. Each compression step corresponds to 0.1% of applied strain to the structure.

6.3.4. Experimental probing of the auxetic interval

Because of the four-fold rotational symmetry described in section 2, the auxetic interval can be determined by measuring the effects of applied deformations on the distances a and c. For each compression test, the structure is imaged from the side, allowing two dimensions to be measured during the deformation, one of which is always the driving parameter.

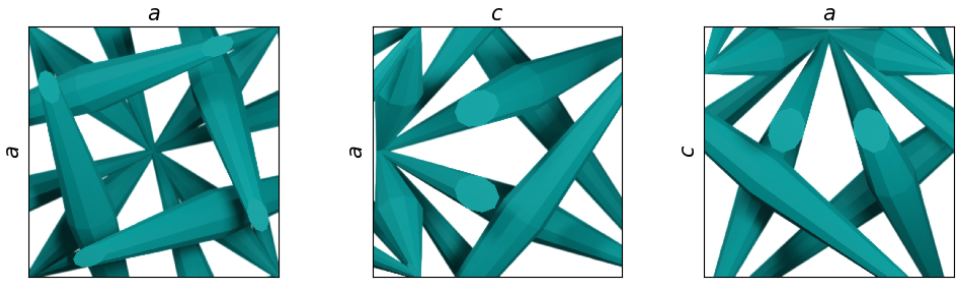
Fig. 6.7 shows a unit cell of the framework under the three different viewing directions. The distance labels a and c can be seen next to the respective sides of the frames.

We observe that, according to Fig. 6.3, when a is actuated, the allowed compression is relatively large, while when c is actuated, the allowed compression of the sample is limited to about 1.35%. Up to this limit, a point on the motion path corresponding to this compression can be found. Beyond this limit, no such point can be found and the framework can therefore no longer respect the intended structural design. In experiments, this will result in deformations which significantly or severely violate the rigid-bar assumption. Therefore, when probing the auxetic interval experimentally, applied strains larger than 1.35% along c do not reflect the theoretical structure in a meaningful way. In our test, we have compressed the structure slightly further to ensure that the full range of motion was measured in the selected region, considering that the deformations are not distributed equally throughout the structure.

6.3.5. Data Processing

The recorded images were used to obtain quantitative data on the strains in the compressed structures. First, the images were rotated and straightened to correct for perspective. To do this, four points on the structure were selected and transformed to span a square.

The images were then processed using digital image correlation. The deformations were tracked in a central region of the structure, consisting of 6x4 unit cells, to mitigate the effects of the boundaries. This region was tracked using Gunnar Farneback's algorithm, as implemented in OpenCV 3.2.0 [45, 46]. Using this algorithm, the displacements of each pixel in the region are calculated. We use these displacements to calculate the local strains in the tracked region and



Figuur 6.7: Schematics of the three distinct viewing directions of the structure that are used in this study. The images show an orthographic view of a single unit cell of structure and the relevant dimensions a and c are marked on the sides of the images.

average this over the region to obtain the horizontal and vertical strains.

6.4. Results

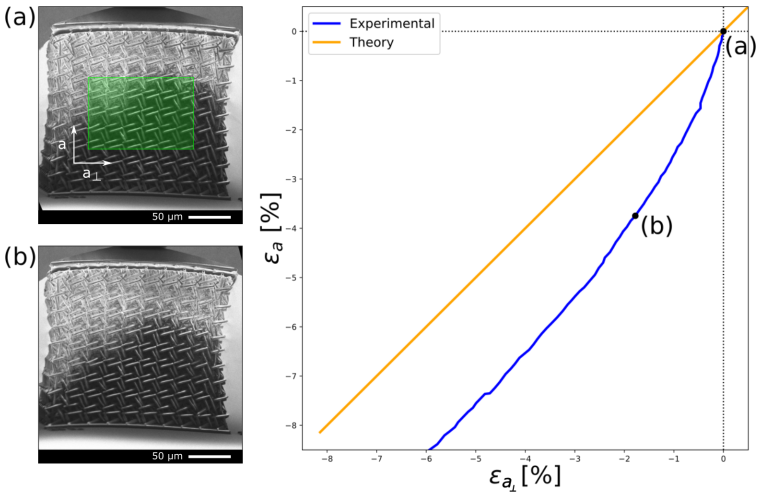
Compression tests were performed on the structures for each of the three distinct viewing directions. For each test, the resulting horizontal and vertical strains were recorded. In the following figures, we report the engineering strains:

$$\epsilon_x = \frac{x - x_0}{x_0}, \tag{6.15}$$

where x is the dimension under study and x_0 is its initial length. Note that we can obtain these strains from the distances a and c from section 6.2.2 by subtracting 1, since these distances have an original size of 1. We discuss each viewing direction separately. We present these strains from both experiment and theory. Next to the plots, we show the state of the structure at the initial position and at the theoretical end of the auxetic interval. These positions are labelled (a) and respectively (b) in the figures.

The results of the first experiment are shown in Fig. 6.8. Here, the structure was compressed along the e_2 direction, with a as the driving parameter and the perpendicular a direction (denoted by $a_{\perp}$) as the orthogonal direction under study. The plot in the figure shows the strains observed in the experiment as well as the strains determined from theory. In the calculated and the experimentally obtained curve, both strains are continuously decreasing throughout the experiment. However, in the experiment, we see that the orthogonal strain lags behind the theoretical value.

Fig. 6.9 shows the results of the experiment where the structure was compressed along the e_2 direction, making a the driving parameter, and c the orthogonal direction under study. In both the theoretical strains and the experimental strains, we see that there is a minimum for ϵ_c, after which this orthogonal strain increases again for continuing compression. In the theoretical curve, this



Figuur 6.8: Strains and images from a compression test along the e_2 direction, measuring the orthogonal strain along $a_{\not\square}$, with vertical dimension a as the driving parameter. (a) shows the undeformed state of the structure. The analyzed region is highlighted in green and the directions a and $a_{\not\square}$ are indicated. (b) shows the deformed state at the end of the calculated auxetic interval.

minimum occurs at $\epsilon_a = -3.7\%, \epsilon_c = -1.35\%$. In the experiment, we saw that this minimum occurred at a larger compressive strain of around -7%.

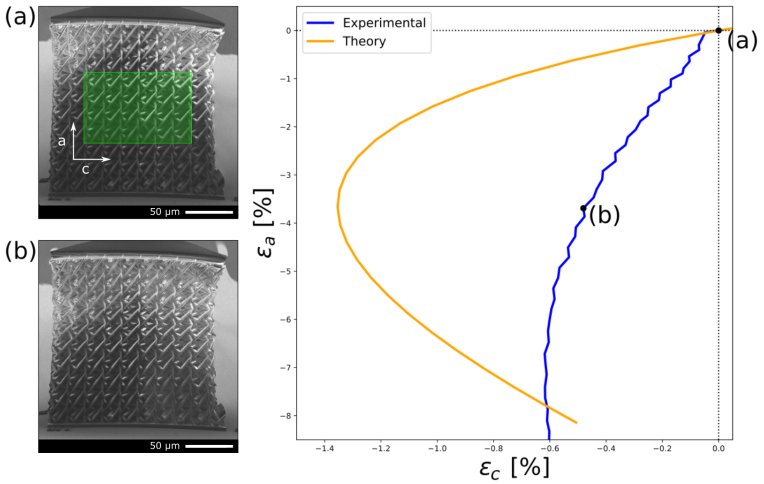
Fig. 6.10 shows the results from the final viewing direction, where the structure was compressed along the e_3 direction, with c as the driving parameter and a as the orthogonal dimension. For this viewing direction, we present applied strains up to $\epsilon_c = -1.35\%$, since compressions beyond that are impossible in theory and might include breaking of the structure in the experimental tests. We see that the theoretical curve flattens off at $\epsilon_c = -1.35\%$, with an orthogonal strain of $\epsilon_a = -3.7\%$. In the experiment, we did not see this lateral contraction. Rather, there was little to no lateral deformation observed.

In the images for all three measurements, we can see that the strains in the structures are not evenly distributed. Especially in the images of Fig. 6.8, we see that the center of the structure contracts substantially more than the regions at the top and bottom of the structure.

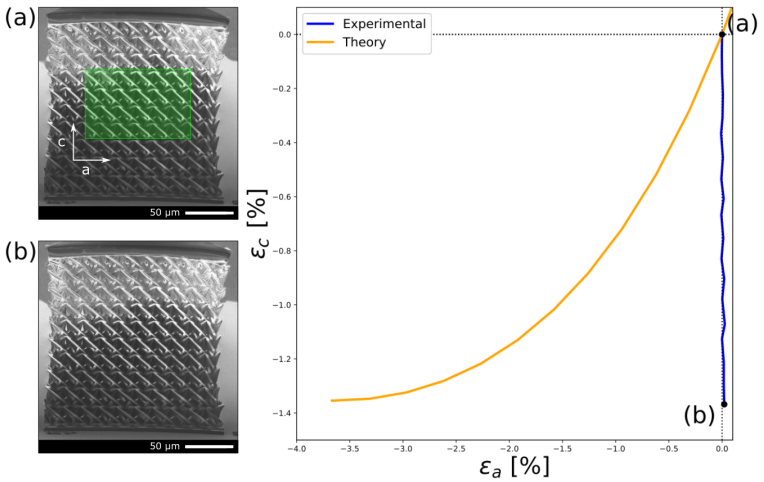
6.5. Discussion

When the structure is compressed along the e_2 direction, with a as the driving parameter, the structure shrinks laterally under increasing compression in both perpendicular directions for the complete calculated auxetic interval. In the measurements, the calculated auxetic interval lies between the points (a) and (b).

Outside of the calculated auxetic interval, we see that the orthogonal a direction keeps shrinking with increasing load, while the c direction starts to expand



Figuur 6.9: Strains and images from a compression test along the e_2 direction, measuring the orthogonal strain along c with a is the driving parameter. (a) shows the undeformed state of the structure. The analyzed region is highlighted in green and the directions a and c are indicated. (b) shows the deformed state at the end of the calculated auxetic interval.



Figuur 6.10: Strains and images from a compression test along the e_3 direction, measuring the orthogonal strain along a with c as driving parameter. (a) shows the undeformed state of the structure. The analyzed region is highlighted in green and the directions a and c are indicated. (b) shows the deformed state at the end of the calculated auxetic interval.

again after an applied strain of -7%. This transition indicates the end of the auxetic interval and occurs later than was calculated from the theoretical model. For both directions, the orthogonal deformations are smaller than those resulting from theory. However, one must take into consideration that the theoretical model assumes unrestricted relative rotations at all joints while monolithic samples have limitations in this respect and introduce boundary conditions. Especially the horzontal constraints introduced by the plates at the top and the bottom of the structure has had a visible effect on the deformation. This can be observed in Fig. 6.8, where the center part of the structure contract substantially more than the sides.

Overall, we observe that the nature of the deformation agrees with the geometric model. Since the structure demonstrated no lateral expansion for each of the three orthogonal views of the structure, we have validated auxetic behavior over the calculated interval admitting compression.

6.6. Conclusion

In this study, we have shown that a framework design based on a geometric theory of periodic auxetics allows for a very explicit and precise description of its global periodic deformation. Furthermore, we have shown that such a framework can be produced using existing additive manufacturing technology at the micrometer scale. Compression tests have been performed on the manufactured frameworks and measurements confirm the auxetic behavior in the interval calculated using the theoretical model.

We emphasize the distinctive role of periodic framework designs with one degree of freedom. In the presence of several degrees of freedom, additional controls or constraints would be needed for selecting an auxetic deformation trajectory from response possibilities which definitely include non-auxetic deformations. Thus, the existence of a general methodology for one degree of freedom auxetic design is particularly relevant [41, 43]. The framework design considered here is of the simplest kind, in view of the fact that it has just two orbits of vertices under periodicity. Moreover, the presence and preservation of the fourfold symmetry allows explicit and precise computations.

Our investigation highlights the importance of predicting and recognizing the interval where auxetic behavior occurs. Within the class of one degree of freedom periodic designs, the *volume increase factor* for the unit cell at the endpoints of the auxetic interval, provides a comparison criterion for auxetic performance.

Bibliografie

[1] C. S. Borcea, F. G. J. Broeren, J. L. Herder, I. Streinu, and V. van der Wijk, *Auxetic interval determination and experimental validation for a three-dimensional periodic framework,* Mathematics and Mechanics of Solids **27**, 764 (2022), https://doi.org/10.1177/10812865211041390 .

[2] A. Love, *A treatise on the mathematical theory of elasticity*, Vol. 1 (Cambridge University Press, 1892).

[3] L. J. Gibson, M. F. Ashby, G. S. Schajer, and C. I. Robertson, *The Mechanics of Two-Dimensional Cellular Materials,* Proceedings of the Royal Society of London Series A **382**, 25 (1982).

[4] A. Kolpakov, *Determination of the average characteristics of elastic frameworks,* Journal of Applied Mathematics and Mechanics **49**, 739 (1985).

[5] R. F. Almgren, *An isotropic three-dimensional structure with poisson's ratio = -1,* Journal of Elasticity **15**, 427 (1985).

[6] R. Lakes, *Foam Structures with a Negative Poisson's Ratio,* Science (80-.). **235**, 1038 (1987).

[7] K. E. Evans, *Auxetic polymers: a new range of materials,* Endeavour **15**, 170 (1991).

[8] O. Sigmund, *Tailoring materials with prescribed elastic properties,* Mechanics of Materials **20**, 351 (1995).

[9] K. E. Evans and A. Alderson, *Auxetic Materials: Functional Materials and Structures from Lateral Thinking!* Adv. Mater. **12**, 617 (2000).

[10] G. N. Greaves, A. L. Greer, R. S. Lakes, and T. Rouxel, *Poisson's ratio and modern materials,* Nat. Mater. **10**, 823 (2011).

[11] Y. Prawoto, *Seeing auxetic materials from the mechanics point of view: A structural review on the negative poisson's ratio,* Computational Materials Science **58**, 140 (2012).

[12] K. K. Saxena, R. Das, and E. P. Calius, *Three decades of auxetics research − materials with negative poisson's ratio: A review,* Advanced Engineering Materials **18**, 1847 (2016).

[13] K. Bertoldi, *Harnessing Instabilities to Design Tunable Architected Cellular Materials,* Annu. Rev. Mater. Res. **47**, 51 (2017).

[14] R. S. Lakes, *Negative-Poisson's-Ratio Materials: Auxetic Solids,* Annu. Rev. Mater. Res. **47**, 63 (2017).

[15] H. A. Kolken and A. A. Zadpoor, *Auxetic mechanical metamaterials,* RSC Adv. **7**, 5111 (2017).

[16] X. Ren, R. Das, P. Tran, T. D. Ngo, and Y. M. Xie, *Auxetic metamaterials and structures: a review,* Smart Mater. Struct. **27**, 023001 (2018).

[17] P. M. Reis, H. M. Jaeger, and M. van Hecke, *Designer Matter: A perspective,* Extrem. Mech. Lett. **5**, 25 (2015).

[18] M. Kadic, G. W. Milton, M. van Hecke, and M. Wegener, *3D metamaterials,* Nat. Rev. Phys. **1**, 198 (2019).

[19] M. J. Mirzaali, H. Pahlavani, and A. A. Zadpoor, *Auxeticity and stiffness of random networks: Lessons for the rational design of 3d printed mechanical metamaterials,* Applied Physics Letters **115**, 021901 (2019).

[20] M. Askari, D. A. Hutchins, P. J. Thomas, L. Astolfi, R. L. Watson, M. Abdi, M. Ricci, S. Laureti, L. Nie, S. Freear, R. Wildman, C. Tuck, M. Clarke, E. Woods, and A. T. Clare, *Additive manufacturing of metamaterials: A review,* Additive Manufacturing **36**, 101562 (2020).

[21] J. Zhang, G. Lu, and Z. You, *Large deformation and energy absorption of additively manufactured auxetic materials and structures: A review,* Composites Part B: Engineering **201**, 108340 (2020).

[22] K. Bertoldi, V. Vitelli, J. Christensen, and M. Van Hecke, *Flexible mechanical metamaterials,* Nat. Rev. Mater. **2** (2017), 10.1038/natrevmats.2017.66.

[23] J. N. Grima and K. E. Evans, *Auxetic behavior from rotating squares,* J. Mater. Sci. Lett. **19**, 1563 (2000).

[24] H. Mitschke, J. Schwerdtfeger, F. Schury, M. Stingl, C. Körner, R. F. Singer, V. Robins, K. Mecke, and G. E. Schröder-Turk, *Finding auxetic frameworks in periodic tessellations,* Advanced Materials **23**, 2669 (2011).

[25] J. C. Á. Elipe and A. D. Lantada, *Comparative study of auxetic geometries by means of computer-aided design and engineering,* Smart Materials and Structures **21**, 105004 (2012).

[26] H. Mitschke, F. Schury, K. Mecke, F. Wein, M. Stingl, and G. E. Schröder-Turk, *Geometry: The leading parameter for the Poisson's ratio of bending-dominated cellular solids,* Int. J. Solids Struct. **100**, 1 (2016).

[27] T.-C. Lim, *Analogies across auxetic models based on deformation mechanism,* physica status solidi (RRL) – Rapid Research Letters **11**, 1600440 (2017).

[28] A. F. Wells, *The geometrical basis of crystal chemistry. Part 1,* Acta Crystallographica **7**, 535 (1954).

[29] W. Gebert, *Three-dimensional nets and polyhedra by a. f. wells,* Acta Crystallographica Section B **34**, 2958 (1978).

[30] O. Delgado-Friedrichs and M. O'Keeffe, *Identification of and symmetry computation for crystal nets,* Acta Crystallographica Section A **59**, 351 (2003).

[31] T. Sunada, *Topological Crystallography*, Surveys and Tutorials in the Applied Mathematical Sciences, Vol. 6 (Springer Japan, 2013).

[32] M. T. Dove, *Theory of displacive phase transitions in minerals,* American Mineralogist **82**, 213 (1997).

[33] C. S. Borcea and I. Streinu, *Periodic frameworks and flexibility,* Proc. R. Soc. a-Mathematical Phys. Eng. Sci. **466**, 2633 (2010).

[34] M. T. Dove and H. Fang, *Negative thermal expansion and associated anomalous physical properties: review of the lattice dynamics theoretical foundation,* Reports on Progress in Physics **79**, 066503 (2016).

[35] A. Yeganeh-Haeri, D. J. Weidner, and J. B. Parise, *Elasticity of α-cristobalite: A silicon dioxide with a negative poisson's ratio,* Science **257**, 650 (1992), https://science.sciencemag.org/content/257/5070/650.full.pdf .

[36] J. N. Grima, R. Jackson, A. Alderson, and K. E. Evans, *Do zeolites have negative poisson's ratios?* Advanced Materials **12**, 1912 (2000).

[37] A. A. Evans, J. L. Silverberg, and C. D. Santangelo, *Lattice mechanics of origami tessellations,* Phys. Rev. E - Stat. Nonlinear, Soft Matter Phys. **92**, 013205 (2015), arXiv:1503.05756 .

[38] J. Dagdelen, J. Montoya, M. de Jong, and K. Persson, *Computational prediction of new auxetic materials,* Nature Communications **8**, 323 (2017).

[39] C. Borcea, I. Streinu, and S.-i. Tanigawa, *Periodic Body-and-Bar Frameworks,* SIAM J. Discret. Math. **29**, 93 (2015).

[40] C. S. Borcea and I. Streinu, *New principles for auxetic periodic design,* SIAM journal on applied algebra and geometry **1**, 442 (2017).

[41] C. S. Borcea and I. Streinu, *Periodic Auxetics: Structure and Design,* The Quarterly Journal of Mechanics and Applied Mathematics **71**, 125 (2017).

[42] C. S. Borcea and I. Streinu, *Auxetic regions in large deformations of periodic frameworks,* in *Interdisciplinary Applications of Kinematics*, edited by A. Kecskeméthy, F. Geu Flores, E. Carrera, and D. A. Elias (Springer International Publishing, Cham, 2019) pp. 197–204.

[43] C. S. Borcea and I. Streinu, *Auxetics Abounding,* in *Proc. 4th IEEE/IFToMM Int. Conf. Reconfigurable Mech. Robot.*, June (Delft, the Netherlands, 2018) pp. 20–22.

[44] Y. Liu, J. H. Campbell, O. Stein, L. Jiang, J. Hund, and Y. Lu, *Deformation behavior of foam laser targets fabricated by two-photon polymerization,* Nanomaterials **8** (2018), 10.3390/nano8070498.

[45] G. Farnebäck, *Two-frame motion estimation based on polynomial expansion,* in *Image Analysis*, edited by J. Bigun and T. Gustavsson (Springer Berlin Heidelberg, Berlin, Heidelberg, 2003) pp. 363–370.

[46] G. Bradski, *The OpenCV Library,* Dr. Dobb's Journal of Software Tools (2000).

7

An Origami-Inspired Spherical Transformable Metamaterial Based on Symmetry Groups

Ivar R. Nuijts, Freek G.J. Broeren, Volkert van der Wijk, Just L. Herder

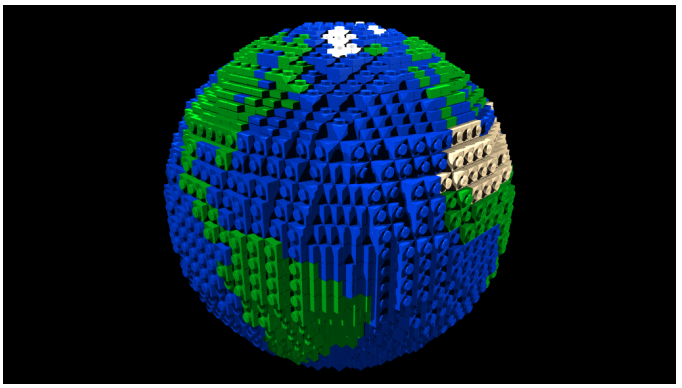
Most currently existing mechanical metamaterial designs are based on Bravais lattices. These consist of paralellogram or parallellepiped unit cells, which are respectively translated along two or three independent vectors to fill the complete space. This approach is inherently unable to match curved surfaces like spheres, since these cannot be constructed only from parallel and perpendicular lines. In this paper, we introduce a generalized unit cell, based on the symmetry groups of the sphere. We use this approach to develop a spherical transformable origami-inspired metamaterial. We describe the motions of this new metamaterial, as well as experimental observations on a physical, 3D printed model.

The contents of this chapter have been published in the proceedings of the 7th International Conference on Control, Mechatronics and Automation (ICCMA)[1]

7.1. Introduction

Mechanical metamaterials are an emerging class of materials where an internal structure, rather than the chemical structure of the material they are made of, dominates the bulk material properties [2, 3]. Generally, when designing these mechanical structures, a unit cell (UC) is designed, of which many copies are repeatedly placed along two or three lattice vectors, for planar and spatial metamaterials respectively, to fill all of space according to a Bravais lattice[4]. This approach greatly simplifies the design process, since it is assumed that the internal deformations of the material structure follow the same periodicity. In general, the mechanical behavior of the metamaterial is fully determined by the behavior of the single unig cell. Therefore, the mechanical behavior that is designed in a single unit cell determines the mechanical properties of the bulk.

While this approach lends itself well to create infinite areas or volumes, not all finite shapes can be created in this way. Specifically, when we consider curved surfaces, we are able to approximate their shape by a stacking of parallellepipeds, but will, in general, never be able to exactly match all curvatures. To illustrate this, consider building a sphere of LEGO bricks. With increasing numbers of available bricks, the sphere can be better approximated, but an exact matching will never be achieved, as illustrated in Fig. 7.1



Figuur 7.1: When creating a sphere out of LEGO bricks (or other parallellepipeds), only an approximation of the sphere can be achieved. *Source: LEGO Ideas - LEGO Globe (Lowell sphere method)* https://ideas.lego.com/projects/d287ef4e-cd1c-491d-8491-dca7de3204c5

In this paper, we present a generalized way of constructing a unit cell, based on the symmetry groups of the desired shape, which is a sphere in our case. Using this method, the unit cell is not copied and translated along generators of a Bravais lattice, but the copies of the unit cell are rotated and mirrored according the chosen symmetry groups of the sphere. Because of this it will be shown that the whole sphere can be exactly matched by the designed mechanical structure.

We employ this method to design a transformable origami-inspired sphere, consisting of 60 generalized unit cells. These unit cells have a single degree

of freedom, allowing the sphere to change in size, enabling a reduction of the inscribed volume of 76.3%.

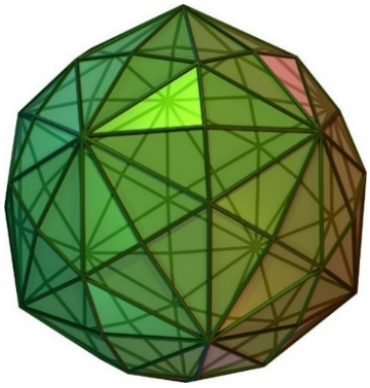
We present a kinematic analysis of this mechanical structure as well as experimental validation of a 3D-printed prototype. We discuss the performance of the design as well as the number of degrees of freedom when periodicity is relaxed to the whole sphere.

7.2. Spherical Symmetry Groups

For spheres, there are exactly 14 possible symmetry groups [5, 6]. These groups can be further split into two categories: platonic and parametric symmetries. Seven platonic symmetry groups exist, corresponding to the Platonic solids. There are seven parametric groups, for which the number of fundamental domains that are needed to span the whole sphere depends on a parameter.

In this study, we chose to focus on the Platonic groups, since for these groups the fundamental domains are more evenly distributed over the sphere due to their correspondence to regular polyhedra. For the parametric groups, there are two sets of fundamental domains, one on the “north-side” of the sphere, and one on the “south-side”, leading to a less evenly distributed set of domains. Since, as we describe in the next section, a polyhedral approximation of the sphere will be used in our design, the even distribution of the fundamental domains leads to a better correspondence between the mechanism and the orinial sphere.

Within the Platonic groups, the *532 symmetry group (using the notation from [5]) was chosen, as it leads to the largest number of fundamental domains on the sphere. This group corresponds to the dodecahedron and its dual, the icosahedron. The fundamental domains of this symmetry group correspond to the faces of a Dysdiakis Triacontahedron7.2. This polygon has 120 faces and is the largest Catalan solid.

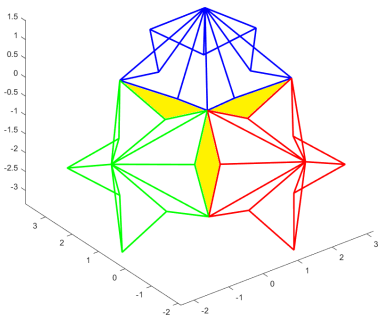


Figuur 7.2: The fundamental domains of the spherical *532 symmetry group correspond to the faces of a Dysdiakis Triacontahedron. *Source: Wikimedia Commons*.

7.3. Unit Cell Design

We design the origami-inspired spherical mechanism based on a unit cell consisting of rigid faces and folds. In general, the folding of curved surfaces is not possible without tearing or buckling. Therefore, to create a folding mechanism, we need to approximate the sphere with a polyhedron. The choice for *532 symmetry in the previous section leads to the Dysdiakis Triacontahedron.

For our origami-inspired mechanism, we take all these faces to be rigid and design the connections between the faces such that a dilational motion is obtained. For this, we consider a Unit Cell consisting of two faces, connected by a fold. Five of these unit cells can be coupled, again with folds, to form a pentagonal unit. The connections between the pentagonal units are realized by spherical joints at the corners of the base pentagon. This structure, for three of such pentagonal units, is shown in Fig. 7.3.



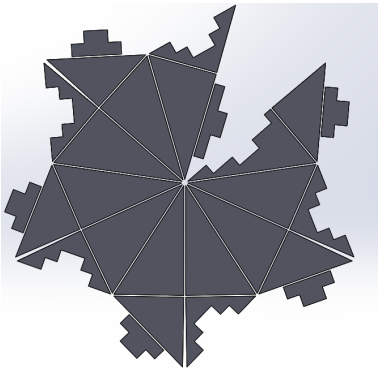
Figuur 7.3: The origami-inspired structure consists of rigid triangular faces, which are connected by folds into pentagonal units (shown with red, blue and green outlines). These units are subsequently coupled by spherical joints, allowing for open spaces (shown in yellow) when the structure is deformed.

When the unit cells are repaeated all over the sphere in this way,

Twelve of these pentagonal units can be used to span the sphere, preserving the single degree of freecom of the unit cell. At the construction position, without open spaces between the pentagonal units, it is a dysdiakis triacontahedron, and when actuated, the sides of the pentagonal units move inwards, shrinking the side-lengths of the regular pentagon they describe. This creates open spaces between these pentagonal units, leaving only point contacts between them. In the physical model, these connections are realized by adding two plates to the unit cell, which are folded into the polyhedron in the construction position. In this way, the whole mechanism consists of rigid plates, connected only by fold lines.

7.4. Fabrication Methods

Of the model shown in Fig. 7.3 a prototype was designed and 3D printed in parts from PLA, using a Prusa i3mk2 3D printer. The 12 printed parts were aligned using notched connectors at their sides and cyanoacrilate glue was used to fix these connections. The design of one such part is shown in Fig. 7.4



Figuur 7.4: A top view of the pentagonal unit design. These structures were 3D printed in the shown flat state. Netting was used to create fold lines between the grey rigid plates and twelve of these units were assembled into a Dysdiakis Triacontahedron by matching and gluing the notched parts.

The parts were 3D printed in a flat state. Each part consisted of a single pentagonal pyramid, opened up at one of the fold lines to fold it flat. The total thickness of the plates is 3mm. For the fold lines, two layers of netting were included within the 3D print, one at a height of 0.5mm and one at a height of 2.75mm. These layers were included during printing and the following layers of PLA flows between the netting, securing it within the rigid plats. After 3D printing, the top- and bottom layers of netting were cut selectively to assign mountain- and valley folds to the mechanism. This resulted in an origami mechanism consisting of rigid plates, connected by fold lines with very little stiffness.

7.5. Results

7.5.1. Degrees of Freedom

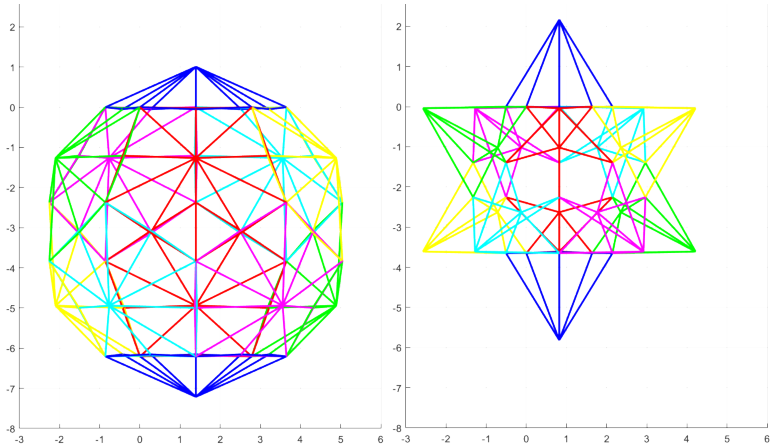
The generalized unit cell we designed has a single degree of freedom. However, when the whole sphere is considered, instead of just the periodic motions based on a single unit cell, There are 33 degrees of freedom. This number was calculated using counting-arguments, and verified by modeling the whole structure as a pin-jointed framework and calculating the nullspace of the Jacobian[7].

In the physical model, these extra degrees of freedom made it difficult to uniquely control the mechanical structure. A balloon was inserted into the enclosed volume such that by inflating the balloon, the prototype expands symmetrically, as if it has a single degree of freedom. To investigate the practical volume decrease, the balloon was deflated and the structure was collapsed ma-

nually.

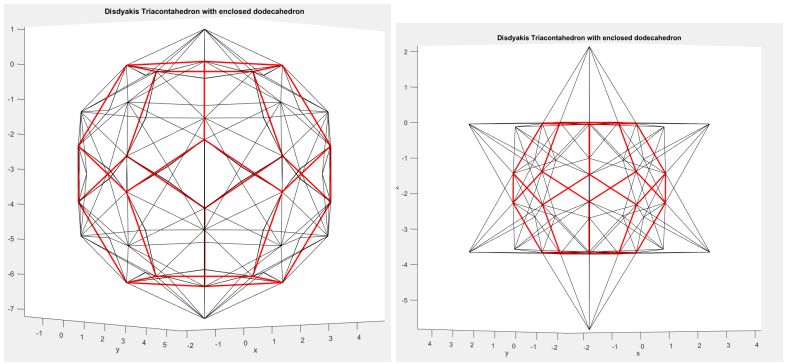
7.5.2. Volume Change

When the mechanism is contracted, the pentagonal units deform such that their base pentagon remains regular and the side-lengths decrease. Simultaneously, the pentagonal units become more pointed, creating a shape similar to a stellated dodecahedron. This state is shown, next to the fully expanded state, in Fig. 7.5.



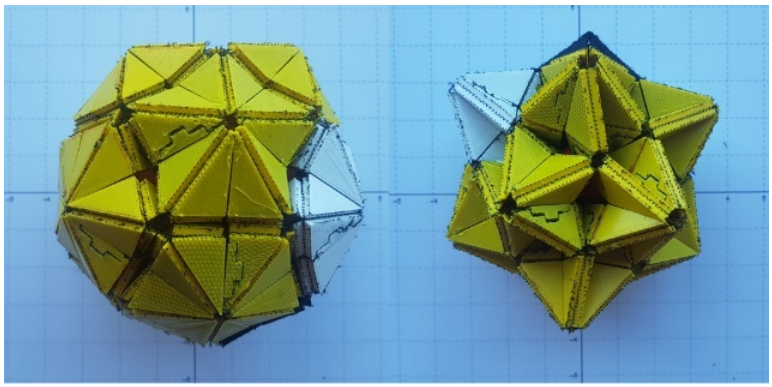
Figuur 7.5: The expanded (left) and contracted (right) state of the origami-inspired mechanism.

To determine the volume decrease of the kinematic model under actuation, the inscribed dodecahedron, defined by the connection points of the pentagonal units was used. This is illustrated in Fig. 7.6. This volume was calculated in the kinematic model to undergo a decrease of 76.3%.

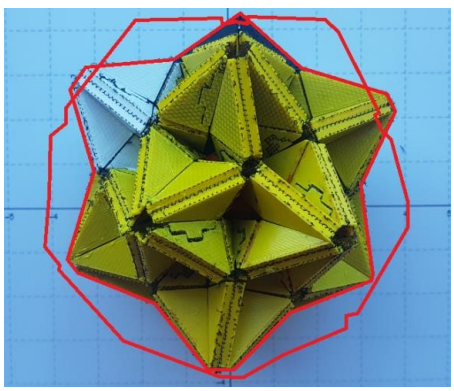


Figuur 7.6: The volume change of the mechanism is determined based on the inscribed dodecahedron, defined by the connection points of the pentagonal units. This dodecahedron is shown here in red.

Images of the physical model in both the expanded and contracted state are shown in Fig. 7.7. In this case, the volume decrease achieved was less than the calculated value. This is clearly shown in Fig. 7.8, where the two states are superimposed in one figure. The enveloping sphere of the model hardly changes in size.



Figuur 7.7: The physical model in the expanded state (left) and in the contracted state (right).



Figuur 7.8: Comparison of the expanded and contracted state of the physical model. The contracted state is shown, with the contours of both the contracted and the expanded state drawn in red.

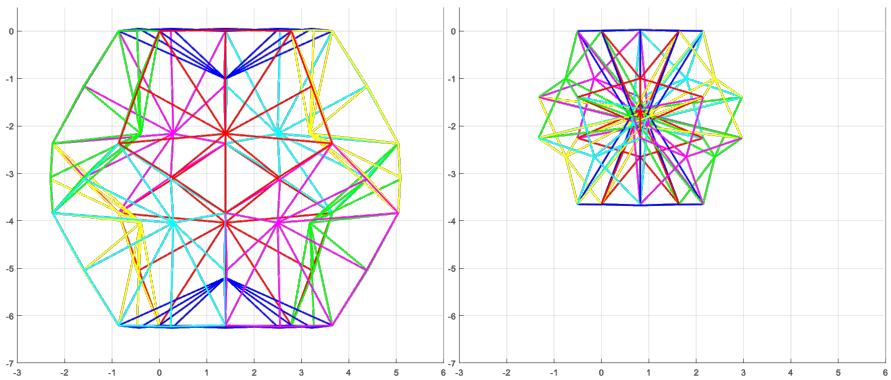
7.6. Discussion

While the volume decrease of the kinematic model is not matched by the physical model, the deformed shapes match. The differences between the two are likely caused by the thickness of the plates in the physical model. This was assumed to be zero in the kinematic model, while they physically limit the motion of the prototype. Also, because the physical model had 33 degrees of freedom and was actuated by hand, it is likely that the extremal states of the mechanism

were not reached. For example, the expanded state shown in Fig. 7.7 shows small indentations on the edges of the pentagonal units, indicating that the fully expanded state was not reached.

A balloon was used to expand the structure, but the contraction was done done manually in this study. As an improvement, the balloon could be attached to the inside of the mechanism, also allowing control of the mechanism contraction through deflation of the balloon. Alternatively, a different assignment of fold lines might help to reduce the degrees of freedom.

Finally, the mechanism presented in this paper deforms from a Dysdiakis Triacontahedron into a stellated dodecahedron. If the largest diameter of the structure is considered, the resulting scaling is minimal. An alternative design could have the pentagonal units pointed into the enclosed volume, creating an approximate dodecahedron with dimples in the faces, as illustrated in Fig. 7.9. This design would have a greater volume change of the circumscribed dodecahedron, but the internal collisons would not allow the neigboring faces to fold completely flat.



Figuur 7.9: An alternative design, where the pentagonal units are inverted to point into the enclosed volume, for improved scaling of the circumscribed volume. Shown are both the expanded (left) and the contracted state (right).

7.7. Conclusions

In this paper, we have presented an origami-inspired transformable mechanism whose construction was based on the spherical *532 symmetry group. The sphere is designed to perform a dilational motion, which results in a decrease of the inscribed dodecahedron volume of 76.3%.

In order to construct this spherical structure, we developed a generalization of the periodic lattices regularly used for the design of mechanical metamaterials. The generalized unit cell consists of a fundamental domain of the chosen spherical symmetry group, and instead of building the lattice by discrete translation, the corresponding symmetry operations are used. The resulting design was constructed using additive manufacturing, with netting used to obtain low

stiffness fold lines between the rigid plates.

Bibliografie

[1] I. R. Nuijts, F. G. J. Broeren, V. van der Wijk, and J. L. Herder, *An origami-inspired spherical transformable metamaterial based on symmetry groups,* in *2019 7th International Conference on Control, Mechatronics and Automation (ICCMA)* (2019) pp. 295–298.

[2] A. A. Zadpoor, *Mechanical meta-materials,* Mater. Horizons **3**, 371 (2016).

[3] M. Kadic, G. W. Milton, M. van Hecke, and M. Wegener, *3D metamaterials,* Nat. Rev. Phys. **1**, 198 (2019).

[4] A. Bravais, *Mémoire sur les systèmes formés par les points distribués régulièrement sur un plan ou dans l'espace,* J. Ec. Polytech. **19**, 1 (1850).

[5] J. H. J. H. Conway, H. Burgiel, and C. Goodman-Strauss, *The symmetries of things* (A.K. Peters, Wellesley, Mass. :, 2008) p. 426.

[6] J. V. D. Craats, *Symmetric Spherical and Planar Patterns,* (2011).

[7] R. Hutchinson and N. Fleck, *The structural performance of the periodic truss,* J. Mech. Phys. Solids **54**, 756 (2006).

8

A General Method for the Creation of Dilational Surfaces

Freek G.J. Broeren, Werner W.P.J. van de Sande, Volkert van der Wijk, Just L. Herder

Dilational structures can change in size without changing their shape. Current dilational designs are only suitable for specific shapes or curvatures and often require parts of the structure to move perpendicular to the dilational surface, thereby occupying part of the enclosed volume. Here, we present a general method for creating dilational structures from arbitrary surfaces (2-manifolds with or without boundary), where all motions are tangent to the described surface. The method consists of triangulating the target curved surface and replacing each of the triangular faces by pantograph mechanisms according to a tiling algorithm that avoids collisions between neighboring pantographs. Following this algorithm, any surface can be made to mechanically dilate and could, theoretically, scale from the fully expanded configuration down to a single point. We illustrate the method with three examples of increasing complexity and varying Gaussian curvature.

The contents of this chapter have been published in Nature Communications (2019) [1]

8.1. Introduction

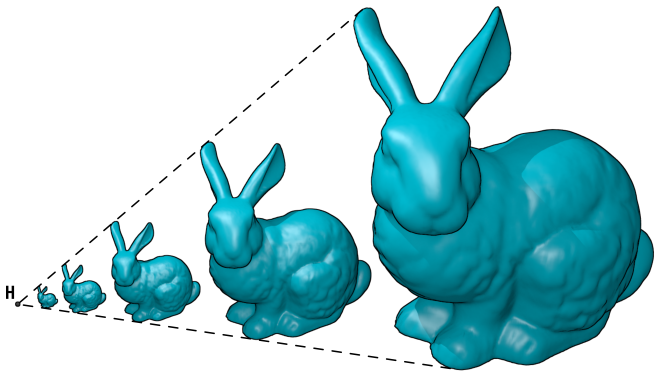
Expandable structures are of significant relevance in nature and engineering and come in a variety of forms. Natural examples include the stowing of the precious wings of beetles [2] or the fitting of young leaves into buds [3]. Numerous engineering examples can be found as well, including satellite antennas and solar panels that need to be compact for launch and expand for operation [4–7], and medical stents that need to be moved through arteries [8] or the esophagus [9] in compacted form and deploy at the target position.

Most expandable structures rely on an underlying mechanism to allow them to be reversibly compacted. One well-known example of an expandable structure in which the mechanism is clearly visible is the Hoberman Sphere [10, 11]. This mechanism dilates, i.e. its envelope changes in size without changing its shape [12, 13]. We define dilational structures as structures composed of mechanisms whose only degree of freedom corresponds to dilation. Other examples of dilational structures are dilational polyhedral linkages [14, 15].

Dilational structures have also been studied in the field of mechanical metamaterials [16, 17], particularly for auxetic behavior where the Poisson's ratio is negative [18–20]. A Poisson's ratio of exactly -1 corresponds to dilation.

Currently, several limitations in dilational structures exist. Firstly, most dilational structures have been designed for a specific shape or curvature, making these mechanisms applicable to a very limited set of shapes; for example, the buckliball [21], which is based on a polyhedral linkage that resembles a sphere. Secondly, linkages such as the Hoberman Sphere use mechanisms that move perpendicular to the described surface, making them protrude into the enclosed volume, which, for instance, could be a problem in stent design. Thirdly, to the authors knowledge, no examples of spatial mechanical metamaterials exist that can be sculpted to thin, curved surfaces. The unit cell that governs the behavior of such structures inherently has a finite volume, making the construction of thin dilational surfaces with only motion tangent to the plane impossible. Also, the current planar auxetic metamaterials can not, in general, be used, since the underlying kinematics are not valid for arbitrarily curved surfaces.

In this paper, we present a general method to create mechanism-based dilational structures fitting to any spatially curved surface, by which we mean 2-manifolds with or without boundary. Our method improves on existing work on two key points. Firstly, the resulting mechanism structure is placed on the surface, with no parts of the mechanism moving into the enclosed volume and normal to the surface, unlike for instance the Hoberman mechanism. Secondly, the method is applicable to surfaces with any curvature and can even be applied to non-closed surfaces, i.e. surfaces containing holes or cuts. Enabling these properties in dilational structures makes them of use in, for instance, structures that grow with a person such as medical braces for children and expandable furniture, medical devices that require stowability or compression but need to be stiff otherwise, or implants that need to accommodate some motion but maintain their shape, such as aortic stents.



Figuur 8.1: Under dilation, a structure scales with respect to a homothetic center (point H in this figure), preserving its size and orientation.

In the following, we describe the method, where we first triangulate the surface and then place pantograph mechanisms on each of the faces of the triangulation. We prove that this method can be used for any spatially curved surface and comment on the maximum scaling factor possible for these structures. Finally, we apply our method to three surfaces of increasing complexity, illustrating its versatility.

8.2. Results

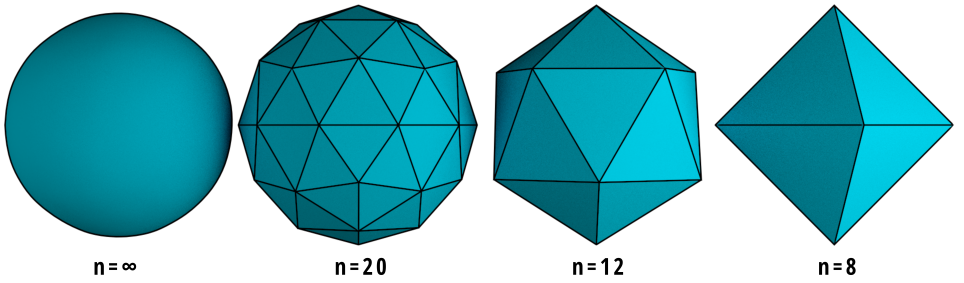
8.2.1. Dilation

Dilation is a homothetic transformation that relates two similar shapes with respect to a homothetic center [22]. Any two figures related by a dilation are similar and have the same orientation (see Fig. 8.1). This transformation preserves the shape and orientation of the figure, but changes the size of each of the elements of the structure by the same factor. In a dilational structure the distances between a representative set of points on the structure, typically corner joints, all scale by the same factor during actuation.

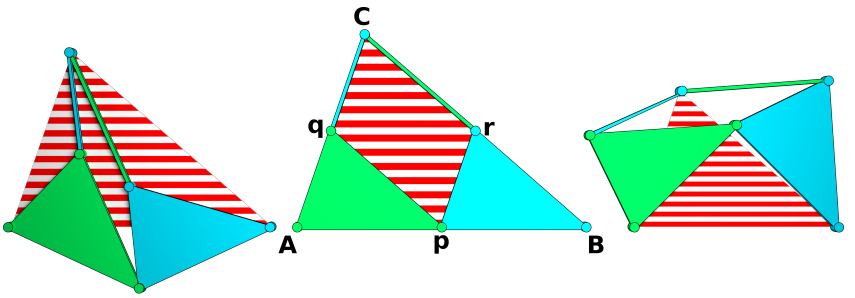
8.2.2. Triangulation

The first step of the presented design method is to triangulate the curved surface from which we want to create a dilational structure. Triangulation is a common strategy to approximate curved surfaces by a mesh of triangular faces and lies at the basis of the STL file format used in 3D printing [23, 24]. Triangulation is illustrated in Fig. 8.2 for a sphere. It is observed that the accuracy of the approximation increases with the number of triangular faces in the resulting mesh.

The triangulation results in a polyhedral surface with only triangular faces. It can be shown that every surface (by which we mean a 2-manifold with or without boundary) can be triangulated such that at most two triangular faces share



Figuur 8.2: Any curved surface, in this case a sphere, can be approximated by a mesh of triangles in a process called triangulation. A larger mesh of triangular faces gives a better approximation of the original surface. Shown are polyhedral triangulations of a sphere with n triangular faces.



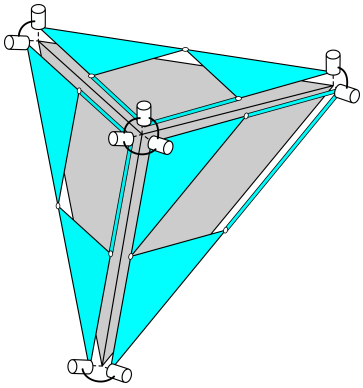
Figuur 8.3: The skew pantograph is a one-degree-of-freedom mechanism that scales the spanned triangle (i.e. the red-striped area) determined by three of its joints; the similarity points, indicated A, B and C. This mechanism has revolute joints at points $p, q, C, andr$. For the neutral position, shown in the middle, the spanned triangle equals the triangular shape of the pantograph, this is a useful pose for constructing dilational surfaces.

an edge. [25] If the resulting polyhedron undergoes dilation, the number of triangles, their shapes and their respective relations must stay constant. Only the size of the triangles is allowed to change, their aspect ratio and orientation are preserved.

8.2.3. Pantograph linkage

To transform the polyhedral surface into a movable linkage with dilational motion, we employ the skew, or Sylvester's, pantograph mechanism [26–28].

The skew pantograph is a four-bar mechanism of which two adjacent links are extended into triangles. The mechanism has revolute joints at p, q, C and r, as illustrated in Fig. 8.3. The link Cq is equal in length to side rp, as are Cr and qp, which makes $pqCr$ a parallelogram. Also, the triangles Apq and pBr are similar. A resulting feature from these properties is that in any pose of the mechanism the triangle ABC is similar to triangles Apq and pBr. The proof can be found in Hall (1986) [29]. When the mechanism moves, the distances AC, AB and BC become smaller as the parallelogram decreases in area. As a result, the



Figuur 8.4: The relative orientation of adjacent pantograph mechanisms is maintained by compound universal joints. This figure shows part of a dilational surface, the triangular faces are shown in grey, and the rigid parts of the pantograph mechanisms are shown in blue. At each of the corners of the pantographs, they are coupled to their neighbors by universal joints. A universal joint consists of two revolute joints (shown as white cylinders) in series. A compound universal joint is created at an intersection with three (or more) triangular faces.

mechanism has a single degree of freedom and during motion the striped red triangle described by its three similarity points (indicated A, B and C) changes in size but remains similar of shape, as is illustrated for three poses. These three joints will be referred to as the similarity points of the pantograph linkage.

The maximum scaling that can be achieved with a skew pantograph depends on the placement of the joints on the edges of the spanned triangle in the neutral position. We place the joint in the middle of the sides of the spanned triangle in the neutral position, such that $Aq = qC$. In this way, the rigid triangles are sized down by a factor 2 relative to the spanned triangle, which allows the spanned triangle to scale down to a single point.

8.2.4. Coupling the pantographs

Each of the faces obtained by triangulating the curved surface is replaced by a skew pantograph mechanism. In this way, we ensure that each individual face can only deform by scaling, keeping its original shape.

The pantograph mechanisms ensures the proper scaling of each individual face. However, in order for the whole structure to dilate, it is also required that each face simultaneously scales by the same factor and that the faces do not rotate with respect to each other. We achieve this by connecting neighboring pantograph mechanisms by means of compound universal joints, whose description follows.

Two adjacent faces of the triangulated surface share a single edge and two vertices. In order to maintain the mobility of the neighboring pantograph mechanisms, they can only be connected at the vertices. At these points, we connect the pantograph mechanisms with universal joints (two consecutive revolute pairs), of which the axes are parallel to the normals of the respective faces,

as is illustrated in Fig. 8.4. This configuration constrains the rotation about the shared edge of the faces and therefore preserves the relative orientation of the two faces.

Because the two neighboring pantograph mechanisms are now connected along the shared edge, their degrees of freedom are also coupled. When one of the pantograph mechanisms moves, the length of the shared edge will change, causing a movement in the other pantograph. In this way, it is ensured that both pantographs are scaled simultaneously by the same factor and maintain their relative orientation.

Each set of neighboring pantograph mechanisms is connected in this way, creating compound universal joints at the corners of the faces. This preserves the relative angles of all faces and ensures the same scale factor for each of the faces. Therefore, the total resulting motion will be dilation.

8.2.5. Range of Motion of the pantograph

Kinematically, a structure constructed from the proposed pantograph mechanisms can scale down to a point. In reality, the range of motion of the planar pantographs is limited because of collisions among the rigid bodies that make up the pantographs. In this section, we highlight the factors limiting the range of motion of the dilational mechanisms constructed from pantographs and discuss how to minimize their effects.

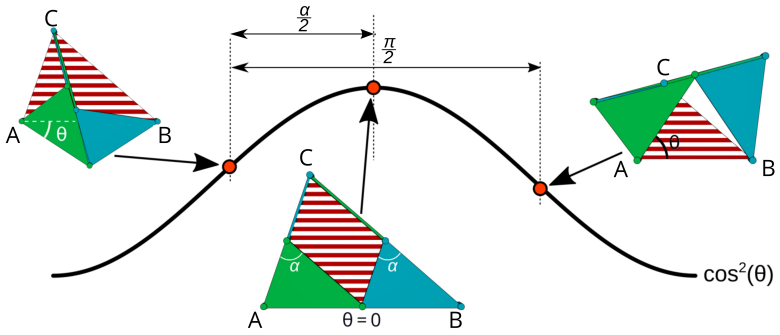
We have described the pantograph mechanism used to make the triangular faces of the polygons dilational. The motion of the mechanism can be described by a single parameter θ and the sides of the spanned triangle are scaled by a factor $\lambda = \cos(\theta)$ when the mechanism is actuated [30]. The area of the spanned triangle is then scaled by a factor of $\lambda^2 = \cos^2(\theta)$, see Fig. 8.5.

Starting at the neutral position, where $\theta = 0$, the mechanism can move in two directions: θ can increase or decrease, corresponding to a counter-clockwise or clockwise rotation of the lower left rigid triangle. In both cases, the effect on the scaling of the spanned triangle will be the same, since $\cos(\theta)$ is symmetric around $\theta = 0$.

In the case where θ increases, the mechanism will protrude out of the spanned triangle at two edges, while it will open up free space at the third edge. Conversely, when θ decreases, the mechanism protrudes out of the spanned triangle at one edge, and opens up space at the other two edges.

When the rigid bodies of the pantograph mechanism are allowed to overlap and cross each other, the minimum area of the spanned triangle is obtained at $\theta = \pm\frac{\pi}{2}$ for the two different cases, both resulting in a scaling factor $\lambda = 0$. When collisions are considered, these values of θ can no longer be reached and often, the scaling factor λ differs between the two motion directions.

If the pantographs are designed to be planar and therefore move within a single plane, the range of motion is limited by internal collisions of the links. All pantograph mechanisms in the dilational surface are linked to have a single degree of freedom. Therefore, when one pantograph is actuated such that, for that mechanism, we obtain a rotation θ in its triangular faces, all other pan-



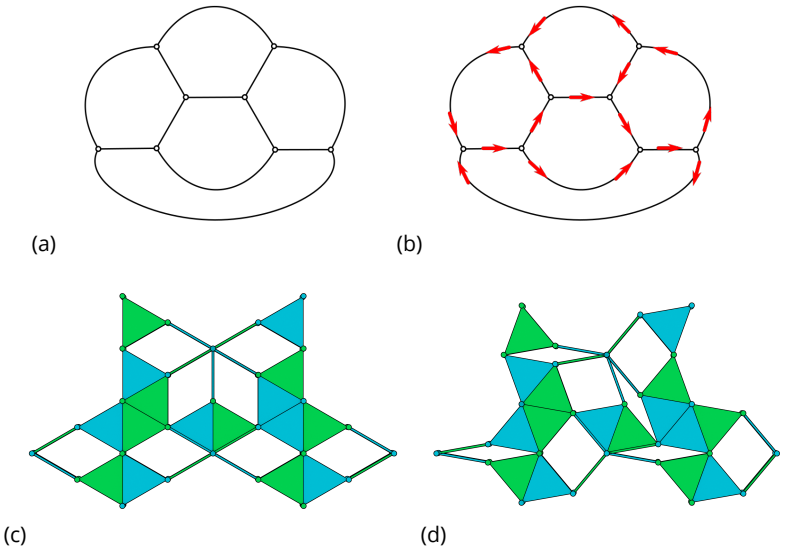
Figuur 8.5: The limits of scaling of a skew pantograph. The area of the spanned triangle (shown as a red-striped area) scales with $\cos^2(\theta)$. The red dots illustrate the values of θ in each of the drawings. The end of motion is reached when the bars of the linkage become collinear (left and right drawings). Between these states, the rotation angle of θ is always $\frac{\pi}{2}$. The distribution of this range over the left and right motion directions depends on the top angle α.

tograph mechanisms in the dilational surface will have a rotation of $\pm\theta$. This causes the complete mechanism to reach the end of its motion as soon as self-collision occurs in any pantograph of the structure. Therefore, this is the main limiting factor on the maximum scaling factor of the assembled dilational mechanism.

Looking at Fig. 8.5, we can see that the pantograph mechanism reaches the end of its range of motion when $\theta = -\frac{\alpha}{2}$ for one direction of motion, or when $\theta = \frac{\pi-\alpha}{2}$ for the other direction, where α is the top angle of the spanned triangle. At these points, the binary links of the pantograph mechanism become collinear. In this calculation, we have considered the links as lines of zero width. In reality, the links and joints from which the pantograph mechanisms are constructed will have finite width. This will cause collisions to happen earlier and limits the range of motion further.

The total range of θ is $\frac{\pi}{2}$ radians, because the internal angles between the links at two adjacent corners of a parallelogram four-bar linkage always add up to π. For the case where the links have zero width, the optimal scaling factor would be found when $\alpha = 0$ or when $\alpha = \pi$, allowing only for motion in one direction.

However, in both of these cases, the pantograph degenerates to a line, in which case no feasible mechanism would be possible. For simplicity and ease of tiling, it is beneficial when both motions directions have the same range from the neutral position. This is the case for $\alpha = \frac{\pi}{2}$; i.e. when the pantograph mechanisms are right-angled. In this case, the maximal scaling factor is $\lambda = \cos\left(\frac{\pi}{4}\right) = \frac{\sqrt{2}}{2} \approx 0.71$. So, when self-collisions are considered, the distances between points on the dilational surface can be scaled down by at most 29%



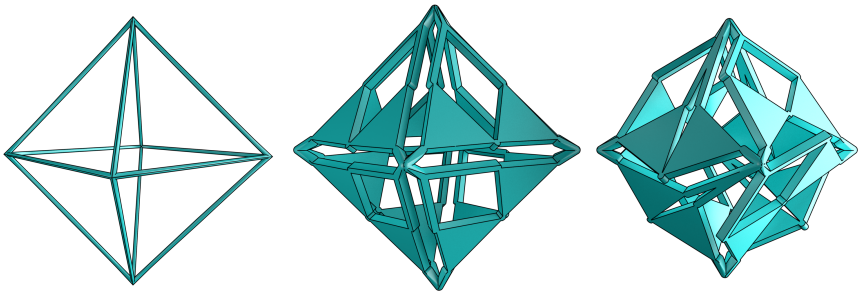
Figuur 8.6: Steps in obtaining a correct tiling pattern of pantographs: (a) dual graph of the net, where the vertices are the faces of the triangulated surface, (b) directed dual graph with correct orientation, (c) correct tiling pattern, (d) correct tiling pattern with $\theta = 20°$

relative to the neutral position.

8.2.6. Placement of the pantographs

When the pantograph mechanism moves, some parts of the mechanism protrude out of the spanned triangle, while other parts move into the spanned triangle. When all the faces of a triangulated surface are replaced by pantograph mechanisms, two neighboring pantographs could have parts moving out of the respective spanned triangles at their shared edge. This will cause neighboring pantographs to collide, locking the motion of the structure and thereby no longer allowing the scaling of the structure. To remedy this, we have created an algorithm that places the pantographs on a triangulated surface such that neighboring pantographs move along with each other, i.e. when one side of a pantograph has parts that move out of the spanned triangle, the corresponding side of the neighboring pantographs will have parts moving inwards. The algorithm consists of the following procedure.

We first construct the dual graph to the triangulated surface. In this graph, there is one node for each triangular face and two nodes are connected if the two corresponding faces share an edge. Such a graph is shown in Fig. 8.6a for the octahedron. Note that, as was mentioned in Section 8.2.2, at most two faces share an edge since the original surface is a 2-manifold. The dual graph to an octahedron is shown in Fig 8.6a. For closed surfaces, this creates a simple, connected, 3-regular graph. We assign a direction to each of the edges in the



(a) (b) (c)

Figuur 8.7: Eight pantograph linkages are placed on the octahedron. (a) shows the wireframe of an octahedron. (b) shows the dilational structure in the neutral position, ($\theta = 0$) and (c) shows a compacted position ($\theta = 25°$).

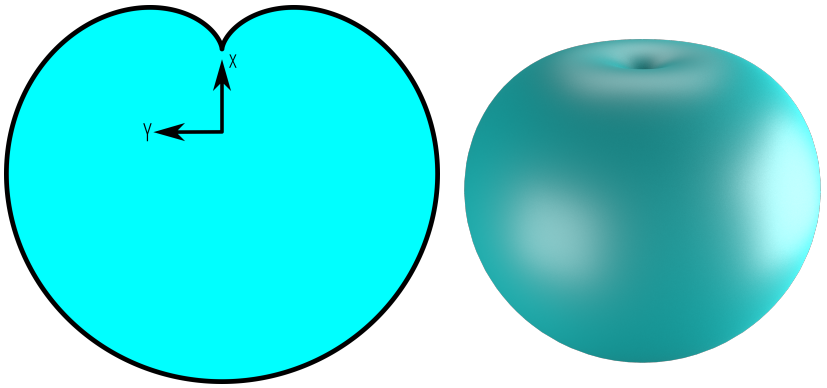
graph to represent the motions of the pantograph mechanisms placed on the triangulated surface. A directed dual graph for an octahedron is shown in Fig. 8.6b. Since each edge in the dual graph can only have a single direction, the sides of the triangles are enforced to move along with each other.

The movement of the pantograph mechanisms is such that either the links on two sides move out of the spanned triangle and the links on the other into it or vice-versa, as shown in Fig. 8.3. Therefore, we require for each vertex of the graph that its indegree and outdegree are larger than zero. In Supplementary Note 1, we show that for each simple connected graph where every node has a degree of at least 2, it is always possible to find an orientation of the graph such that both the indegree and outdegree of every node are larger than zero. The dual graph to every feasible triangulated surface always has nodes of degree at least 3; nodes with degree larger than three correspond to holes in the surface. Therefore, there must exist an orientation of the pantographs on each surface such that movement without collisions between the pantograph mechanisms is possible.

To find a suitable orientation, we use an algorithm that searches for flows through the representing graphs. A flow through a vertex ensures that the difference between the indegree and outdegree is one. This algorithm is further discussed in Supplementary Note 2. Once this orientation is found, the pantographs can be placed accordingly, see Figs. 8.6c,c for an example.

8.2.7. Examples

In this section, we will show the application of our method to three surfaces: an octahedron as a simple example [30], a cardioid with both positive and negative Gaussian curvature, and the Stanford Bunny as an advanced example. For all three examples, the reported maximum scaling is based on the pantographs in the resulting structure with the largest and smallest top angle, as described in subsection 8.2.5.



(a) (b)

Figuur 8.8: The cardioid surface is constructed by revolving the planar cardioid curve. (a) shows the curve, (b) shows the complete revolved cardioid.

We start with the octahedron. This polygonal surface can be viewed as a very rough triangulation of a sphere, comprised of only 8 triangular faces. The eight faces of the octahedron are replaced by pantograph mechanisms, see Fig. 8.7 and Supplementary Movie 1. In this way, a dilational surface with only equilateral faces is obtained ($\alpha = 60°$);this gives them a range of $[-30°, 60°]$. Any placement of the pantograph linkages will include pantographs with opposite motion directions, the maximum scaling can therefore be calculated to be $\lambda = \cos(30°) = 0.866$.

As a second example. we look at the cardioid. The cardioid is a planar curve obtained by tracing a point on a circle, which is rolled around a second circle with equal radius. This curve can be parameterized as follows:

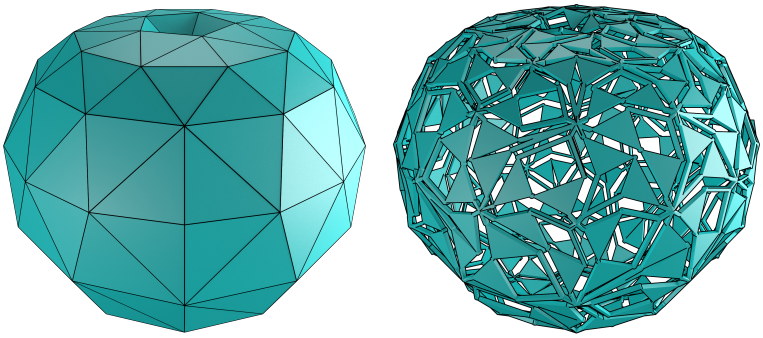
$$x(t) = a(2\cos(t) - \cos(2t)) \tag{8.1}$$
$$y(t) = a(2\sin(t) - \sin(2t)). \tag{8.2}$$

By revolving this curve around the x-axis, we obtain a spatial surface, as is shown in Fig. 8.8.

We have triangulated this shape by taking a planar map of the surface and performing a Delaunay triangulation [31, 32] on this map. The points of the triangulation have been chosen to minimize the number of sharp angles in the triangulation. This triangulation is shown in Fig. 8.9a.

On this triangulated surface, we apply our method. First, the dual graph of this surface is determined and we apply the placement algorithm on that graph to determine a suitable placement of the pantograph mechanisms. When the mechanisms are placed on the surface according to this placement, we obtain the shape shown in Fig. 8.9b and Supplementary Movie 2.

For the cardioid we have constructed here, the rotation angle θ can lie in



(a) (b)

Figuur 8.9: The surface of the cardioid is first triangulated (a), after which each triangular face is replaced by a skew pantograph (b) to obtain a dilational surface. A movie of the final mechanism is included in the supplementary material.

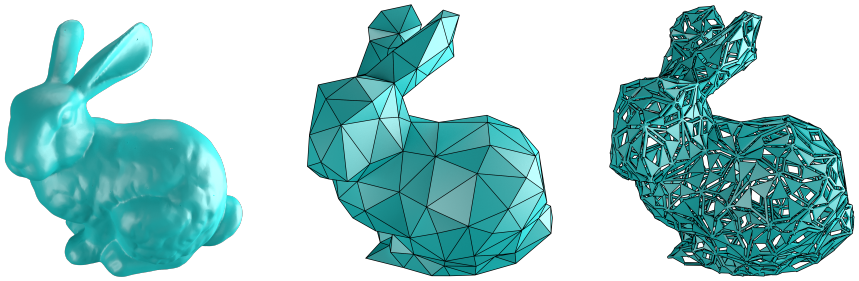
the range $[-20.5°, 20.3°]$, resulting in a maximum scaling factor of $\lambda = 0.937$. A movie of the resulting dilational surface moving between its extremal points is included in the supplementary materials.

As a final example, we have taken the Stanford Bunny [33], shown in Fig. 8.10a. For the bunny, we took an available triangulation [34], and edited the triangulation manually to remove the triangles with the sharpest angles in order to increase the maximum scaling factor. The resulting model is shown in Fig. 8.10b. This mesh was then fed into our algorithm, which computed a suitable placement of the pantograph mechanisms. The resulting dilational mechanism is shown in Fig. 8.10c and Supplementary Movie 3.

For this mechanism, the rotation angle θ can lie in the range $[-15.0°, 13.1°]$, resulting in a maximum scaling factor $\lambda = 0.966$. This scaling factor is not limited by the shape of the Stanford Bunny, but rather by the specific triangulation used to approximate it and the placement of the pantographs on the triangulation. The maximum scaling factor could be increased further by triangulating the Stanford bunny such that the triangles are close to equilateral, thereby removing even more sharp angles from the polyhedron. Even so, the linear scaling of 3.4% obtained here is already similar to the diametric expansion of human arteries during the cardiac cycle [35]

8.3. Discussion

In this work we introduce a comprehensive strategy to achieve dilation of any surface. We do this by triangulating the surface and replacing the triangular faces with Sylvester's pantographs. The similarity points of this pantograph always span a similar triangle. We constrain these triangles in such a way that their orientation is preserved, this preserves the shape of the triangulated surface



(a) (b) (c)

Figuur 8.10: (a) shows the original Stanford bunny [33]. (b) shows our adaptation of the triangulated version by Thingiverse user johnny6 [34], which was used to create the dilational surface shown in (c) by replacing each triangular face with skew pantograph mechanisms. The resulting surface has a scaling factor of $\lambda = 0.966$. A movie of the final mechanism is included in the supplementary material.

while allowing it to scale.

Kinematically, a structure constructed using this strategy can be scaled to a single point from its original size. In practice, however, the range of motion of the pantographs is limited by both collisions between links within a pantograph, and collisions between neighboring pantograph mechanisms.

Collisions within the pantograph linkage cause the pantograph with the smallest range of motion to limit the motion of the whole structure, since all pantographs share a single degree of freedom. This could be improved by changing the triangulation strategy and optimizing the placement of the pantographs such that the top-angle of the triangles comes out more favorable (possibly favoring one motion direction over the other). Better pantograph placements might be found, since our pantograph placement algorithm yields non-unique solutions to the pantograph placement problem.

We avoid collisons between neighboring pantograph mechanisms by tiling them in a specific manner. We used a graph-based approach to generate suitable placemements of mechanisms and showed that this approach works for any triangulated surface.

We have illustrated our method with three examples: an octahedron, a cardioid and the Stanford bunny. These surfaces increase in complexity and have varying Gaussian curvature. For the octahedron, the maximal scaling and suitable tiling can be determined by hand. For the cardioid and the Stanford bunny, there are many more triangular faces and the faces are more irregular, for which we present computational methods to generate dilational structures for these surfaces.

The planar kinematics of the pantographs ensure that the resulting dilational mechanism stays close to the described surface throughout the range of motion. This leaves the encompassed interior entirely empty.

A interesting side-effect is that our implementation of the method is directly

compatible with the often used STL file format for 3D objects. As such, our strategy could be implemented as a one-click solution to create dilational models.

Bibliografie

[1] F. G. Broeren, V. van der Wijk, and J. L. Herder, *Spatial pseudo-rigid body model for the analysis of a tubular mechanical metamaterial,* Math. Mech. Solids , 108128651987550 (2019).

[2] J. H. Brackenbury, *Wing Folding in Beetles,* in *IUTAM-IASS Symp. Deployable Struct. Theory Appl.* (Springer, Dordrecht, 2000) pp. 37–44.

[3] S. De Focatiis, D.S.A., Guest, *Deployable membranes designed from folding tree leaves,* Philos. Trans. R. Soc. London A Math. Phys. Eng. Sci. **360** (2002), 10.1098/rsta.2001.0928.

[4] J. M. Fernandez, M. Schenk, G. Prassinos, V. J. Lappas, and S. O. Erb, *Deployment Mechanisms of a Gossamer Satellite Deorbiter,* in *15th Eur. Sp. Mech. Tribol. Symp.* (Noordwijk, The Netherlands, 2013).

[5] M. Schenk, S. G. Kerr, A. M. Smyth, and S. D. Guest, *Inflatable Cylinders for Deployable Space Structures,* in *Proc. First Conf. Transform.*, edited by F. Escrig and J. Sanchez (Seville, 2013).

[6] H. Petroski, *Engineering: Deployable Structures,* Am. Sci. **92**, 122 (2004).

[7] Z. You and S. Pellegrino, *Foldable bar structures,* Int. J. Solids Struct. **34**, 1825 (1997).

[8] K. Kuribayashi, K. Tsuchiya, Z. You, D. Tomus, M. Umemoto, T. Ito, and M. Sasaki, *Self-deployable origami stent grafts as a biomedical application of Ni-rich TiNi shape memory alloy foil,* Mater. Sci. Eng. A **419**, 131 (2006).

[9] M. N. Ali, J. J. C. Busfield, and I. U. Rehman, *Auxetic oesophageal stents: structure and mechanical properties,* J. Mater. Sci. Mater. Med. **25**, 527 (2014).

[10] C. Hoberman, *Reversibly Expandable Doubly-curved Truss Structure,* (1990).

[11] C. Hoberman, *Retractable structures comprised of interlinked panels,* (2002).

[12] G. W. Milton, *Composite materials with poisson's ratios close to — 1,* J. Mech. Phys. Solids **40**, 1105 (1992).

[13] G. W. Milton, *New examples of three-dimensional dilational materials,* Phys. status solidi **252**, 1426 (2015).

[14] G. Kiper and E. Söylemez, *Polyhedral linkages obtained as assemblies of planar link groups,* Front. Mech. Eng. **8**, 3 (2013).

[15] C. M. Gosselin and D. Gagnon-Lachance, *Expandable Polyhedral Mechanisms Based on Polygonal One-Degree-of-Freedom Faces,* Proc. Inst. Mech. Eng. Part C J. Mech. Eng. Sci. **220**, 1011 (2006).

[16] K. Bertoldi, *Harnessing Instabilities to Design Tunable Architected Cellular Materials,* Annu. Rev. Mater. Res. **47**, 51 (2017).

[17] A. A. Zadpoor, *Mechanical meta-materials,* Mater. Horizons **3**, 371 (2016).

[18] K. E. Evans, *Auxetic polymers: a new range of materials,* Endeavour **15**, 170 (1991).

[19] K. E. Evans and A. Alderson, *Auxetic Materials: Functional Materials and Structures from Lateral Thinking!* Adv. Mater. **12**, 617 (2000).

[20] G. N. Greaves, A. L. Greer, R. S. Lakes, and T. Rouxel, *Poisson's ratio and modern materials,* Nat. Mater. **10**, 823 (2011).

[21] Shim, C. Perdigou, E. R. Chen, K. Bertoldi, and P. M. Reis, *Buckling-induced encapsulation of structured elastic shells under pressure,* Proc. Natl. Acad. Sci. United States Am. **109** (2012).

[22] B. Meserve, *Fundamental concepts of geometry* (Addison-Wesley, Cambridge (Mass.), 1955).

[23] N. J. Lennes, *Theorems on the Simple Finite Polygon and Polyhedron,* Am. J. Math. **33**, 37 (1911).

[24] T. Grimm, *The Rapid Prototyping Process,* in *User's Guid. to Rapid Prototyp.* (Society of Manufacturing Engineers (SME), 2004) Chap. 3, pp. 49–84.

[25] E. E. Moise, *Geometric Topology in Dimensions 2 and 3*, Graduate Texts in Mathematics, Vol. 47 (Springer New York, New York, NY, 1977).

[26] J. J. Sylvester, *On the Plagiograph aliter the Skew Pantigraph,* Nature **12**, 168 (1875).

[27] J. J. Sylvester, *History of the Plagiograph,* Nature **12** (1875).

[28] E. Dijksman, *Motion geometry of mechanisms.* (Cambridge University Press, Cambridge, UK, 1976).

[29] A. S. Hall, *Kinematics and linkage design* (Waveland Press, 1986) p. 162.

[30] F. G. Broeren, W. W. Van De Sandel, V. Van Der Wijk, and J. L. Herder, *Dilational Triangulated Shells Using Pantographs,* in *2018 Int. Conf. Reconfigurable Mech. Robot. ReMAR 2018 - Proc.* (Institute of Electrical and Electronics Engineers Inc., 2018).

[31] B. Delaunay, *Sur la Sphère Vide,* Bull. Acad. Sci. USSR **12**, 793 (1934).

[32] D. T. Lee and B. J. Schachter, *Two algorithms for constructing a Delaunay triangulation,* Int. J. Comput. Inf. Sci. **9**, 219 (1980).

[33] Stanford University Computer Graphics Laboritory, *Stanford Bunny,* (1994).

[34] Johnny6, *Low Poly Stanford Bunny,* Thingiverse **151081** (2013).

[35] N. J. Weissman, I. F. Palacios, and A. E. Weyman, *Dynamic expansion of the coronary arteries: Implications for intravascular ultrasound measurements,* Am. Heart J. **130**, 46 (1995).

9

Discussion

In this dissertation, we have explored how elastic mechanical metamaterials can be represented by rigid body mechanisms and how, when treating the reverse problem, rigid body mechanisms can be a design tool for elastic mechanical metamaterials. In this chapter, we will place these results into a broader context. What have we learned from this work and how could it be applied in the future? Also, and equally importantly, when do the methods described in this dissertation not work and what are their limitations?

This dissertation started with a set of definitions and explanations of the terms regularly used in metamaterial and mechanism research. In that chapter, we introduced a definition of a metamaterial that is close to how we use regular materials. The metamaterial is not the finished product, rather it is the building material from which other components can be made. In this light, the applications mentioned in Chapter 3, for a tubular auxetic structure, are applications of a metamaterial. It is investigated how a planar 'Holey Sheet' type metamaterial can be used to make a tubular stent while preserving the effective material properties of the original metamaterial.

Chapter 3 also serves to illustrate the usefulness of a rigid body approach to mechanical metamaterial analysis and design. It shows how the complex spatial motion of the elastic metamaterial can be accurately captured by a rigid body mechanism. We see that, by augmenting the mechanisms with springs to create a Pseudo-Rigid Body Model, the stiffness of the structure, as well as the effects of the boundary conditions, can be taken into account. The resulting model is analytic, and therefore substantially simpler and quicker to evaluate than commonly used finite element models.

In Chapters 4 and 5, the synthesis problem was addressed. We investigated how Poisson's ratio can be designed in a planar periodic mechanism and how such a mechanism can then be transformed into an elastic metamaterial. In Chapter 4, we show that Poisson's ratio is effectively a transmission ratio between two orthogonal periodicity generators and that literature on linkages

serves as a great starting point for finding mechanisms with the desired transfer function. In that chapter, we show examples for Poisson's ratios of -1, $\frac{1}{2}$, 0 and 1, but any fractional Poisson's ratio can be achieved using this method, provided that we can find a linkage that draws the corresponding polynomial curve. A well-known result by Kempe[1], tells us that for any polynomial function such linkages exist, although the construction in that paper almost invariably yields linkages that are too complex for application in metamaterials. Later adaptations of his method[2, 3] do yield simpler mechanisms but often involve higher kinematic pairs such as cams and cable transmissions which are not readily suitable to convert into a compliant structure. The open challenge here lies therefore in the design of linkages that follow or approximate the desired curve while being simple enough to allow for the construction of a compliant version.

Chapter 5 shows that, even when we have found a suitably simple linkage, there can be multiple ways to design a periodic adaptation from it. We see that the choices made here affect the performance of the resulting mechanical metamaterial. Depending on the requirements of the part which is to be made from the metamaterial, a single-layer design with less accurate long-range performance could be preferable over a more complex design with multiple layers that more accurately captures the designed Poisson's ratio for large deformations.

In Chapter 6, we have investigated how to construct mechanical metamaterials at the microscale and we have introduced the concept of an auxetic interval. Auxeticity, which is taken here as a non-expansion of the material in any direction when it is compressed, is a widely studied property of mechanical metamaterials. Previous work by C. Borcea and I. Streinu[4–6] has yielded a design methodology that generates frameworks that are guaranteed to be auxetic, albeit mostly for deformations from the fabrication position. By constructing one of these frameworks in a monolithic form, we have experimentally demonstrated the existence of the auxetic interval in these frameworks. Additionally, the results in this chapter serve to illustrate the importance of considering deformations of the material along all orthogonal directions. When the studied structure would only be viewed along a single direction (along the axis of four-fold rotational symmetry), one could be made to believe that it is auxetic up to very large deformations. The other directions, however, show a much more limited auxetic interval, after which the structure expands in certain directions under increasing compression. This ties into the definition of auxeticity given at the start of this work and shows that a single Poisson's ratio is insufficient for determining auxeticity in spatial structures.

Finally, in Chapters 7 and 8, we have investigated metamaterial design for non-flat surfaces. Periodicity, such as it has been introduced in the Chapter 2, inherently only applies to surfaces that can be divided into equal parts by sets of straight lines or planes. When looking at surfaces, this limits us to the plane. Therefore, we have explored alternative ways to define a unit cell. We keep the concept of a tiling, where only a small part of the structure needs to be designed and can then be copied all over the desired surface, but we change

the way in which these cells are copied. In Chapter 7, this is done according to spherical symmetry groups, resulting in unit cells that are exactly equal but are copied over a sphere using mirroring and rotation operators. In Chapter 8, we consider more general curved surfaces and allow the unit cell to change its shape while keeping its mechanical properties.

These two chapters have shown that, by using a generalized definition of the unit cell, curved surfaces can be created with custom properties. The work in this dissertation has only considered scaling of the resulting surface, but the same technique can also be used to add different mechanical properties to these surfaces, such as multiple stable states or completely different transformations.

Looking at this dissertation as a whole, we see that, for bending-dominated mechanical metamaterials, a Pseudo-Rigid Body approach is a viable technique both for the analysis and design of these novel structures. We also see, however, that the conversion of a kinematic design to a compliant mechanical metamaterial is not always straightforward and that care must be taken to ensure that the designed properties are expressed in the final structures. This was clearly observed in the experiments in Chapter 5.

In this dissertation, only bending-dominated mechanical metamaterials have been considered. This was a conscious choice since the kinematic techniques we present are most suitable for this class of metamaterial. Stretching-dominated structures could also be studied using a Pseudo-Rigid Body approach. In this case, we would allow stretching of the members and model them as prismatic joints with an appropriate stiffness. However, because these structures are usually designed to be as stiff as possible while minimizing weight [7–9], no substantial kinematic behavior is expected. For these structures, PRB methods could be used to estimate and/or design the resulting stiffness of the metamaterial.

We have seen that PRB models are useful in the approximation of the effective material properties of mechanical metamaterials, but that they are rarely exact. This is inherent to the simplification of the problem when converting an elastic structure to a linkage. Therefore, when designing mechanical metamaterials to exact specifications further refinement and optimization steps are necessary. Most structural optimization steps are very sensitive to their initial conditions, and a good initial guess can greatly improve both the convergence and the optimality of the final result. This is where an initial PRB design could be valuable, allowing for a quick and intuitive method for establishing a structure that performs close to specification.

The promise of metamaterials is that we can design materials to specification. By cleverly designing the material architecture, it is possible to create material with completely new and not naturally occurring sets of material properties. This design process is, as of yet, complicated because of the multitude of factors involved. We envision PRB methods as a first step in the design of tailor-made mechanical metamaterials. Given a set of material properties, a linkage, augmented with springs at its joints, can be created to match this behavior.

From this linkage, an initial compliant design can be constructed by replacing the joints with slender elements. When these rational design steps are executed carefully, they will yield a mechanical metamaterial with properties close to the desired values. When greater accuracy is required, further refinements can be applied, either by redesigning the kinematic structure or by optimizing the shape of the resulting compliant structure.

Mechanical metamaterials also allow for a greater degree of function integration in machines. Instead of adding sensors and actuators onto a manufactured object, these could be integrated into the material from which the objects are made. This would allow for a distribution of functionality and increased adaptability of the created objects. Clamps and brackets in machine parts could be created to sense and dampen vibrations autonomously or facades of buildings could be made of materials that open or close to regulate the inside climate. Each level of functionality that is added to these mechanical metamaterials also comes with increased complexity. This further increases the need for accurate and intuitive design tools such that ideas and concepts can be quickly evaluated and iterated. The methods shown in this dissertation, and possible extensions thereof, will be exceptionally suited for this stage of the design process, allowing for fast development of the conceptual design.

Bibliografie

[1] A. B. Kempe, *On a General Method of describing Plane Curves of the n^{th} degree by Linkwork,* Proc. London Math. Soc. **s1-7**, 213 (1875).

[2] Y. Liu and J. M. McCarthy, *Synthesis of a linkage to draw a plane algebraic curve,* Mechanism and Machine Theory **111**, 10 (2017).

[3] M. Gallet, C. Koutschan, Z. Li, G. Regensburger, J. Schicho, and N. Villamizar, *Planar linkages following a prescribed motion,* Mathematics of Computation **86**, 473 (2017).

[4] C. Borcea, I. Streinu, and S.-i. Tanigawa, *Periodic Body-and-Bar Frameworks,* SIAM J. Discret. Math. **29**, 93 (2015).

[5] C. S. Borcea and I. Streinu, *New principles for auxetic periodic design,* SIAM journal on applied algebra and geometry **1**, 442 (2017).

[6] C. S. Borcea and I. Streinu, *Auxetic regions in large deformations of periodic frameworks,* in *Interdisciplinary Applications of Kinematics*, edited by A. Kecskeméthy, F. Geu Flores, E. Carrera, and D. A. Elias (Springer International Publishing, Cham, 2019) pp. 197–204.

[7] V. Deshpande, M. Ashby, and N. Fleck, *Foam topology: bending versus stretching dominated architectures,* Acta Mater. **49**, 1035 (2001).

[8] T. A. Schaedler, A. J. Jacobsen, A. Torrents, A. E. Sorensen, J. Lian, J. R. Greer, L. Valdevit, W. B. Carter, Q. Ge, J. A. Jackson, S. O. Kucheyev, N. X. Fang, and C. M. Spadaccini, *Ultralight metallic microlattices.* Science **334**, 962 (2011).

[9] J. B. Berger, H. N. G. Wadley, and R. M. McMeeking, *Mechanical metamaterials at the theoretical limit of isotropic elastic stiffness,* Nature (2017), 10.1038/nature21075.

10

Conclusion

In this dissertation, we have demonstrated how kinematic methods can be used to design mechanical metamaterials. By approaching metamaterial design from a mechanism perspective, Poisson's ratio becomes a transmission, and Young's modulus becomes a function of the joint stiffnesses. This translation between the field of materials science and mechanism science allows us to take inspiration from the vast body of literature on linkages and kinematics.

Furthermore, the toolbox of kinematic design allows us to rationalize and simplify the design process, allowing us to tackle the problem piece by piece. First, Poisson's ratio can be designed as a transmission between two orthogonal directions, after which Young's modulus can be designed by adding springs to the mechanism, and finally these stiffnesses can be used to dimension the final compliant structure. This piecewise method transforms a complicated problem, where the whole continuum mechanics of the structure needs to be evaluated into a more familiar design problem. In this way, a designer can rationally design new mechanical metamaterials, instead of having to rely on a computer to generate and optimize the solutions from the start.

The contributions of this thesis lie in furthering the understanding of the principles behind bending-dominated mechanical metamaterials and applying Pseudo-Rigid Body Models to this class of materials. It introduces the concept of Poisson's ratio as a transmission and illustrates how this can guide the design process. Furthermore, it expands the realm of metamaterials to curved surfaces. It is shown how periodic tilings of mechanical systems can be extended to non-flat surfaces and how this can be used to create shell-based auxetic mechanisms. Throughout the work, theoretical findings are supported by experimental results. This indicates that the contributions of this thesis do not only serve to further the academic study of metamaterials but that they can also be applied in practice.

Curriculum Vitæ

Freek Gerardus Johannes Broeren

12-06-1991 Born in 's-Hertogenbosch, the Netherlands.

Education

2002-2009 High School
Gymnasium Bernrode, Heeswijk-Dinther, the Netherlands

2009-2013 BSc. Physics
Leiden University, Leiden, the Netherlands

Research Project: An EPR Investigation of the Conformations of Pseudoazurin
Advisor: Dr. P. Gast

2013-2015 MSc. Experimental Physics
Leiden University, Leiden, the Netherlands

Research Project 1: Detecting Tau Neutrinos with KM3NeT (Internship at NIKHEF, Amsterdam)
Advisor: Dr. D. Samtleben

Research Project 2: Understanding Mechanical Metamaterials Through 3D Printing (Internship at AMOLF, Amsterdam)
Advisor: Dr. C. Coulais

2016-2020 PhD. Mechanical Engineering
Delft University of Technology, Delft, the Netherlands

Topic: Kinematic Methods for Mechanical Metamaterial Design
Promotor: Prof. dr. ir. J.L. Herder
Copromotor: Dr. V. van der Wijk

Work Experience

2020 - Juniordocent
Delft University of Technology, Delft, the Netherlands

List of Publications

Peer-Reviewed Journal Publications

6. C.S. Borcea, **F.G.J. Broeren**, I. Streinu, J.L. Herder and V. van der Wijk *Auxetic interval determination and experimental validation for a three dimensional periodic framework*, Mathematics and Mechanics of Solids **27**, 5 (2022)

5. B. Boogaard, A. Tas, J. Nijssen, **F.G.J. Broeren**, J. van den Dobbelsteen, V. Verhoeven, J. Pluim, S. Dekker, E.J. Snijder, M.J. van Hemert and S. Herfst *Efficacy Assessment of Newly-designed Filtering Facemasks during the SARS-CoV-2 Pandemic*, Aerosol and Air Quality Research **21**, 3 (2021).

4. T.W.A. Blad, J. Nijssen, **F.G.J. Broeren**, B. Boogaard, S. van der Toorn, S. Lampaert, J. van den Dobbelsteen *A Rapidly Deployable Test Suite for Respiratory Protective Devices in the COVID-19 Pandemic*, Applied Biosafety **23**, 3 (2020).

3. **F.G.J. Broeren**, W.W.P.J. van de Sande, V. van der Wijk and J.L. Herder, *A General Method for the Creation of Dilational Surfaces*, Nature Communications **10**, 5180 (2019).

2. **F.G.J. Broeren**, J.L. Herder and V. van der Wijk, *Spatial pseudo-rigid body model for the analysis of a tubular mechanical metamaterial*, Mathematics and Mechanics of Solids **25**, (2019).

1. P. Gast, **F.G.J. Broeren**, S. Sottini, R. Aoki, A. Takashina, T. Yamaguchi, T. Kohzuma and E.J.J. Groenen *The type 1 copper site of pseudoazurin: Axial and rhombic*, Journal of Inorganic Biochemistry **Volume 137**, p57-63 (2014).

Conference Publications

3. I.R. Nuijts, **F.G.J. Broeren**, V. van der Wijk and J.L. Herder, *An Origami-Inspired Spherical Transformable Metamaterial Based on Symmetry Groups*, 2019 7th International Conference on Control, Mechatronics and Automation (ICCMA), Delft, Netherlands p295-298 (2019).

2. **F.G.J. Broeren**, V. van der Wijk and J.L. Herder, *On the Synthesis of Periodic Linkages with a Specific Constant Poisson's Ratio*, Advances in Mechanism and Machine Science. IFToMM WC 2019. Mechanisms and Machine Science, **vol 73** (2019).

1. **F.G.J. Broeren**, W.W.P.J. van de Sande, V. van der Wijk and J.L. Herder *Dilational Triangulated Shells Using Pantographs*, 2018 International Conference on Reconfigurable Mechanisms and Robots (ReMAR) (2018).

In Preparation

1. **F.G.J. Broeren**, V. van der Wijk and J.L. Herder *Mechanical Metamaterial with Poisson's Ratio Close to 1 Based on the Inversor Linkage*, submitted to Mechanism and Machine Theory (2022)

Other Publications

1. **F.G.J. Broeren**, V. van der Wijk and J.L. Herder *Tailored Properties*, Mikroniek (2020)

Acknowledgements

After more than six years of work leading up to this dissertation, I have amassed a great number of people to whom I owe thanks. It therefore feels inevitable that some will be missed. Nevertheless, I will try to say thanks to all those who have helped me get here.

First of all, let me thank Just and Volkert without whose supervision and trust none of this would have happened. You made a great team together, possibly without even knowing it yourselves. The incredibly positive support from Just, combined with the incredibly critical attitude from Volkert has helped me grow both in my research and my writing.

Secondly, my colleagues from the department of Precision and Microsystems Engineering, and especially my direct colleagues from the MSD lab. Thank you for the insightful discussions about our work and especially for those about all other topics. I would not have been able to work this hard for this long without the great atmosphere around the office. I fondly remember the trips we took together, the endless discussions about whether the earth might be flat or whether we might be in a simulation, and of course all the times we were able to help each other out whenever we got stuck in our work.

To all my fellow juniordocenten whom I have worked with in the past couple of years: thank you for getting me incredibly enthusiastic about a profession I would have never previously dreamed of.

Many thanks to all my friends outside of the TU Delft for keeping me grounded and pulling me out of research every now and then. Whether it was in the FooBar, het Keizertje or during Paaspop, you almost always managed to get my mind off of work eventually, which was at times an incredibly welcome relief.

I would like my parents for having my back, helping me make my own decisions, and supporting me throughout.

Finally, I would be amiss not to thank my partner Eline for her incredible support. You were always happy to let me ramble on about my work right up to the point where I could figure out the solution to my problem. I am still not sure whether you actually listened to it all, but if you did you must be able to defend this dissertation as well as I am. Thank you for putting up with me during these years and I look forward to returning the favor in the years to come.

Freek Gerardus Johannes Broeren
Voorschoten, November 2022